UNIVERSITY OF CALIFORNIA

SANTA CRUZ

ADVANCED ELECTRODE DESIGN FOR HIGH-RATE ALKALINE WATER SPLITTING

A dissertation submitted in partial satisfaction

of the requirements for the degree of

DOCTOR OF PHILOSOPHY

In

CHEMISTRY

by

Qiu Ren

August 2026

The Dissertation of Qiu Ren is approved:

_____

Professor Yat Li, chair

_____

Professor Jin Zhong Zhang

_____

Professor Scott R. J. Oliver

_____

Donald Smith

Interim Vice Provost and Dean of Graduate Studies

Table of Contents

List of Figures vii

List of Tables xvi

Abstract xvii

Dedication xix

Acknowledgement xx

Chapter 1 1

Introduction of Electrochemical Water Splitting 1

Abstract 1

1.1 Background 2

1.2 Water splitting technologies 3

1.3 Fundamentals of water splitting 4

1.3.1 Hydrogen evolution reaction 5

1.3.2 Oxygen evolution reaction 6

1.4 High-rate water splitting 7

References 11

Chapter 2 13

Nanocone-Modified Surfaces for Enhanced Bubble Detachment in High-Rate Alkaline Water Splitting 13

2.1 Abstract 13

2.2 Introduction 13

2.3 Experimental section 15

2.3.1 Preparation of nickel nanocone-modified electrodes 15

2.3.2 Fabrication of 3D-printed nickel lattice electrodes 15

2.3.3 Structural and surface characterization 16
2.3.4 Simulation of bubble detachment dynamics 16
2.3.5 High-speed imaging of bubble evolution 17
2.3.6 Electrochemical measurements 17
2.4 Results and discussion 19
2.4.1 Surface morphology and structural characterization 19
2.4.2 Bubble detachment dynamics: simulation insights 23
2.4.3 Experimental observation of bubble evolution 26
2.4.4 Electrochemical performance at high current densities 31
2.4.5 Extension to 3D architectures 36
2.4.6 Long-term stability and surface integrity 41
2.5 Conclusion 44
References 45
Chapter 3 48
Interpenetrating 3D Electrodes for High-Rate Alkaline Water Splitting 48
3.1 Abstract 48
3.2 Introduction 49
3.3 Experimental section 51
3.3.1 Fabrication of 3D-printed interpenetrating gyroid electrodes 51
3.3.2 Metallization of 3DIG and 3DG 52
3.3.3 Synthesis of NiFeOOH@3DIG 53
3.3.4 Electrode fabrication 53
3.3.5 Structural and surface characterization 54
3.3.6 Electrochemical measurements 54

3.4 Results and discussion 56
3.4.1 Surface morphology and structural characterization 56
3.4.2 Ionic transport characteristics from simulation..... 59
3.4.3 Electrochemical performance 61
3.4.4 Electrochemical impedance analysis 66
3.4.5 Long-Term Stability..... 72
3.4.6 Catalyst modification of 3DIG electrodes 72
3.5 Conclusion 74
References..... 75
Chapter 4..... 78
Ni^{3+}-Enriched Nickel Sulfide Catalysts for Urea Oxidation..... 78
4.1 Abstract 78
4.2 Introduction..... 79
4.3 Experimental section..... 82
4.3.1 Structural characterization 82
4.3.2. 3D printing of interpenetrated polymer substrates and flow cell device 82
4.3.3 Ni deposition of 3D-printed interpenetrating electrodes 83
4.3.4. Synthesis of nickel sulfide on Ni substrates 84
4.3.5. Preparation of Ni_3S_2-modified 3DIE for electrochemical tests ... 84
4.3.6. Electrochemical measurements..... 85
4.3.7. *In-situ* Raman spectroscopy..... 85
4.3.8. Simulation..... 86
4.4 Results and discussion 87

4.4.1. Surface morphology and structural characterization 87

4.4.2 Electronic Structure and Valence-State Analysis 90

4.4.3 Electrochemical performance 95

4.4.4 Mechanistic study 105

4.5 Device-level performance of the interpenetrating electrode architecture 111

4.6 Conclusion 114

References 116

Chapter 5 120

Conclusion and outlook 120

References 123

List of Figures

Chapter 1

Figure 1.1. Key challenges in high-rate water splitting: (a) gas bubble accumulation, (b) ion-diffusion limitation, and (c) sluggish OER kinetics.

Chapter 2

Figure 2.1. SEM images of (a) Foil and (e) Foil_NC; (b) Foam and (f) Foam_NC; and 3D-printed Ni lattice (c, d) before and (g, h) after nanocone modification. Scale bars are 1 μm for (a, b, e, f), 300 μm for (c, g), and 1 μm for the magnified images in (d, h).

Figure 2.2. XRD patterns of (a) carbon paper and nanocone-modified carbon paper (Carbon paper_NC), and (b) Foil_NC, Foam_NC, and Lattice_NC. The standard Ni diffraction pattern (PDF# 04-0850) is included for reference.

Figure 2.3. Ni 2p XPS spectra of (a) Lattice and (b) Lattice_NC.

Figure 2.4. Digital images showing the air contact angles on (a) Foil and (b) Foil_NC.

Figure 2.5. Simulation of a single bubble on (a) flat and cone-decorated surfaces with initial depth of (b) $h/h_0 = 1$, (c) $h/h_0 = 2/3$ and (d) $h/h_0 = 1/3$. Normalized simulation time (t*) is labeled for all four cases below (d). (e) Schematic illustration of the initial depth $\frac{h}{h_0}$. (f) Normalized attachment time of the bubble for flat and cone substrates shown a-d.

Figure 2.6. High-speed camera images showing hydrogen bubble evolution on (a-c) Foil and (d-f) Foil_NC as a function of time. Scale bars are 500 μm. The dashed circles highlight the bubble locations. Histograms illustrate the distribution of (g, h)

bubble detachment time (T_d) and (i, j) detachment size (D_d) on Foil and Foil_NC substrates.

Figure 2.7. High-speed camera images show the oxygen bubble evolution process take place on (a-c) Foil and (d-f) Foil_NC, as a function of time. Scale bars are 500 μm. The dashed circles highlight the bubble locations. Histograms illustrate the distribution of (g, h) bubble detachment time (T_d) and (i, j) detachment size (D_d) on Foil and Foil_NC substrates.

Figure 2.8. Gas bubble evolution at the high current density of 1000 mA cm^{-2}. Hydrogen bubble evolution on (a) Foil and (b) Foil_NC. Oxygen bubble evolution on (c) Foil and (d) Foil_NC. Scale bars are 2 mm.

Figure 2.9. LSVs for (a) HER and (b) OER plotted based on geometric current density at a scan rate of 0.1 mV s^{-1}. Comparison of overpotentials required to reach 1000 mA cm^{-2} for (c) HER and (d) OER.

Figure 2.10. ECSA analysis and ECSA-normalized electrochemical performance of pristine Ni foil and Foil_NC. Capacitive current density plotted as a function of scan rate in the non-faradaic regions for (a) HER and (d) OER, respectively. (b and e) Comparison of ECSA values calculated from the scan-rate-dependent current response. ECSA-normalized polarization curves for (c) HER and (f) OER in 1.0 M KOH.

Figure 2.11. CV curves of Foam and Foam_NC collected for (a, b) HER and (d, e) OER in 1.0 M KOH at different scan rates from 20 to 100 mV s^{-1} with an interval of 20 mV s^{-1}. The difference of geometric current density j_{geo} of Foam and Foam_NC are plotted as a function of scan rate for (c) HER and (f) OER, respectively.

Figure 2.12. LSVs of Foam and Foam_NC electrodes collected in 1.0 M KOH at a scan rate of 0.1 mV s^{-1} for (a, b) HER and (c, d) OER. Figures (a and c) are plotted in geometric current density, while Figures (b and d) are plotted in ECSA-normalized current density.

Figure 2.13. CV curves of the Lattice and Lattice_NC for (a-b) HER and (d-e) for OER were collected in 1.0 M KOH at different scan rates from 20 to 100 mV s^{-1} at an interval of 20 mV s^{-1}. The difference of geometric current density j_{geo} of Lattice and Lattice_NC are plotted as a function of scan rate for (c) HER and (f) OER, respectively.

Figure 2.14. LSVs of Lattice and Lattice_NC electrodes collected in 1.0 M KOH at a scan rate of 0.1 mV s^{-1} for (a, b) HER and (c, d) OER. Figures (a and c) are plotted in geometric current density, while Figures (b and d) are plotted in ECSA-normalized current density. Figures (e and f) compare the HER and OER overpotentials of Foil_NC, Foam_NC, and Lattice_NC at different geometric current densities.

Figure 2.15. EIS spectra of (a, d) Foil and Foil_NC, (b, e) Foam and Foam_NC, and (c, f) Lattice and Lattice_NC were collected in 1.0 M KOH. The top row shows EIS spectra under HER conditions, and the bottom row shows EIS spectra under OER conditions. EIS was performed at -1.08 V versus Hg/HgO for HER and 0.70 V versus Hg/HgO for OER, with a frequency ranging from 100 kHz to 1 Hz and an amplitude of 5 mV. Circles represent experimental data. The solid lines represent fitting curves based on the equivalent circuit model (inset).

Figure 2.16. The geometric current density of a device assembled with two Lattice_NC electrodes recorded at a fixed voltage of 2.45 V for 100 h. The inset

figure shows a schematic illustration of the two-electrode device. The SEM images show the NC morphology before and after the stability test.

Figure 2.17. Ni 2p XPS spectra of (a) Lattice_NC after HER and (b) Lattice_NC after OER stability tests in water splitting.

Chapter 3

Figure 3.1. (a) Schematic illustration of an interpenetrating gyroid structure. Gyroid 1 and Gyroid 2 are highlighted with red and blue curves, respectively. (b) Schematic diagram showing the fabrication process of 3DIG. (c) Digital image of 3DIG. (d) Magnified image of the boxed region in (c). (e) SEM image of 3DIG showing the strut thickness and pore size. (f) SEM image of the surface of a 3DIG strut after metallization. (g) EDS elemental mapping of a single 3DIG strut showing the uniform distribution of Ni.

Figure 3.2. (a, b) Digital image of 3DG, where Gyroid 1 and Gyroid 2 electrodes are arranged in a separate configuration. (c-e) SEM images of a gyroid lattice under different magnifications.

Figure 3.3. XRD patterns of 3DIG and 3DG. Standard Ni diffraction (PDF# 04-0850) is added for reference.

Figure 3.4. Simulation comparing ion diffusion kinetics in 3DIG and 3DG, driven by constant concentration and electric potential gradients. (a) Average normalized ion concentration in the electrolyte as a function of normalized time. Normalized equilibrium concentration distribution in (b) 3DIG and (c) 3DG. Normalized electric potential gradient magnitude in (d) 3DIG and (e) 3DG.

Figure 3.5. (a) Schematic illustration of a repeating unit in the interpenetrating gyroid structure. Digital images show interpenetrating gyroid structures with

different unit cell lengths (b) 4 mm, (c) 6 mm, and (d) 8 mm. These electrodes' thicknesses are 3.5 mm, 5.5 mm, and 8 mm, respectively.

Figure 3.6. LSVs of 3DIG with different feature sizes collected in 1.0 M KOH at a scan rate of 1.0 mV s^{-1} (a) under geometric current density and (b) are plotted in ECSA-normalized current density.

Figure 3.7. (a) Digital images of two 3DG electrodes. (b) The distance between the two 3DG electrodes was set to be 5 mm for the water splitting test.

Figure 3.8. (a) The schematic illustration of 3DG and (b) LSVs of 3DG with separation distances collected in 1.0 M KOH at a scan rate of 1.0 mV s^{-1} are plotted in geometric current density.

Figure 3.9. CV curves of (a) 3DIG and (b) 3DG collected in 1.0 M KOH at different scan rates from 2 to 10 mV s^{-1} at an interval of 2.0 mV s^{-1}. The data obtained in the potential range from 0.1 to 0.2 V are used to determine the electrode's ECSA. (c) The geometric current density of 3DIG and 3DG are plotted as a function of scan rate.

Figure 3.10. LSVs of 3DIG and 3DG collected in 1.0 M KOH at a scan rate of 1.0 mV s^{-1} are plotted in (a) geometric current density and (b) ECSA-normalized current density.

Figure 3.11. (a) Nyquist plots of 3DIG and 3DG obtained in a frequency range from 100 kHz to 1 Hz under an amplitude of 5 mV. Circles represent experimental data. The solid lines represent fitting curves based on the equivalent circuit model (inset). Histograms show the (b) R_S and (c) R_{CT} values of 3DIG and 3DG.

Figure 3.12. (a) LSVs of 3DIG and 3DG collected in 1.0 M KOH at a scan rate of 1.0 mV s^{-1} at different temperatures. (b) The 3DG/3DIG voltage ratios obtained at 200 and 400 mA cm^{-2} are plotted as a function of temperature.

Figure 3.13. Nyquist plots of (a) 3DIG and (b) 3DG collected in a frequency range from 100 kHz to 1.0 Hz at an amplitude of 5 mV at different temperatures. Circles are experimental data. Solid lines are fitting curves based on the equivalent circuit model. Histograms show the (c) R_S, and (d) R_{CT} of 3DIG and 3DG at different temperatures.

Figure 3.14. Nyquist plot of (a) 3DIG and (b) 3DG, in a frequency range from 100 kHz to 1.0 Hz at an amplitude of 5 mV at different current densities. Circles are experimental data. Solid lines are fitting curves based on the equivalent circuit model. Insets: Magnified Nyquist plots in the high-frequency region. Histograms show the (c) solution resistance and (d) charge transfer resistance of 3DIG and 3DG obtained at different current densities.

Figure 3.15. (a) Digital image of 3DIG device. (b) The current density of 3DIG obtained at 2.4 V in 1.0 M KOH is plotted as a function of time.

Figure 3.16. (a) Digital image and (b) SEM image of NiFeOOH@3DIG. (c) Magnified SEM image showing the region highlighted by the box in (b). (d) EDS elemental mapping obtained from a strut of NiFeOOH@3DIG shows the distribution of Fe signal. (e) LSVs of 3DIG and NiFeOOH@3DIG collected in 1.0 M KOH at a scan rate of 1.0 mV s^{-1}.

Chapter 4

Figure 4.1. (a) Schematic illustration of the hydrothermal synthesis of Ni_3S_2. (b) X-ray diffraction patterns of $Ni(OH)_2$, Ni_3S_2_1.0, Ni_3S_2_2.0, Ni_3S_2_3.0 and Ni_3S_2_4.0.

Standard diffraction patterns of $Ni(OH)_2$ (PDF# 14-0117), Ni_3S_2 (PDF# 44-0805) and metallic Ni (PDF# 04-0850) are added for reference.

Figure 4.2. (a-e) SEM images of $Ni(OH)_2$, Ni_3S_2_1.0, Ni_3S_2_2.0, Ni_3S_2_3.0 and Ni_3S_2_4.0, along with corresponding elemental mappings for O, Ni, and S. Scale bars are 100 μm.

Figure 4.3. Ni 2p XPS spectra of spent catalysts: (a) $Ni(OH)_2$, (b) Ni_3S_2_1.0, (c) Ni_3S_2_2.0, (d) Ni_3S_2_3.0 and (e) Ni_3S_2_4.0. (f) Histogram showing the Ni^{3+}/Ni^{2+} ratio in the spent Ni_3S_2 samples and $Ni(OH)_2$. Quantitative analysis of the Ni^{3+}/Ni^{2+} ratios was performed using the Ni $2p_{3/2}$ peak due to its superior signal intensity and more clearly defined peak envelopes compared to the Ni $2p_{1/2}$ region.

Figure 4.4. Ni 2p XPS spectra of fresh catalysts: (a) $Ni(OH)_2$, (b) Ni_3S_2_1.0, (c) Ni_3S_2_2.0, (d) Ni_3S_2_3.0 and (e) Ni_3S_2_4.0. (f) Histogram showing the Ni^{3+}/Ni^{2+} ratio in the spent Ni_3S_2 samples and $Ni(OH)_2$. Quantitative analysis of the Ni^{3+}/Ni^{2+} ratios was performed using the Ni $2p_{3/2}$ peak due to its superior signal intensity and more clearly defined peak envelopes compared to the Ni $2p_{1/2}$ region.

Figure 4.5. S 2p XPS spectra of (a) Ni_3S_2_1.0, (b) Ni_3S_2_2.0, (c) Ni_3S_2_3.0 and (d) Ni_3S_2_4.0.

Figure 4.6. LSVs of $Ni(OH)_2$, Ni_3S_2_1.0, Ni_3S_2_2.0, Ni_3S_2_3.0 and Ni_3S_2_4.0 collected in (a) 1.0 M KOH and (b) 1.0 M KOH with 0.33 M urea, at a scan rate of 1.0 mV s^{-1}. (c) Potentials required for each sample to reach a current density of 100 mA cm^{-2}. (d) Comparison of LSVs for Ni_3S_2_3.0 collected in 1.0 M KOH (dash line) and in 1.0 M KOH with 0.33 M urea (solid line) at a scan rate of 1.0 mV s^{-1}.

Figure 4.7. CV curves of each sample (a, b) $Ni(OH)_2$, (d, e) Ni_3S_2_1.0, (g, h) Ni_3S_2_2.0, (j, k) Ni_3S_2_3.0 and (m, n) Ni_3S_2_4.0 collected in 1.0 M KOH and 1.0

M KOH with 0.33 M urea at different scan rates from 20 to 100 mV s^{-1} at an interval of 20 mV s^{-1}, respectively. The data obtained in the positive potential are used to determine the electrode's ECSA for OER and UOR, respectively. The geometric current density j_{geo} of each sample (c) $Ni(OH)_2$, (f) Ni_3S_2_1.0, (i) Ni_3S_2_2.0, (l) Ni_3S_2_3.0 and (o) Ni_3S_2_4.0 is plotted as a function of scan rate. The values in the figures are the areal capacitances of samples.

Figure 4.8. (a) The ECSA for OER and UOR of $Ni(OH)_2$, Ni_3S_2_1.0, Ni_3S_2_2.0, Ni_3S_2_3.0 and Ni_3S_2_4.0. (b) ECSA normalized LSV curves for UOR.

Figure 4.9. SEM images illustrating the surface morphology of (a) $Ni(OH)_2$, (b) Ni_3S_2_1.0, (c) Ni_3S_2_2.0, (d) Ni_3S_2_3.0, and (e) Ni_3S_2_4.0 under higher magnification. Scale bars are 4 μm.

Figure 4.10. (a) Nyquist plots of the samples obtained in a frequency region ranging from 100 kHz to 1.0 Hz under an amplitude of 5 mV at 1.417 V vs. RHE. Circles represent experimental data. The solid lines represent fitted curves based on the equivalent circuit model. (b): Enlarged view of the high frequency region. (c) Histograms illustrate the R_S and R_{CT} values across different samples.

Figure 4.11. (a) Chronoamperometric stability test conducted at 1.35 and 1.37 V vs. RHE in 1.0 M KOH with 0.33 M urea using a three-electrode configuration. (b) XRD of Ni_3S_2_3.0 before and after stability test.

Figure 4.12. *In-situ* Raman spectra of (a) Ni_3S_2_3.0 and (b) Ni_3S_2_1.0 in the electrolyte containing 1.0 M KOH with 0.33 M urea.

Figure 4.13. Lattice-resolved TEM image of the post-UOR Ni_3S_2_3.0 sample under different magnifications.

Figure 4.14. Simulated reaction pathways for (a) $Ni(OH)_2$, (b) Ni_3S_2, (c) S-rich Ni_3S_2, (d) side view of Ni_3S_2 and S-rich Ni_3S_2 and the corresponding reactions.

Figure 4.15. (a) The calculated reaction energy diagram of $Ni(OH)_2$, Ni_3S_2, and S-rich Ni_3S_2 for UOR. Inset image: the simulated profile for the rate-determining step: the formation of CO* and NH* intermediates on Ni_3S_2 catalyst. (b) The Gibbs free energy barrier for the rate-determining step of $Ni(OH)_2$, Ni_3S_2, and S-rich Ni_3S_2. The gray, yellow, red, brown, light blue and pink spheres represent Ni, S, O, C, N and H, respectively.

Figure 4.16. (a) Schematic illustration of a repeating unit in the interpenetrated structure. (b) Schematic illustration of an interpenetrated device. (c) Optical image of Ni_3S_2_3.0//Ni interpenetrated device. (d) LSVs of devices made of separated electrodes vs. interpenetrated electrodes collected in a beaker cell. (e) LSVs of the Ni_3S_2_3.0//Ni interpenetrated device collected in a home-built flow cell in 1.0 M KOH (dash line) and in 1.0 M KOH with 0.33 M urea (solid line) at a scan rate of 1.0 mV s^{-1}.

List of Tables

Chapter 1

Table 1.1. Summary of representative technical performance targets for high-rate water splitting devices.

Chapter 2

Table 2.1. Input parameters of the Shan-Chen model used in the simulation.

Chapter 3

Table 3.1. Physical dimensions of interpenetrating electrodes with different unit cell lengths.

Table 3.2. Simulation parameters for 3DIG and 3DG.

Table 3.3. The ECSA of 3DIG with different feature sizes

Chapter 4

Table 4.1. Summary of the measured weight percentages and calculated atomic percentages of Ni, O, and S for the control and sulfurized samples.

Abstract

Advanced Electrode Design for High-Rate Water Splitting

By Qiu Ren

Electrochemical water splitting provides promising technology for green hydrogen production. Among different electrolysis technologies, alkaline water splitting is attractive because it can use earth-abundant electrode materials and relatively low-cost materials. However, efficient operation at industrially relevant current densities remains challenging due to gas bubble accumulation, ion-transport resistance, sluggish anodic kinetics. These limitations become more severe under high-rate conditions, where rapid gas generation and fast ionic consumption can reduce electrode-electrolyte contact and increase the overall cell voltage.

This dissertation focuses on advanced electrode design and interfacial engineering strategies to address these challenges. First, nickel nanocone-modified surfaces were developed to improve gas bubble detachment. The nanocone structures created a superaerophobic interface, leading to shorter bubble residence times and smaller bubble detachment sizes during both the hydrogen evolution reaction and oxygen evolution reaction. Simulations and high-speed imaging confirmed that the nanocone geometry reduced bubble adhesion and promoted rapid gas release. Consequently, nanocone-modified nickel foil, foam, and 3D-printed lattice electrodes showed reduced overpotentials at high current densities, and a two-electrode device using nanocone-modified lattice electrodes operated stably for up to100 h.

Second, a 3D-printed interpenetrating gyroid electrode architecture was designed to improve ion transport. This structure consists of two independent but

spatially interwoven electrode networks, reducing the interelectrode distance while maintaining ordered channels for electrolyte transport. Simulations showed more uniform ion concentration profiles and smoother electric potential gradients than separated gyroid electrodes. Electrochemical measurements further revealed lower solution and charge-transfer resistances, confirming improved ionic transport and reaction accessibility. The architecture also maintained stable long-term operation and could be combined with catalyst modification to enhance water-splitting activity.

Finally, urea electrooxidation was investigated as an alternative anodic reaction to replace oxygen evolution for more energy-efficient hydrogen production. A valence-state engineering strategy was developed through controlled sulfurization to form nickel sulfide catalysts with enriched Ni^{3+} species, which are recognized as the active sites for the urea oxidation. The optimized nickel sulfide catalyst exhibited enhanced urea oxidation activity compared with nickel hydroxide. The results showed that sulfurization modulated the Ni^{3+}/Ni^{2+} ratio and catalytic surface environment, facilitating charge transfer and lowering the energy barrier for C-N bond cleavage. The catalyst was further integrated into a 3D-printed interpenetrating electrode device and evaluated under flow-cell conditions.

Overall, this dissertation demonstrates that surface morphology, electrode architecture, catalyst chemistry, and device configuration must be jointly optimized to improve high-rate alkaline water splitting. By addressing gas bubble accumulation, ion-diffusion limitations, and anodic energy loss, this work provides practical design principles for efficient and stable electrochemical hydrogen production under industrially relevant conditions.

Dedication

DEDICATED

TO

My parents, Changming Ren and Yuxia Yang

Acknowledgement

Time flies, and it is hard to believe that I am now approaching the end of my journey at UC Santa Cruz. First and foremost, I would like to express my deepest gratitude to my advisor, Professor Yat Li, for his guidance, support, and encouragement throughout my Ph.D. study. My first conversation with Professor Li was in 2019, when I was applying to graduate school. Because of the pandemic, I was not able to come to the United States as originally planned. During that difficult and uncertain time, Professor Li was very supportive and gave me a great deal of help while I was still in China. With his support, I was finally able to come to the United States and join his group. Throughout my Ph.D. study, Professor Li has always supported my research and helped me make progress on my projects. Whenever I faced difficulties or felt unsure about the next step, he was always willing to discuss the problems with me and provide helpful suggestions. His comments and questions often helped me see my work from a different perspective and think more deeply about my research. I learned a great deal from every discussion with him, not only about scientific knowledge, but also about how to identify important questions and carry out research more carefully. I am also very grateful for the freedom and trust he gave me to explore different research ideas. He encouraged me to work independently while always being available when I needed guidance. His feedback helped me improve my experimental design, scientific thinking, writing, and presentation skills. His support has been very important to my growth as a researcher. Beyond research, Professor Li is also a very kind and approachable person. He has always been willing to help me whenever I faced difficulties, whether they were related to research or other parts of my life.

Over the years, I have felt that he was not only my advisor, but also a mentor and a friend. I feel very fortunate to have completed my Ph.D. under his guidance, and I will always be grateful for his patience, understanding, trust, and support.

I would also like to sincerely thank my dissertation committee members, Professor Yat Li, Professor Jin Zhong Zhang and Professor Scott R. J. Oliver, for their time, support, and guidance throughout my Ph.D. study. I am also grateful to Dr. Cheng Zhu, who served as an outside committee member for my qualifying exam. I truly appreciate the time my committee members spent participating in my annual reviews over the years. They always listened carefully to my research updates and gave me many helpful comments and suggestions. The questions they asked often helped me think more carefully about my work and better understand what could be improved. Their feedback helped me look at my research from different perspectives and improve the quality of both my projects and this dissertation. I am very thankful for the time and effort they devoted to supporting my academic progress.

My sincere thanks also go to all the current and former members of the Yat Li group. It has been a great honor to work with so many talented and dedicated people, including Dr. Shanwen Wang, Dr. Mingpeng Chen, Dr. Dun Lin, Professor Tianyi Kou, Professor Gongming Wang, Dr. Bin Yao, Dr. Megan Freyman, Dr. Anica Pinongcos, Dr. Samuel Eisenberg, Xinzhe Xue, Ella Davide, Cassidy Tran, and Nathan Delney. Thank you for all the discussions, technical help, support, and friendship over the years. I have learned so much from working with all of you, and I truly appreciate the supportive and collaborative environment in the lab. I would also like to thank the undergraduate students from the Li lab, including Jori Steinle,

Logan Valdovinos, Malia Parra, Isaac Loke, Samuel Avalos, Angel Maqueda Alvarado, Marisa Hertzog, Elken Liu, Omar Sanchez, Willa James Swanson, Cameron Ho, Emma Coester, and Ashley Middling, as well as the high school student interns who worked with me during the summers, including Asa Ashley, Brandon Bao, Jerry Chen, Calixte De Belloy De Saint Lienard, Riana Kuçi, Victoria Reyes Holguin, April Chen, Jianan Wang, and Tomas James Mercado. It was a meaningful experience to work with and mentor all of you. Your hard work, curiosity, and enthusiasm also helped me grow as a mentor and communicator.

I am also thankful to my collaborators and colleagues who contributed to different parts of this work, including Professor Xiao Wang, Professor Tianyi Kou, Dr. Zhen Liu, Dr. Longsheng Feng, Dr. Cheng Zhu, Dr. Eric B Duoss, Dr. Fang Qian and Dr. Congwang Ye. I would also like to thank Dr. Tom Yuzvinsky for his help with SEM characterization, Dr. Brian Dreyer for his support with ICP-OES measurements, and Dr. Ilkeun Lee at UC Riverside and Dr. Kennedy Nguyen at UC Merced for their help with XPS characterization. Their efforts, support, and valuable discussions made this research possible and made my Ph.D. journey more meaningful.

My appreciation also extends to the faculty, staff, and friends in the Department of Chemistry and Biochemistry at UC Santa Cruz, including Alissa Nolan, Dr. Panpan Zhang, Dr. Kai-chun Chou, Dr. Bingzhe Yu, Dr. Dingjie Pan, Tianchen Cui, and Riley Ball. Their help, kindness, and support made my graduate life much smoother and more enjoyable. I am also thankful for all the teaching opportunities I had during my Ph.D. These experiences allowed me to work with

many wonderful students and helped me grow not only as a researcher, but also as a mentor, teacher, and communicator.

I am especially grateful to my master's advisor, Professor Xiaoming Ren. During my master's study, he gave me a great deal of support and guidance in both my research and personal life. He helped me develop my research skills, encouraged me when I faced difficulties, and gave me many valuable suggestions on my projects. His support and trust were very important to my growth at that stage and also helped prepare me for my Ph.D. study. I am truly thankful for everything he has done for me and for the care and encouragement he has given me over the years.

Special thanks go to my friends, both inside and outside the university, including Dr. Jingwei Yu, Chengyi Liu, Dr. Gan Shen, Dr. Jin Zhang, Dr. Dongsheng Shao, Dr. Yanyan Fang, Dr. Cong Wei, Dr. Bo Liu, Xuanwei Yin, Zenan Bian, Dr. Wanwan Yao, Jin Zhang, Shu Wang, Dr. Yi Liu, Qingtian Wang, Yuxiang Zhao, Dongyi Liu, Yuzhuo Song, Renlong Chen and Miaofei Yin. Thank you for your companionship, encouragement, and all the moments that made these years memorable. Graduate school was not always easy, but your support helped me get through many difficult times and made this journey much more meaningful.

Most importantly, I would like to thank my family for their unconditional love, understanding, and support. I am deeply grateful to my parents, Changming Ren and Yuxia Yang. Since coming to the United States for my Ph.D., I have not had the chance to return to China to visit them. Being far away from home for so many years has not been easy, and I often feel sorry that I could not be by their side. However, their love, trust, and encouragement have always given me strength, especially during the most difficult moments of my graduate study. Their sacrifices

and support made it possible for me to pursue this journey, and words cannot fully express how thankful I am.

I would also like to thank my other family members, including Xiaoming Ren, Guiming Ren, Changlin Ren, Manlin Ren, Min Yao, Guiying Cheng, Wenxiang Li, Haiyan Si, Ling Ren, Jin Ren, Lite Ren, Qianqian Ren, Zhiheng Ren, Fei Ren, and Weike Wang. Even though we have often been far apart, your care and encouragement have always meant a great deal to me. I could not have completed this journey without your trust, patience, and love.

This text of this dissertation includes reprints of the following previously published or subsequently published materials:

1. **Ren, Q**., Feng, L., Ye, C., Xue, X., Lin, D., Eisenberg, S., Kou, T., Duoss, E.B., Zhu, C., Li, Y., *Adv. Energy Mater.,* **2023** 13, 2302073.
2. **Ren, Q**., Feng, L., Tran, C., Eisenberg, S., Xue, X., Pinongcos, A., Duoss, E.B., Zhu, C., Li, Y., *ACS Mater. Lett.,* **2024**, 6, 3705-3712.
3. **Ren, Q**., Tran, C., Zhang, K., Zhu, C., Li, Y., *Nanoscale*, **2025**, 17, 3600.
4. **Ren, Q**., Delaney, N., Liu, Z., Tran, C., Eisenberg, S., Alvarado, A.M., Zhu, C., Xin, Y., Zhang, D., Liang, G., Kou, T., Wang, X., Li, Y., *Small*, **2026**, e73847.

Chapter 1

Introduction of Electrochemical Water Splitting

Abstract

Hydrogen is considered a promising clean energy carrier because of its high gravimetric energy density and carbon-free emission during use. However, hydrogen does not naturally exist as a free gas in large quantities and must be produced from hydrogen-containing compounds. At present, most hydrogen is produced through fossil-fuel-based processes, which are well established but generate greenhouse gases and other pollutants. In contrast, electrochemical water splitting provides a more sustainable strategy for hydrogen production because water serves as the hydrogen source and the required electricity can be supplied by renewable energy sources such as solar and wind power.

This chapter introduces the background and fundamentals of electrochemical water splitting. First, the motivation for green hydrogen production is discussed, followed by a comparison of major water splitting technologies, including alkaline water splitting, proton exchange membrane electrolysis, and solid oxide electrolysis cells. The basic reaction mechanisms of the hydrogen evolution reaction and oxygen evolution reaction are then summarized. Special attention is given to high-rate water splitting, where practical operation requires high current density, long-term stability, and low cell voltage. Under these conditions, gas bubble accumulation, ion-diffusion limitations, and sluggish oxygen evolution kinetics become major challenges. Finally, strategies such as electrode architecture design, surface/interface engineering, catalyst modification, and the use of alternative

anodic oxidation reactions are introduced as important approaches to improve the efficiency and durability of electrochemical hydrogen production.

1.1 Background

Fossil fuels, including coal, petroleum, and natural gas, have been the major energy sources supporting industrial development and modern society for more than a century. However, the rapid growth of the global population and economy has greatly increased energy consumption and accelerated the depletion of fossil fuel reserves. Since fossil fuels require geological timescales to form, they are nonrenewable on a human timescale. Their extensive use also releases large amounts of greenhouse gases and pollutants, leading to serious environmental and climate concerns. These issues have motivated the search for cleaner and more sustainable energy sources.[1]

Hydrogen has received increasing attention as a clean energy carrier because of its high gravimetric energy density and carbon-free nature during use.[2] When produced from renewable energy, hydrogen can also serve as a way to store intermittent electricity from solar and wind power in the form of chemical energy. Therefore, sustainable hydrogen production is considered an important component of future low-carbon energy systems. However, most hydrogen is still produced through fossil-fuel-based processes, which limits its environmental benefits.[3] Developing efficient and sustainable routes for green hydrogen production is therefore essential.

Electrochemical water splitting is one of the most promising technologies for producing green hydrogen.[4] In this process, water is converted into hydrogen and oxygen using electricity. When the electricity is supplied by renewable sources,

water splitting provides a direct pathway to generate hydrogen with zero carbon emissions. Compared with fossil-fuel-based hydrogen production, electrochemical water splitting can operate under relatively mild conditions and can be integrated with renewable electricity sources, making it an attractive strategy for sustainable energy conversion and storage.

1.2 Water splitting technologies

Several water splitting technologies have been developed, including proton exchange membrane electrolysis, alkaline water splitting, and solid oxide electrolysis cells.[5] Although these systems differ in electrolyte, membrane, operating temperature, and electrode materials, they share the same basic principle: the hydrogen evolution reaction occurs at the cathode, while the oxygen evolution reaction occurs at the anode.

Proton exchange membrane electrolysis generally operates under acidic conditions and uses a proton-conducting polymer membrane. The high proton conductivity of the membrane allows PEM electrolyzers to operate at high current densities with relatively low ohmic losses. However, the acidic environment requires noble-metal-based catalysts, such as Pt for the hydrogen evolution reaction and Ir- or Ru-based oxides for the oxygen evolution reaction.[6] The high cost and limited abundance of these materials remain major barriers to large-scale deployment.

In contrast, alkaline water splitting is more cost-effective because it can use non-precious-metal electrodes and more affordable separators or diaphragms in alkaline electrolytes. Nickel-based materials, in particular, have been widely used and investigated as promising electrodes for alkaline water electrolysis. However,

compared with PEM systems, alkaline electrolyzers often suffer from slower reaction kinetics, higher ionic resistance, and more pronounced mass-transport limitations, especially under high-current-density operation. These issues can increase the required cell voltage and reduce energy efficiency.[7]

Solid oxide electrolysis cells operate at much higher temperatures, typically several hundred degrees Celsius. The high operating temperature can improve reaction kinetics and energy efficiency, but it also creates challenges related to material degradation, thermal stability, sealing, and long-term durability.[8] Therefore, although solid oxide electrolysis cells technology is promising, further improvements in materials stability and system lifetime are still needed.

Among these technologies, alkaline water splitting is particularly attractive for large-scale hydrogen production because of its low cost and compatibility with earth-abundant catalysts. However, achieving efficient and stable alkaline water splitting at industrially relevant current densities remains challenging. This challenge motivates the development of advanced catalysts, electrode architectures, and electrode-electrolyte interfaces.

1.3 Fundamentals of water splitting

Water splitting consists of two half-cell reactions: the hydrogen evolution reaction (HER) at the cathode and the oxygen evolution reaction (OER) at the anode. The overall efficiency of water splitting depends not only on the intrinsic kinetics of these reactions, but also on charge transfer, ion transport, electrolyte accessibility, and gas product removal.

1.3.1 Hydrogen evolution reaction

The HER is a two-electron process that produces hydrogen gas at the cathode.[9] The reaction pathway depends strongly on the pH of the electrolyte. In acidic media, abundant protons are available, and HER generally proceeds through hydrogen adsorption followed by hydrogen molecule formation:

Volmer step:

$* + H^+ + e^- \rightarrow H*$

Heyrovsky step:

$H* + H^+ + e^- \rightarrow H_2 + *$

Or Tafel step:

$2H* \rightarrow H_2 + 2*$

In alkaline and neutral media, the concentration of free protons is much lower. Therefore, water molecules must first dissociate to generate adsorbed hydrogen intermediates:

Volmer step:

$H_2O + * + e^- \rightarrow H* + OH^-$

Heyrovsky step:

$H_2O + H* + e^- \rightarrow H_2 + OH^- + *$

Or Tafel step:

$2H* \rightarrow H_2 + 2*$

Here, * represents an active site on the catalyst surface, and H* represents an adsorbed hydrogen intermediate. The binding strength of H* is a key descriptor for HER activity. According to Sabatier principle, an efficient HER catalyst should bind

hydrogen neither too strongly nor too weakly.[10] If the hydrogen binding is too weak, hydrogen adsorption becomes difficult. If the binding is too strong, hydrogen desorption or H-H bond formation becomes limited. Therefore, optimizing hydrogen adsorption free energy is essential for improving HER kinetics.

In alkaline media, HER is generally slower than in acidic media because water dissociation is required before hydrogen formation. As a result, the design of alkaline HER catalysts must consider not only hydrogen adsorption, but also water activation and hydroxide desorption.

1.3.2 Oxygen evolution reaction

The OER is the anodic half reaction of the overall water splitting reaction. Unlike the HER, which is a two-electron transfer reaction, the OER is a multi-electron transfer reaction which involves a total of four electrons.[11] In acidic media, the steps of one proposed mechanism are as follows:

$* + H_2O \rightarrow *OH + H^+ + e^-$

$*OH \rightarrow *O + H^+ + e^-$

$*O + H_2O \rightarrow *OOH + H^+ + e^-$

$*OOH \rightarrow * + O_2 + H^+ + e^-$

The steps are slightly different in alkaline and neutral media and are as follows:

$* + OH^- \rightarrow *OH + e^-$

$*OH + OH^- \rightarrow *O + H_2O + e^-$

$*O + OH^- \rightarrow *OOH + e^-$

$*OOH + OH^- \rightarrow * + O_2 + H_2O + e^-$

The formation and transformation of adsorbed intermediates, including *OH, *O, and *OOH, strongly influence OER kinetics. Because these elementary steps require multiple proton-coupled electron-transfer processes, OER typically shows larger overpotentials and slower kinetics than HER. Therefore, highly active OER catalysts are needed to reduce the cell voltage and improve the energy efficiency of water electrolysis. Noble-metal oxides such as IrO_2 and RuO_2 are among the most active OER catalysts, especially in acidic media.[12] However, their high cost and limited abundance restrict their large-scale use. In alkaline media, transition-metal-based catalysts, especially Ni-, Fe-, and Co-based oxides, hydroxides, and oxyhydroxides, have been widely investigated as cost-effective alternatives. Among them, NiFe-based oxyhydroxides are considered benchmark alkaline OER catalysts because of their high activity and relatively low cost.

1.4 High-rate water splitting

For industrial applications, it is essential to develop electrode materials that can perform effectively under industry-relevant conditions, such as high current density, extended operational periods, and specific pressure and temperature requirements. High current density is particularly important because it increases the rate of hydrogen production, which can reduce capital costs and improve the profitability of hydrogen production.[13]

The ability to produce hydrogen at high rates is vital to effectively meet the growing demand for hydrogen in various applications, including hydrogen-powered fuel cell vehicles, ammonia production, and fuel cell related energy storage systems.[14] Various governments and organizations have established technical targets for high-rate water splitting to address different application needs. For

example, the U.S. Department of Energy (DOE) has set ambitious targets for PEM water splitting.[15] By 2026, the DOE aims to achieve a current density of 3000 mA cm^{-2} at a cell voltage of 1.8 V, with a long-term goal of reaching 3000 mA cm^{-2} at 1.6 V. Similarly, the Fuel Cells and Hydrogen Joint Undertaking (FCH JU) in Europe has set broader targets,[16] aiming for a current density of 800 mA cm^{-2} for alkaline water splitting and 2500 mA cm^{-2} for PEM water splitting by 2030. These targets are part of a broader strategy to enhance performance and reduce the costs of hydrogen production technologies, making them more accessible and practical for widespread use. However, achieving high current densities can accelerate the degradation of electrode materials, highlighting the need for more robust and durable catalysts and electrodes. Research efforts have been focused on developing advanced catalysts, innovating electrode architectures to improve mass transport and reduce overpotentials and integrating electrolysis systems with renewable energy sources to ensure sustainable hydrogen production. **Table 1.1** summarizes some of the future technical performance targets, which are driving research into electrochemical water splitting under high current density conditions.

Table 1.1. Summary of representative technical performance targets for high-rate water splitting devices.

Source	**Technique**	**Year**	**Current density (mA cm^{-2})**	**Voltage (V)**	**Energy Efficiency (%)**	**Durability (h)**
DOE	PEM	2026	3000	1.8	69	80000
DOE	PEM	Ultimate	3000	1.6	77	80000
FC HJU	PEM	2030	2500	-	-	Degraded by 0.12% per 1000 h

FC HJU	AWS	2030	800	-	-	Degraded by 0.1% per 1000 h

However, achieving these targets is challenging because high-current-density operation introduces severe electrode- and interface-level limitations. These limitations are especially important in alkaline water splitting, where lower-cost non-precious-metal electrodes are attractive but often suffer from slower reaction kinetics and larger transport resistance. In particular, three major issues must be addressed to enable efficient high-rate water splitting: gas bubble accumulation, ion-diffusion limitations, and sluggish oxygen evolution kinetics (**Figure 1.1**).

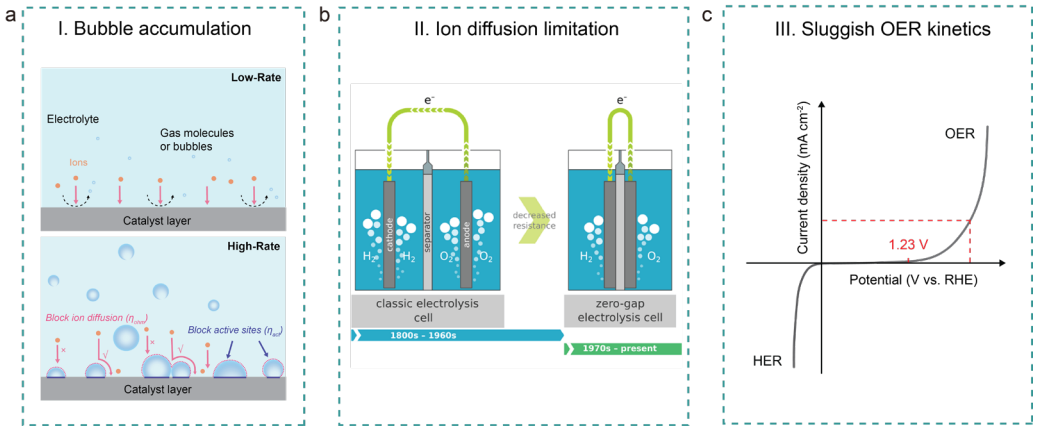

Figure 1.1. Key challenges in high-rate water splitting: (a) gas bubble accumulation, (b) ion-diffusion limitation, and (c) sluggish OER kinetics.

First, rapid gas generation at high current densities leads to extensive bubble formation on electrode surfaces. Accumulated gas product bubbles can block active sites, reduce the effective catalyst-electrolyte contact area, and increase local resistance. Bubble coverage also interrupts electrolyte access to the electrode surface and creates unstable reaction environments. As a result, even if the catalyst

itself is active, poor gas bubble removal can significantly increase the apparent overpotential and lower the overall efficiency. Therefore, promoting fast bubble detachment is essential for maintaining efficient water electrolysis under high-rate conditions.[17]

Second, ion diffusion and electrolyte transport become increasingly important as the reaction rate increases. At low current densities, reactants and ions can usually reach the electrode surface fast enough to sustain the electrochemical reaction. However, under high-current-density operation, rapid consumption and generation of ionic species can create local concentration gradients within the electrode and electrolyte. In porous or thick electrodes, insufficient electrolyte penetration and tortuous ion-transport pathways can further increase concentration polarization and ohmic resistance. These effects limit the accessible active surface area and reduce the benefit of increasing catalyst loading or geometric surface area.[18]

Third, the OER remains a major kinetic bottleneck in overall water splitting. Compared with HER, OER involves a four-electron transfer process and multiple oxygen-containing intermediates, leading to intrinsically sluggish kinetics and large overpotentials. This issue becomes more significant at high current densities, where faster charge transfer is required to sustain rapid oxygen production. Therefore, developing efficient OER catalysts is an important strategy to lower the anodic overpotential and improve the energy efficiency of water electrolysis. In alkaline media, transition-metal-based catalysts have been widely studied as promising alternatives to noble-metal oxides. In addition to improving OER catalysts, another effective strategy is to replace the OER with alternative anodic oxidation reactions that require lower thermodynamic potentials and faster reaction kinetics. For

example, the urea oxidation reaction has a much lower theoretical potential than OER and can reduce the overall energy input for hydrogen production when coupled with the HER at the cathode. This approach not only improves the energy efficiency of hydrogen generation, but also provides a potential route for treating urea-containing wastewater. Therefore, integrating low-energy anodic reactions with water electrolysis offers a promising direction for sustainable hydrogen production.[19]

References

1. Yu, Z.-Y.; Duan, Y.; Feng, X.-Y.; Yu, X.; Gao, M.-R.; Yu, S.-H., *Adv. Mater.* **2021,** *33* (31), 2007100.

2. Jin, H.; Wang, J.; Su, D.; Wei, Z.; Pang, Z.; Wang, Y., *J. Am. Chem. Soc.* **2015,** *137* (7), 2688-94.

3. Qian, Q.; Zhu, Y.; Ahmad, N.; Feng, Y.; Zhang, H.; Cheng, M.; Liu, H.; Xiao, C.; Zhang, G.; Xie, Y., *Adv. Mater.* **2024,** *36* (4), e2306108.

4. Wang, J.; Cui, W.; Liu, Q.; Xing, Z.; Asiri, A. M.; Sun, X., *Adv. Mater.* **2016,** *28* (2), 215-30.

5. Liu, R. T.; Xu, Z. L.; Li, F. M.; Chen, F. Y.; Yu, J. Y.; Yan, Y.; Chen, Y.; Xia, B. Y., *Chem. Soc. Rev.* **2023,** *52* (16), 5652-5683.

6. Sun, P.; Qiao, Z.; Dong, X.; Jiang, R.; Hu, Z.-T.; Yun, J.; Cao, D., *J. Am. Chem. Soc*. **2024,** *146* (22), 15515-15524.

7. Tuysuz, H., Alkaline Water Electrolysis for Green Hydrogen Production. *Acc. Chem. Res.* **2024,** *57* (4), 558-67.

8. Wang, Z. X.; Wang, Y.; Li, N. Z.; Tong, Y. C.; Teng, Y.; Wang, D.; Chen, C. S.; Zhan, Z. L., *Int. J. Hydrogen Energy* **2023,** *48* (35), 12949-12957.

9. Li, Y.; Peng, Y.; Dong, W.; Jiang, X.; Lu, L.; Yang, D.; Hsu, L. C.; Li, W.; Su, B.; Lei, A., J. Am. Chem. Soc. 2024, 146 (20), 14194-14202.

10. Shi, Z.; Li, J.; Wang, Y.; Liu, S.; Zhu, J.; Yang, J.; Wang, X.; Ni, J.; Jiang, Z.; Zhang, L.; Wang, Y.; Liu, C.; Xing, W.; Ge, J., *Nat. Commun.* **2023,** *14* (1), 843.

11. Carmo, M.; Fritz, D. L.; Merge, J.; Stolten, D., *Int. J. Hydrogen Energy* **2013,** *38* (12), 4901-4934.

12. Xu, H.; Zhang, J.; Eikerling, M.; Huang, J., *J. Am. Chem. Soc.* **2024,** *146* (29), 19720-19727.

13. Luo, Y.; Zhang, Z.; Chhowalla, M.; Liu, B., *Adv. Mater.* **2022,** *34* (16), e2108133.

14. Zhang, X.; Jin, M. T.; Jia, F. F.; Huang, J. Q.; Amini, A.; Song, S. X.; Yi, H.; Cheng, C., *Energy Environ. Mater.* **2023,** *6* (5), e12457.

15. Technical Targets for Proton Exchange Membrane Electrolysis. https://www.energy.gov/eere/fuelcells/technical-targets-proton-exchange-membrane electrolysis.

16. Annual Work Plan 2014-2020. https://www.fch.europa.eu/page/multi-annual-work-plan.

17. Ren, Q.; Tran, C.; Zhang, K.; Zhu, C.; Li, Y., *Nanoscale*, **2025**, 17, 3600.

18. Hodges, A.; Hoang, A.L.; Tsekouras, G.; Wagner, K., Lee; C.Y., Swiegers, G.F.; Wallace, G.G., *Nat. Commun.* **2022**, 13, 1304.

19. Xu, W.; Lu, Z.; Sun, X.; Jiang, L.; Duan, X., *Acc. Chem. Res.* **2018**, 51, 1590.

Chapter 2

Nanocone-Modified Surfaces for Enhanced Bubble Detachment in High-Rate Alkaline Water Splitting

2.1 Abstract

Hydrogen production through alkaline water splitting is regarded as a promising and sustainable technology for a clean energy economy. However, under industrially relevant current density conditions ($\approx$ 1000 mA cm^{-2}), severe gas bubble accumulation on the electrode surface hinders catalytic activity, restricts mass transport, and can even damage the catalyst layer. This chapter presents a surface engineering strategy in which nickel substrates are modified with nanocone structures to promote rapid gas bubble detachment. The nanocone-modified electrodes exhibit superaerophobicity, leading to faster bubble release and smaller bubble detachment sizes compared to unmodified electrodes. Both simulations and high-speed imaging confirm reduced adhesion forces and enhanced detachment dynamics. Electrochemical measurements further demonstrate significantly reduced overpotentials at high current densities, along with excellent long-term stability in two-electrode water-splitting devices. These findings establish nanocone surface modification as an effective and generalizable approach for mitigating bubble accumulation, thereby enabling efficient and stable hydrogen production at ultrahigh current densities.

2.2 Introduction

The growing demand for renewable and carbon-free energy sources has positioned hydrogen as a key energy carrier in the transition toward sustainable technologies.[1-3] Among various production routes, alkaline water splitting provides

an attractive method for large-scale hydrogen generation due to its reliance on earth-abundant catalysts and system durability.[4, 5] Nevertheless, commercial alkaline water splitting electrolyzers typically operate at modest current densities of around 400 mA cm^{-2}, which limits hydrogen production rates compared to proton-exchange membrane electrolyzers.[6] To achieve industrially relevant outputs, it is necessary to raise the current density of alkaline water splitting systems to approximately 1000 mA cm^{-2} or higher.[7, 8]

A major obstacle at these high current densities is the excessive formation and accumulation of gas bubbles on electrode surfaces,[9, 10] adherent bubbles can disrupt or damage surface layers block active sites, obstruct ion and electrolyte diffusion, and increase ohmic resistance, all of which reduce catalytic efficiency.[11] Furthermore, the detachment of large coalesced bubbles can disrupt or damage catalyst layers, threatening electrode stability. While strategies such as forced electrolyte flow, acoustic fields, or magnetic assistance have been explored to remove bubbles, these approaches generally involve additional energy consumption or complex system designs.[12-14]

An alternative and potentially more practical solution is to modify the electrode surface to enhance bubble detachment through structural and chemical design. Previous studies have demonstrated that nanostructured surfaces, superaerophobic coatings, and optimized electrode architectures can reduce bubble adhesion force and promote their release.[15-18] Inspired by these insights, this chapter investigates the use of nickel nanocone surface modification as a versatile strategy to address bubble accumulation on the electrode surface. Unlike catalyst redesign, which alters intrinsic catalytic activity, nanocone modification relies on

morphological control of the electrode surface, allowing improved bubble dynamics without fundamentally changing the material's composition.

2.3 Experimental section

2.3.1 Preparation of nickel nanocone-modified electrodes

Nickel nanocone structures were synthesized on various nickel substrates, including nickel foil, nickel foam, and 3D-printed nickel lattices (denoted as Foil, Foam, and Lattice), using an electrodeposition method.[19] Prior to deposition, the substrates were cut into 1 × 1 cm pieces and sequentially cleaned by ultrasonication in acetone, 3.0 M HCl, deionized (DI) water, and ethanol for 10 min each, followed by drying under ambient conditions. The electrodeposition bath contained 0.84 M $NiCl_2$, 1.0 M H_3BO_3, and 1.4 M NH_4Cl in DI water, with the pH adjusted to 4.0 using 10 wt% NaOH solution. A conventional three-electrode configuration was used, with the nickel substrate as the working electrode, Ag/AgCl as the reference electrode, and a piece of Ni foam (2 × 3 cm) as the counter electrode. Electrodeposition was performed at a constant current density of 20 mA cm^{-2} for 8 min at 60 °C. The resulting nanocone-modified nickel-based substrates (denoted as Foil_NC, Foam_NC, and Lattice_NC) were rinsed with DI water and ethanol, then dried at ambient conditions.

2.3.2 Fabrication of 3D-printed nickel lattice electrodes

Three-dimensional nickel lattice structures were fabricated using a direct ink writing method. The printing ink was prepared by dispersing 26.7 g of nickel powder (3-7 μm, Alfa Aesar) in a polymeric solution composed of polylactic-co-glycolic acid (PLGA) dissolved in dichloromethane (DCM). Ethylene glycol butyl ether (EGBE) was added to adjust the viscosity and volatility. The slurry was

homogenized using a planetary mixer to achieve a solid loading of 40-50 vol%. The ink was then extruded through a 200 μm nozzle using a pneumatic dispenser onto silicon wafers, guided by a computer-controlled three-axis stage. The printed lattices were dried in air and subjected to thermal treatment at 300 and 600 °C in hydrogen to remove organics, followed by annealing at 900 °C in argon to obtain metallic nickel lattices. The final structures exhibited dimensions of approximately 10 × 10 × 3 mm with less than 10% linear shrinkage.

2.3.3 Structural and surface characterization

The morphology of pristine and nanocone-modified substrates was characterized by scanning electron microscopy (SEM, Hitachi S-4800 II). Crystal structures were analyzed by X-ray diffraction (XRD, Rigaku SmartLab) using Cu Kα radiation, with standard nickel diffraction peaks provided for reference. Surface chemical states were examined by X-ray photoelectron spectroscopy (XPS, Kratos AXIS Ultra DLD).

Wettability was evaluated by measuring the underwater air bubble contact angle. The nickel foil and nanocone-modified nickel foil substrates were horizontally immersed in a water-filled quartz cell, and a bubble of controlled size was introduced beneath the surface. The air-solid contact angle was recorded with a goniometer (Ossila) and analyzed using the accompanying software.

2.3.4 Simulation of bubble detachment dynamics

Bubble detachment behavior on flat and cone-decorated surfaces was investigated using a Shan-Chen type multiphase multicomponent lattice Boltzmann model, implemented with the Palabos package.[20, 21] The model accounted for fluid-fluid interactions, fluid-solid adhesion, and gravitational forces. The simulation

domain dimensions were set to 150 × 100 × 100, with a substrate thickness of 30 units. For cone-decorated surfaces, the cone geometry was defined by a base radius of 10 units and a height of 30 units. Model parameters, including cohesion and adhesion strengths, were selected based on established literature values (**Table 2.1**).

Table 2.1. Input parameters of the Shan-Chen model used in the simulation.

Equilibrium fluid density ρ_1 and ρ_2	2.0
Relaxation time τ	1.0
Dissolved density $\rho_{d,1}$ and $\rho_{d,2}$	0.06
Cohesion force strength G_c	0.9
Applied gravitational force F_g	10^{-4}
Convergence threshold ϵ	5×10^{-6}
Adhesion parameter $G_{ads,1}$	0.4
Adhesion parameter $G_{ads,2}$	-0.4

2.3.5 High-speed imaging of bubble evolution

Bubble evolution during the HER and OER was recorded using a high-speed camera (Photron NOVA S9) coupled with a macro lens. Electrochemical cells with transparent quartz walls were used to minimize optical distortion. The frame rate was set to 60 fps, with a shutter speed of 1 ms. The working electrode (Foil or Foil_NC, 1 × 1 cm) was placed vertically in the electrolyte, while Hg/HgO and graphite served as the reference and counter electrodes, respectively. Illumination was provided by LED lamps.

2.3.6 Electrochemical measurements

Electrochemical performance was evaluated in 1.0 M KOH solution using a CHI 660D workstation. Linear sweep voltammetry (LSV) was performed at 0.1 mV s^{-1} after cyclic voltammetry (CV) activation. For HER, CV activation was

conducted between -0.6 and -1.35 V vs Hg/HgO for 50 cycles; for OER, the potential window was 0-0.8 V for 20 cycles. Electrochemical impedance spectroscopy (EIS) was performed at -1.08 V (HER) and 0.7 V (OER) over a frequency range of 100 kHz to 1 Hz, with a 5 mV perturbation. An 85% iR compensation was applied.

The electrochemically active surface area (ECSA) was determined from the capacitive current associated with double-layer charging, extracted from CV at scan rates of 20-100 mV s^{-1}. The ECSA values of HER and OER test were determined using a method previously reported.[22] Specifically, a series of CV curves were collected in a potential window from 0.417 to 0.517 V vs. RHE where no Faradaic reaction occurred. The scan rate varied from 20 to 100 mV at an interval of 20 mV s^{-1}. A linear plot was generated from the difference between j_{anodic} and $j_{cathodic}$ (at 0.464 V vs. RHE) versus scan rate, and the slope of this plot is proportional to the ECSA. The ECSA of each sample was calculated based on the following equation (**Equation 2.1**):

$$ECSA = \frac{C_{area} \times A}{C_{ref}} \qquad \textbf{(Equation 2.1)}$$

Where, C_{area} is the areal capacitance, which is half the slope of the generated plot, A is the geometric area of the electrode, and C_{ref} is the reference areal capacitance for Ni (40 μF cm^{-2}).[23] For the ECSA of OER tests, similar scan-rate-dependent measurements were conducted in a potential window from 1.017 to 1.117 V vs. RHE. A linear plot was generated from the difference between j_{anoidc} and $j_{cathodic}$ at 1.067 V vs. RHE and scan rate to determine ECSA by using the same equation.

Stability tests were conducted using two-electrode configurations with Lattice_NC electrodes as both anode and cathode. Chronoamperometry was recorded at a fixed voltage of 2.45 V at room temperature for up to 100 h.

2.4 Results and discussion

2.4.1 Surface morphology and structural characterization

To establish the structural features of the nanocone-modified electrodes, scanning electron microscopy (SEM) was employed to compare pristine nickel substrates with those after nanocone growth. As shown in **Figure 2.1**, all untreated nickel substrates exhibited relatively smooth surfaces with only minor surface irregularities, whereas the nanocone-modified samples were uniformly covered with a dense array of vertically aligned nanocones. The nanocones possessed base diameters in the range of approximately several hundred nanometers and displayed consistent coverage across different types of nickel substrates, including Foil, Foam and Lattice. This uniformity demonstrates the versatility of the electrodeposition method for modifying both planar and more complex 3D architectures. Such a pronounced morphological transformation not only increases the surface roughness but also introduces a hierarchical texture that is expected to strongly influence bubble-surface interactions, reduce adhesive forces, and facilitate rapid bubble detachment during high-rate water splitting.

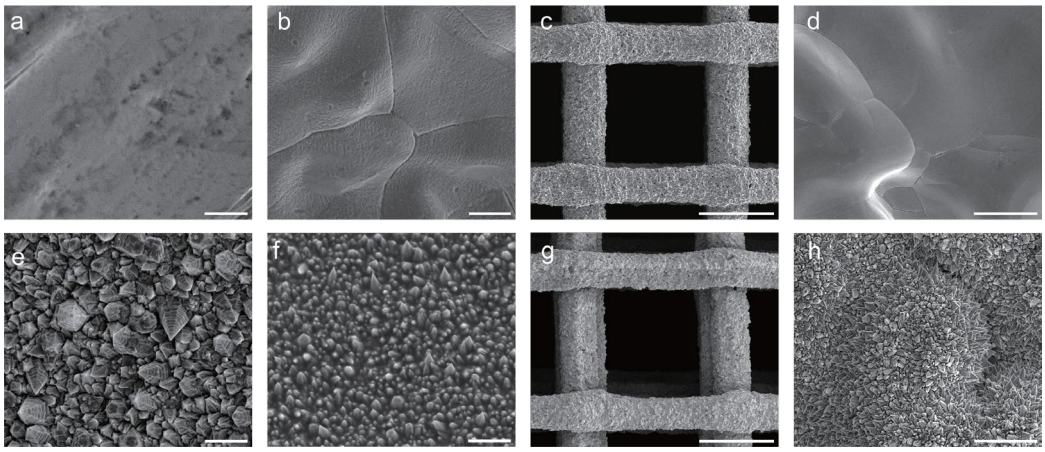

Figure 2.1. SEM images of (a) Foil and (e) Foil_NC; (b) Foam and (f) Foam_NC; and 3D-printed Ni lattice (c, d) before and (g, h) after nanocone modification. Scale bars are 1 μm for (a, b, e, f), 300 μm for (c, g), and 1 μm for the magnified images in (d, h).

X-ray diffraction (XRD) patterns were collected to confirm the crystallographic nature of the deposited nanocones. To eliminate interference from the strong background of Ni substrates, nanocones were first deposited on carbon paper using the same electrodeposition method. As shown in **Figure 2.2a**, the resulting sample exhibited three prominent diffraction peaks at 44.5°, 51.8°, and 76.4°, corresponding to the (111), (200), and (220) planes of metallic Ni. This result confirms that the electrodeposited nanocones are indeed nickel in composition. Subsequently, XRD patterns of nanocone-modified foil, foam, and 3D-printed lattice electrodes were collected (**Figure 2.2b**). All three substrates displayed the same characteristic Ni reflections, consistent with both the pristine nickel substrates and the standard Ni reference (PDF#04-0850). The close agreement of peak positions and intensities confirms that the nanocone deposition process preserved

the metallic nickel phase and did not introduce any detectable secondary phases or impurities.

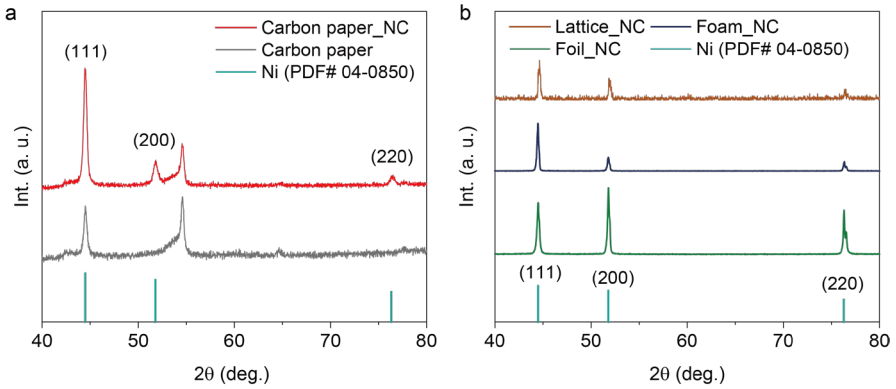

Figure 2.2. XRD patterns of (a) carbon paper and nanocone-modified carbon paper (Carbon paper_NC), and (b) Foil_NC, Foam_NC, and Lattice_NC. The standard Ni diffraction pattern (PDF# 04-0850) is included for reference.

X-ray photoelectron spectroscopy (XPS) was further conducted to probe the surface chemical states of the electrodes before and after nanocone modification (**Figure 2.3**). Both pristine and nanocone-modified samples exhibited broad Ni 2p spectra with a main peak centered at ≈855.3 eV, accompanied by a satellite feature at ≈861.4 eV. Deconvolution of the spectra revealed contributions from metallic Ni (≈853.3 eV), Ni^{2+} (≈855.2 eV), and Ni^{3+} (≈856.7 eV) species, consistent with previously reported nickel-based catalysts.[24] The overall spectral profiles and relative peak intensities were nearly identical for pristine and nanocone-modified electrodes, indicating that the electrodeposition process does not significantly alter the oxidation states or electronic structure of surface nickel. This finding, combined with the XRD results, suggests that the intrinsic catalytic chemistry of the electrode remains unchanged after nanocone growth. Therefore, the performance

enhancement observed in subsequent electrochemical measurements can be attributed primarily to morphological effects, namely, increased surface roughness and altered bubble-surface interactions, rather than compositional differences.

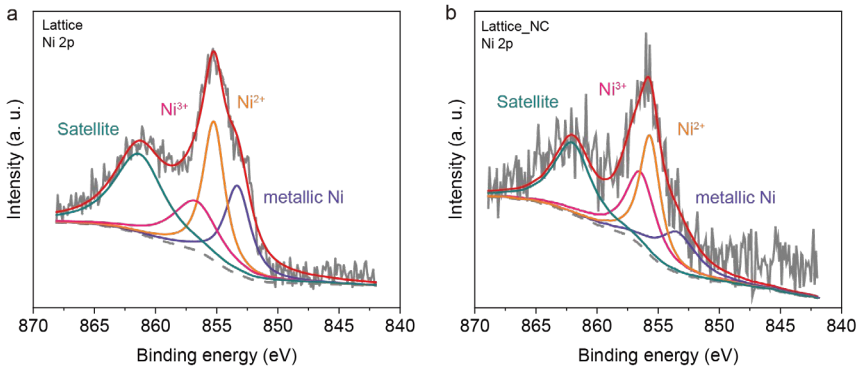

Figure 2.3. Ni 2p XPS spectra of (a) Lattice and (b) Lattice_NC.

Finally, the wettability of the electrodes toward air bubbles was assessed using air contact angle measurements. The pristine foil exhibited an underwater air contact angle of 134.6°, whereas the nanocone-modified foil displayed a substantially larger angle of 151.8° (**Figure 2.4**). This increase indicates that the nanocone-nanocone modified surface is highly superaerophobic, reducing the adhesive interaction between bubbles and the electrode. These findings collectively demonstrate that nanocone modification alters surface roughness and aerophobicity without changing the fundamental chemical composition of the electrode, thereby providing an ideal platform to investigate bubble detachment dynamics.

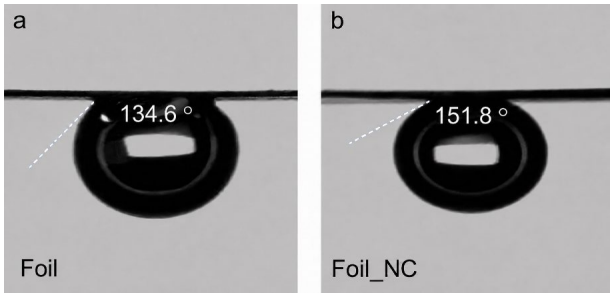

Figure 2.4. Digital images showing the air contact angles on (a) Foil and (b) Foil_NC.

2.4.2 Bubble detachment dynamics: simulation insights

To elucidate the role of nanocone morphology in bubble detachment, computational simulations were performed using a Shan-Chen-type multiphase multicomponent lattice Boltzmann model.[20, 21] This approach allows for the mesoscale representation of bubble-liquid-solid interactions, accounting for buoyancy, adhesion, and interfacial tension forces. In the simulations, a single bubble was positioned on either a flat nickel substrate or a cone-decorated surface, and the attachment time (t_A) was monitored under varying initial penetration depths (h/h_0) into the surface features.

The results, shown in **Figure 2.5**, reveal significant differences between the two surface types. On flat surfaces, bubbles remained attached throughout the simulation, indicating strong adhesion that resisted buoyant forces. In contrast, bubbles placed on cone-decorated surfaces detached significantly earlier, with detachment time decreasing as the initial depth into the cones was reduced. For example, bubbles at h/h_0 = 1/3 detached at a normalized time of 0.35, compared to 0.65 for h/h_0 = 1.

These observations can be explained by the Cassie-Baxter wetting model, which describes the influence of surface roughness on apparent contact angle (**Equation 2.2**).[25]

$$cos\alpha^* = f_s(cos\alpha + 1) - 1 \qquad \textbf{(Equation 2.2)}$$

where α^* represents the apparent bubble contact angle on a rough solid surface with liquid, α is the apparent bubble contact angle on a smooth surface, f_s denotes the fraction of the solid in contact with the bubble. Compared to a smooth surface, the surface with nanoarchitectures is expected to have a smaller f_s and, therefore, a higher contact angle and aerophobicity. Furthermore, the diameter of the detached bubble (D_d) is also proportional to the sine function of the bubble contact angle, as shown in **Equation 2.3**.

$$D_d = \sqrt{\gamma} sin\alpha \sqrt{\frac{6}{\rho g}} \qquad \textbf{(Equation 2.3)}$$

$\sqrt{\gamma}$ is the surface tension at TPCL, α is the contact angle between the bubble and the solid surface, ρ and g represent the density of the electrolyte and gravitational acceleration, respectively. According to **Equation 2.3**, the D_d decreases with the increase of α, which is in the range of 90-180 degrees. A superaerophobic surface, which typically has an underwater air bubble contact angle exceeding 150°, can significantly reduce the bubble-solid contact area and adhesive force, thereby facilitate bubble detachment and reducing the bubble size at detachment.

The presence of nanocones reduces the effective solid-gas contact fraction, thereby increasing the apparent contact angle and aerophobicity. In mechanical terms, the adhesion force on a flat surface is aligned opposite to the buoyant force, maximizing resistance to detachment. On cone-decorated surfaces, however, the adhesion force is reoriented at an angle relative to buoyancy, effectively diminishing its magnitude in the vertical direction. As a result, the balance between buoyancy

and adhesion shifts in favor of detachment, leading to smaller bubble sizes and shorter residence times.

These simulation results strongly support the hypothesis that nanocone modification enhances bubble detachment by altering interfacial geometry rather than surface chemistry. This theoretical insight provides a mechanistic foundation for the subsequent experimental studies on bubble dynamics and electrochemical performance.

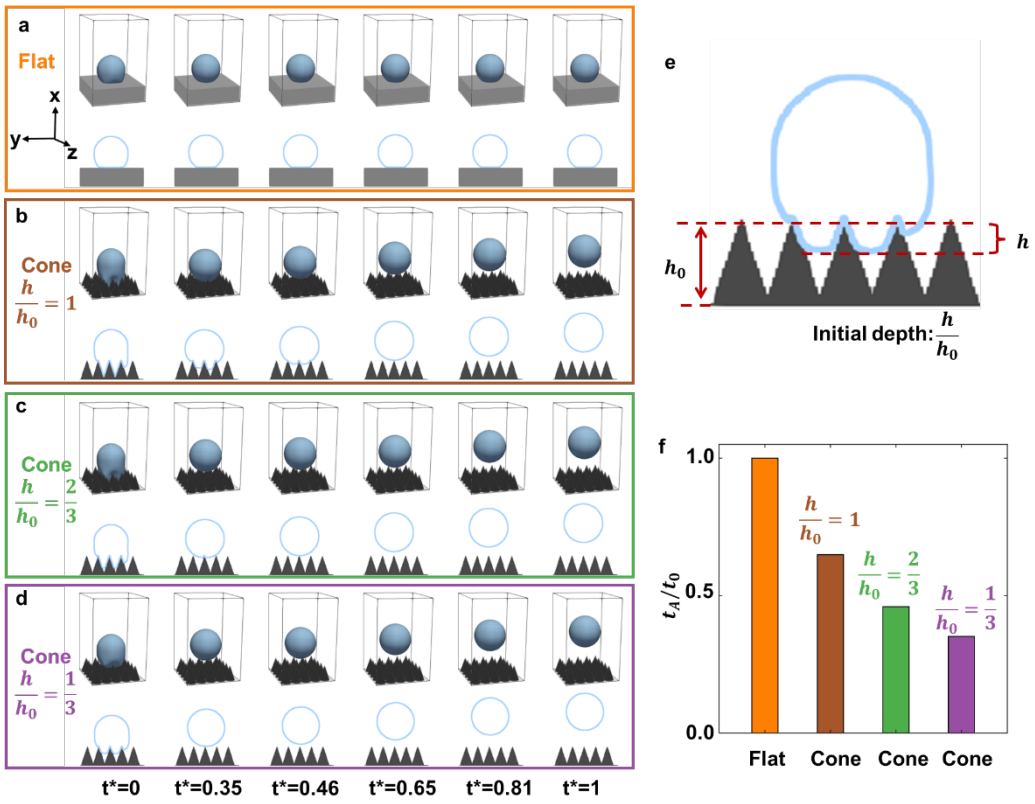

Figure 2.5. Simulation of a single bubble on (a) flat and cone-decorated surfaces with initial depth of (b) $h/h_0 = 1$, (c) $h/h_0 = 2/3$ and (d) $h/h_0 = 1/3$. Normalized simulation time (t*) is labeled for all four cases below (d). (e) Schematic illustration of the initial depth $\frac{h}{h_0}$. (f) Normalized attachment time of the bubble for flat and cone substrates shown a-d.

2.4.3 Experimental observation of bubble evolution

To experimentally verify the influence of nanocone modification on bubble dynamics, high-speed optical imaging was conducted during both the HER and OER. Representative snapshots are shown in **Figure 2.6**. At a current density of 2 mA cm^{-2} for HER, bubbles nucleated, grew, and detached from both pristine and nanocone-modified nickel foils. However, the temporal evolution revealed clear differences between the two surfaces. On the unmodified foil, bubbles remained attached for extended periods, reaching larger sizes before detachment. In contrast, bubbles on the nanocone-modified foil detached more rapidly and at smaller diameters, consistent with the enhanced superaerophobicity observed in contact angle measurements.

To ensure statistical validity, more than 100 individual bubbles were analyzed from different substrate locations. The results, summarized in the histograms of **Figure 2.6**, demonstrate that the average detachment time (T_d) for bubbles on nanocone-modified electrodes was significantly shorter than that on pristine foil. Moreover, the detachment diameter (D_d) was consistently reduced, indicating that bubbles left the surface at an earlier growth stage. These findings corroborate the simulation results and highlight the role of nanocone geometry in diminishing adhesive forces at the bubble-electrode interface.

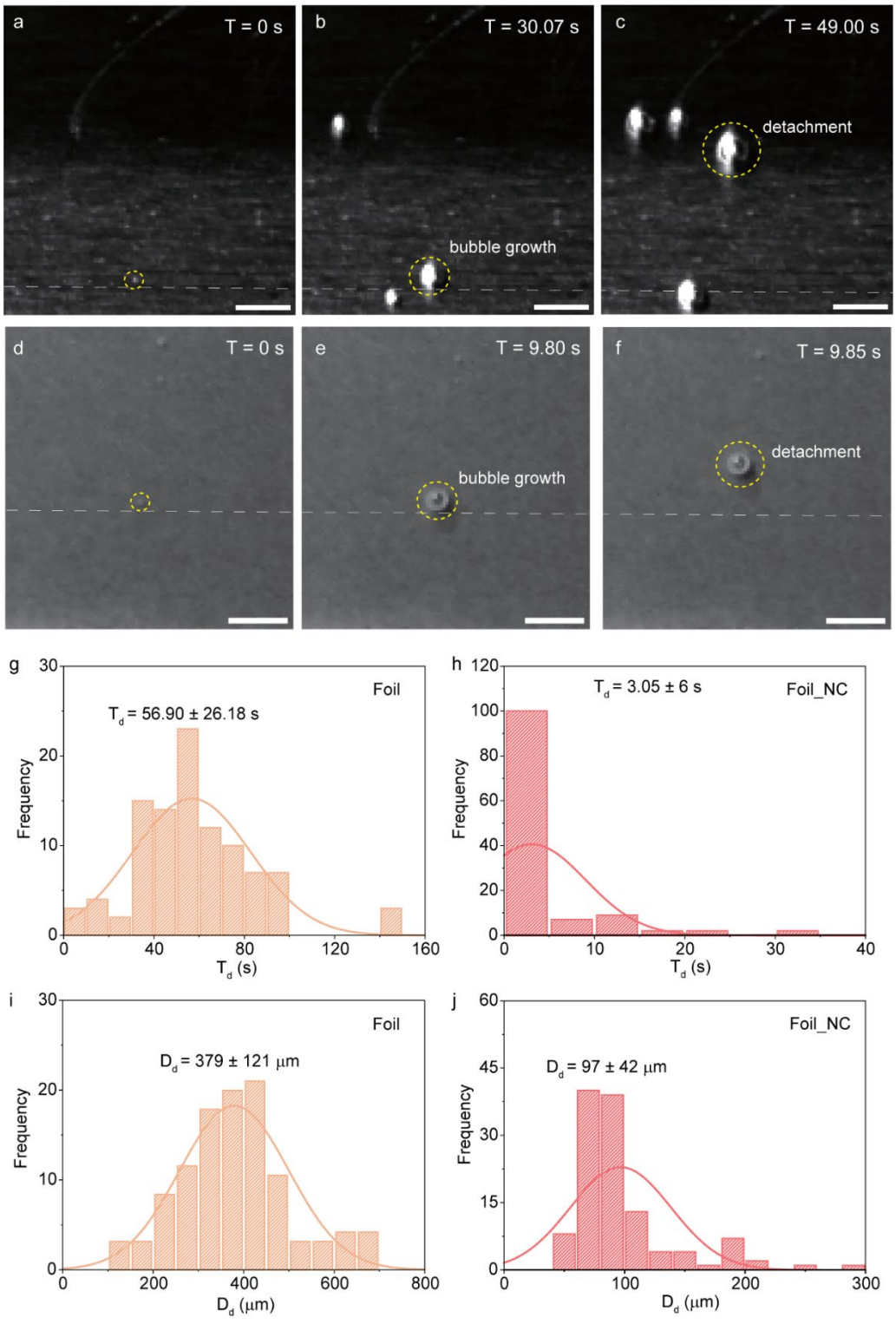

Figure 2.6. High-speed camera images showing hydrogen bubble evolution on (a-c) Foil and (d-f) Foil_NC as a function of time. Scale bars are 500 μm. The dashed circles highlight the bubble locations. Histograms illustrate the distribution of (g, h)

bubble detachment time (T_d) and (i, j) detachment size (D_d) on Foil and Foil_NC substrates.

Similar experiments were performed under OER conditions at 4 mA cm^{-2}. As shown in **Figure 2.7**, oxygen bubbles exhibited the same trend: faster detachment and smaller diameters on nanocone-modified surfaces compared to pristine electrodes. An additional phenomenon was observed on the unmodified foil, frequent bubble coalescence. Due to the longer residence time and larger size of bubbles, adjacent bubbles often merged to form even larger bubbles prior to detachment. This coalescence process not only delayed detachment further but also posed a greater risk of disturbing the electrode surface layer. In contrast, bubble coalescence was substantially suppressed on nanocone-modified electrodes, as bubbles detached quickly and maintained smaller sizes.

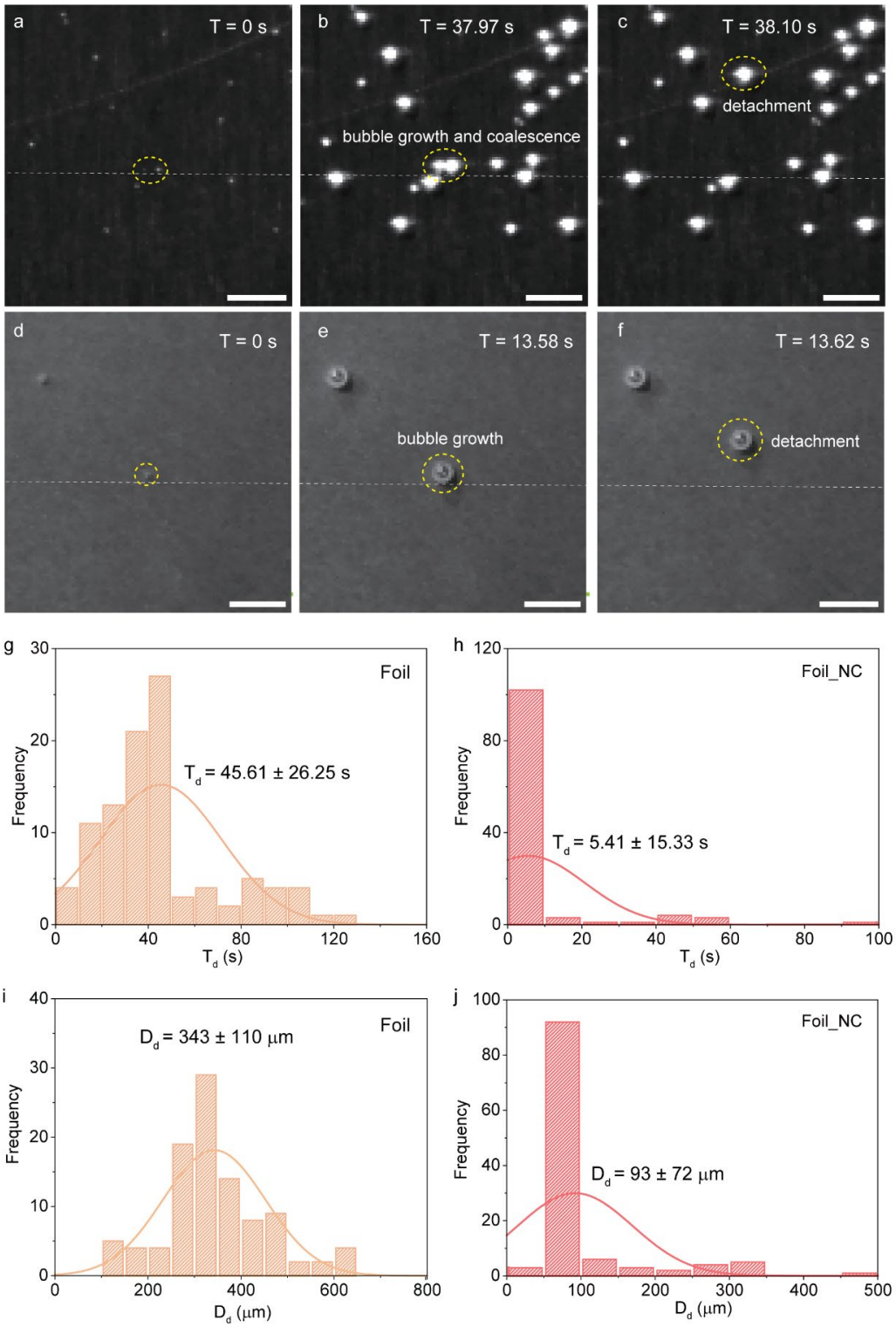

Figure 2.7. High-speed camera images show the oxygen bubble evolution process take place on (a-c) Foil and (d-f) Foil_NC, as a function of time. Scale bars are 500 μm. The dashed circles highlight the bubble locations. Histograms illustrate the

distribution of (g, h) bubble detachment time (T_d) and (i, j) detachment size (D_d) on Foil and Foil_NC substrates.

To further evaluate the electrode behavior under conditions more relevant to practical operation, bubble evolution was also examined at ultrahigh current densities of 1000 mA cm^{-2} (**Figure 2.8**). At this current density, massive gas production led to severe bubble accumulation on the pristine foil, where large bubbles adhered to the surface and hindered electrolyte access. In contrast, the nanocone-modified foil exhibited smooth bubble release, with fewer large bubbles observed and a more continuous evolution of gas. The stark contrast at high current densities underscores the importance of nanocone-induced superaerophobicity in maintaining electrode accessibility under industrially relevant conditions.

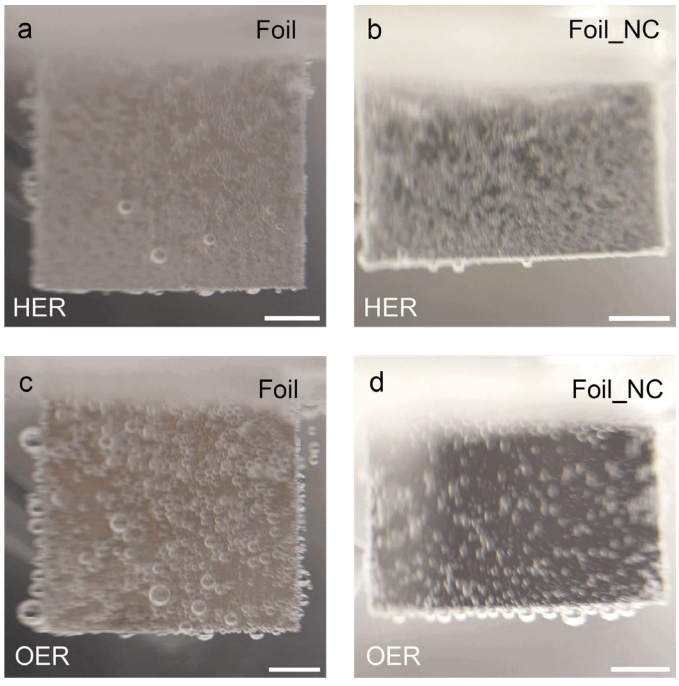

Figure 2.8. Gas bubble evolution at the high current density of 1000 mA cm^{-2}. Hydrogen bubble evolution on (a) Foil and (b) Foil_NC. Oxygen bubble evolution on (c) Foil and (d) Foil_NC. Scale bars are 2 mm.

2.4.4 Electrochemical performance at high current densities

To evaluate the effect of nanocone modification on electrochemical performance, the HER and OER activities of pristine Ni foil and nanocone-modified Ni foil (Foil_NC) were first compared in 1.0 M KOH. As shown in **Figure 2.9**, Foil_NC exhibited significantly improved electrochemical behavior for both HER and OER compared with pristine foil. For HER, Foil_NC reached a geometric current density of 1000 mA cm^{-2} at an overpotential of 519 mV, while pristine foil required 737 mV to achieve the same current density. This corresponds to a 29.5% reduction in overpotential. A similar improvement was observed for OER, where the overpotential at 1000 mA cm^{-2} decreased from 712 mV for pristine foil to 457 mV for Foil_NC, corresponding to a 35.8% reduction. These results show that nanocone modification substantially enhances the apparent electrochemical performance of Ni foil under high-current-density operation.

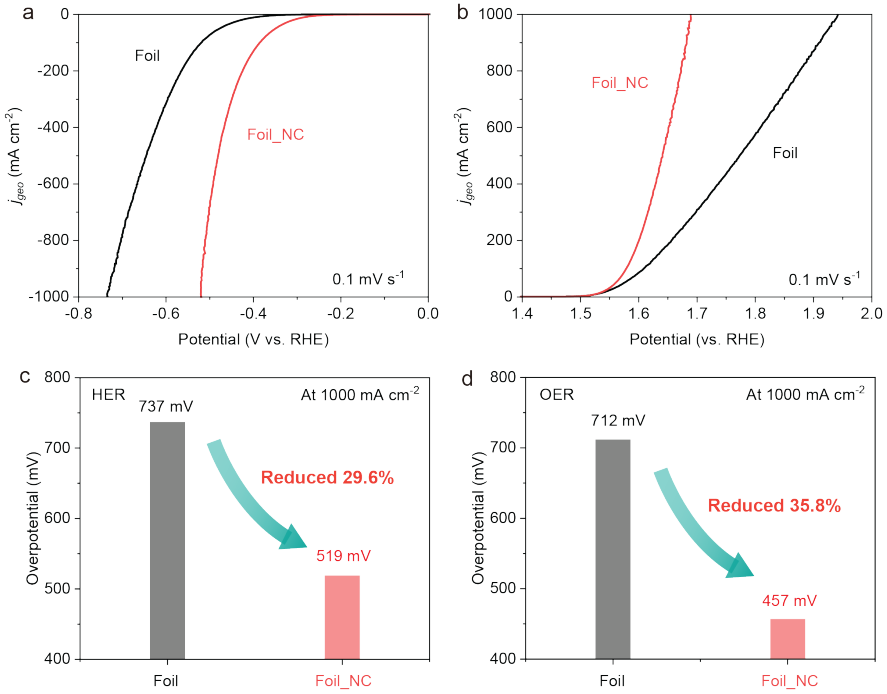

Figure 2.9. LSVs for (a) HER and (b) OER plotted based on geometric current density at a scan rate of 0.1 mV s^{-1}. Comparison of overpotentials required to reach 1000 mA cm^{-2} for (c) HER and (d) OER.

The geometric current density is determined by the intrinsic activity and the total amount of available catalytic active sites. We studied the electrochemically active surface area (ECSA) of both substrates. To estimate the ECSA, cyclic voltammetry measurements were performed at different scan rates in the non-faradaic potential regions for HER and OER. As shown in **Figure 2.10a** and **b**, Foil_NC exhibited a larger areal capacitance than pristine foil in the HER potential region, increasing from 0.12 to 0.44 mF cm^{-2}. Similarly, in the OER potential region, the areal capacitance increased from 0.30 to 0.81 mF cm^{-2} after nanocone modification (**Figure 2.10d, e**). These results are consistent with the roughened

surface morphology and dense nanocone coverage, which provide a larger electrochemically accessible area.

However, the performance enhancement cannot be explained solely by the increase in ECSA. After normalizing the current density by ECSA, Foil_NC still showed higher HER and OER activity than pristine foil (**Figure 2.10c, f**). This result indicates that the nanocone structure does more than simply increase the number of accessible surface sites. Instead, the nanocone-modified surface also improves the effective reaction environment during gas-evolving reactions. At high current densities, rapid gas bubble generation can block active sites, reduce electrolyte contact, and increase local transport resistance. The nanocone structure facilitates bubble removal from the electrode surface, thereby maintaining more efficient electrode-electrolyte contact during HER and OER. Therefore, the improved electrochemical performance of Foil_NC arises from the combined effects of increased active surface area and enhanced bubble detachment behavior, with the latter becoming particularly important under high-rate water splitting conditions.

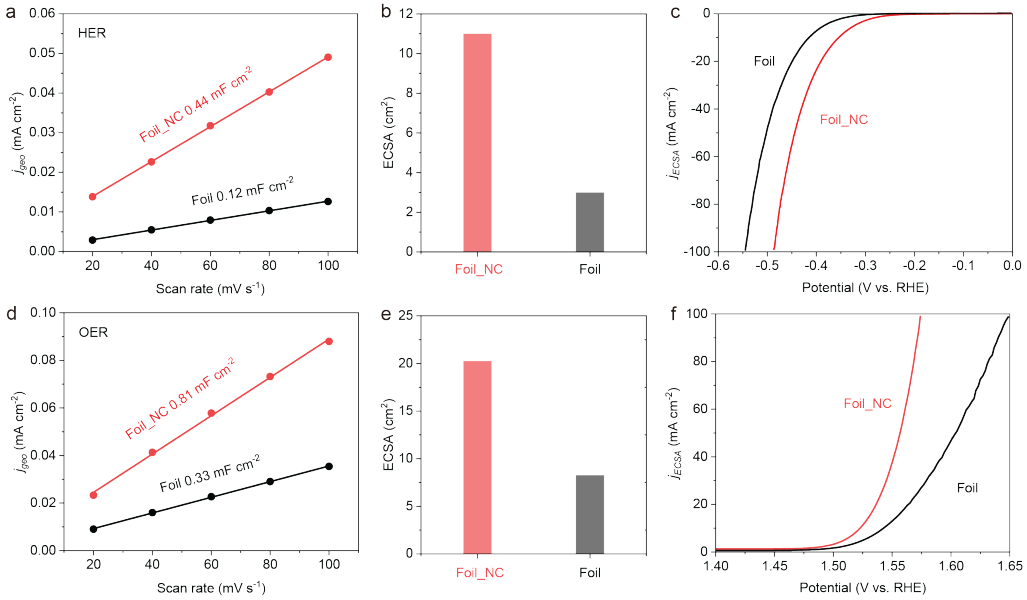

Figure 2.10. ECSA analysis and ECSA-normalized electrochemical performance of pristine Ni foil and Foil_NC. Capacitive current density plotted as a function of scan rate in the non-faradaic regions for (a) HER and (d) OER, respectively. (b and e) Comparison of ECSA values calculated from the scan-rate-dependent current response. ECSA-normalized polarization curves for (c) HER and (f) OER in 1.0 M KOH.

To evaluate the generality of this approach, we extended the study to nickel foam, a commonly used 3D porous substrate with large surface area for alkaline water splitting. As shown in **Figure 2.11**, Foam_NC exhibited a significantly larger ECSA compared to pristine foam. The increase is attributed to the conformal growth of nanocones across the three-dimensional porous framework, which effectively increases the roughness and exposes additional active surface sites throughout the foam structure. This enhancement demonstrates that the nanocone modification strategy is not limited to flat electrodes but can also be extended to 3D porous architectures, where the enlarged surface area is particularly beneficial for supporting high current operation.

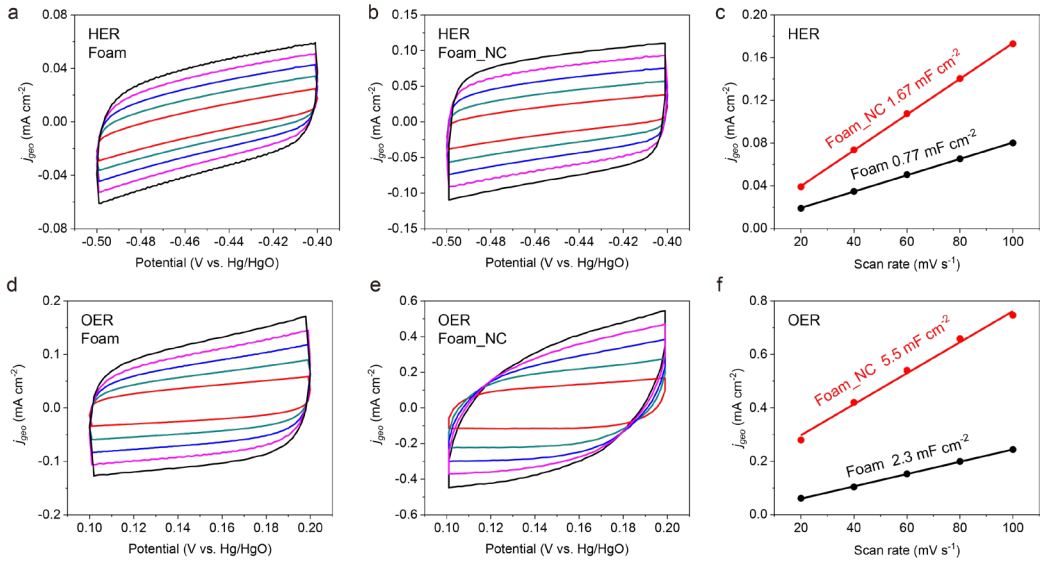

Figure 2.11. CV curves of Foam and Foam_NC collected for (a, b) HER and (d, e) OER in 1.0 M KOH at different scan rates from 20 to 100 mV s^{-1} with an interval of 20 mV s^{-1}. The difference of geometric current density j_{geo} of Foam and Foam_NC are plotted as a function of scan rate for (c) HER and (f) OER, respectively.

We then compared the HER and OER polarization curves of Foam and Foam_NC electrodes. As shown in **Figure 2.12**, the nanocone-modified foam exhibited markedly reduced overpotentials relative to pristine foam across the entire potential range. For example, at a geometric current density of 1000 mA cm^{-2}, Foam_NC required substantially lower applied potentials (-0.491 V vs. RHE for HER and 1.638 V vs. RHE for OER, respectively) than the unmodified substrate (-0.785 V vs. RHE for HER and 2.052 V vs. RHE for OER), highlighting the beneficial effect of nanocone modification on three-dimensional porous electrodes. Importantly, when the current densities were normalized to ECSA, Foam_NC still outperformed pristine foam. This result indicates that the performance enhancement

arises from the accelerated bubble detachment provided by the nanocone structures, which plays a central role in sustaining mass transport and catalytic activity under high-rate water splitting conditions.

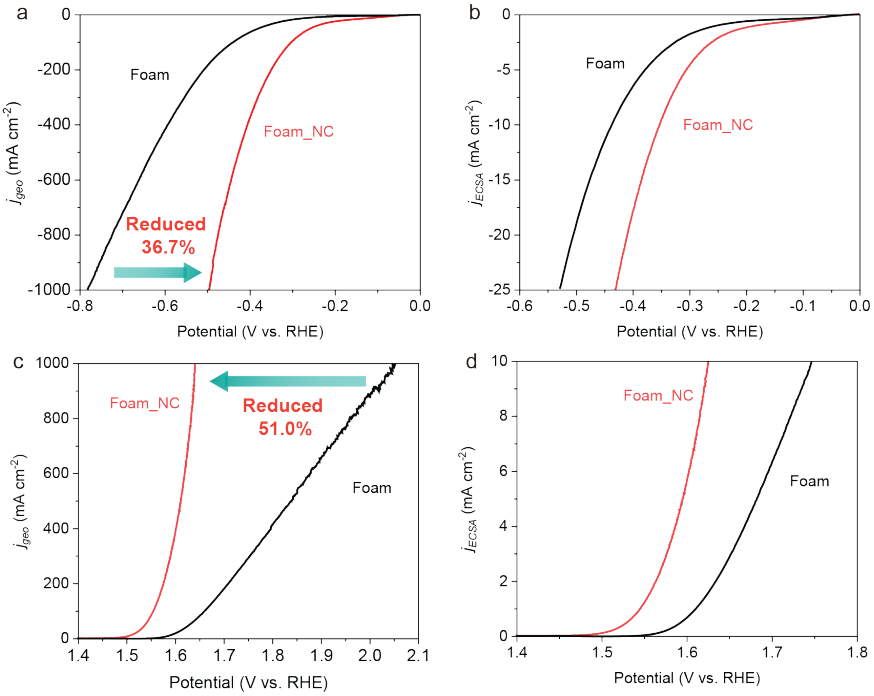

Figure 2.12. LSVs of Foam and Foam_NC electrodes collected in 1.0 M KOH at a scan rate of 0.1 mV s^{-1} for (a, b) HER and (c, d) OER. Figures (a and c) are plotted in geometric current density, while Figures (b and d) are plotted in ECSA-normalized current density.

2.4.5 Extension to 3D architectures

Previous work from our group demonstrated under ultrahigh current densities that, compared to conventional nickel foam with tortuous and disordered pore networks, 3D-printed nickel lattice electrodes with ordered channels provide significant advantages for bubble management. The periodic and low-tortuosity architecture facilitates more efficient bubble transport, thereby minimizing bubble

coalescence and accumulation within the electrode interior.[26] Motivated by these findings, we selected 3D-printed lattice electrodes as a representative porous architecture to further investigate the effects of nanocone surface modification.

To assess the generality of this surface engineering strategy, the same electrodeposition method was applied to both nickel foam and 3D-printed nickel lattices. SEM and XRD analyses confirmed that in both cases the substrates were uniformly covered with dense nickel nanocone structures (**Figures 2.1** and **2.2**). Although slight variations in cone size were observed due to differences in local growth environments, the overall morphology was consistent with that obtained on flat nickel foils, demonstrating that nanocone growth can be successfully extended from planar electrodes to three-dimensional porous architectures.

The ECSA of the 3D-printed nickel lattice before and after nanocone modification was also examined. As shown in **Figure 2.13**, the Lattice_NC electrode exhibited a substantially larger ECSA compared to the pristine lattice. This enhancement arises from the uniform deposition of nanocones along the ordered struts of the lattice architecture, which significantly increases the surface roughness and exposes a greater number of electrochemically accessible active sites.

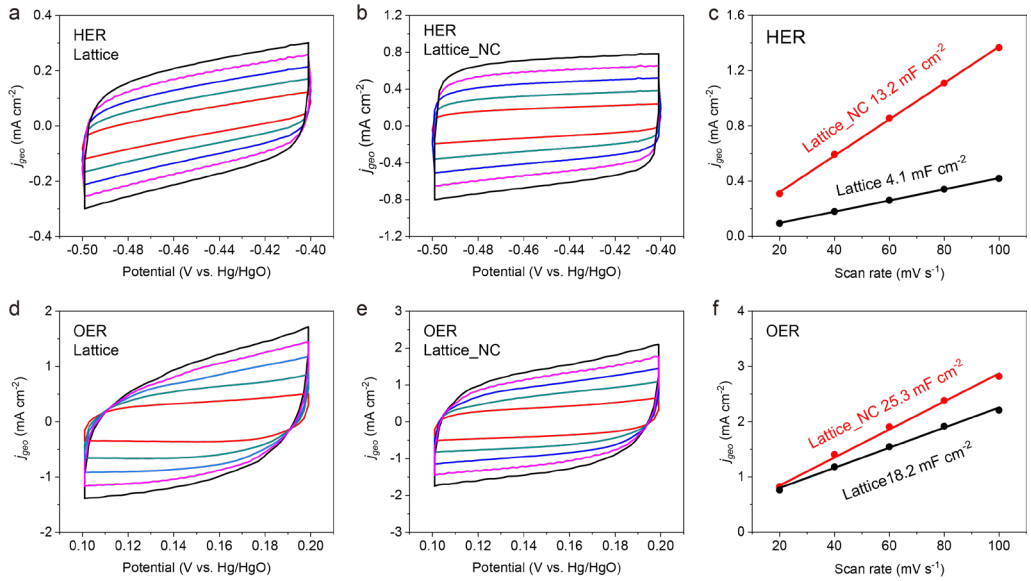

Figure 2.13. CV curves of the Lattice and Lattice_NC for (a-b) HER and (d-e) for OER were collected in 1.0 M KOH at different scan rates from 20 to 100 mV s^{-1} at an interval of 20 mV s^{-1}. The difference of geometric current density j_{geo} of Lattice and Lattice_NC are plotted as a function of scan rate for (c) HER and (f) OER, respectively.

Electrochemical testing demonstrated that nanocone modification also improved the performance of 3D-printed nickel lattice electrodes. As shown in **Figure 2.14**, Lattice_NC exhibited substantially higher current densities for both HER and OER compared to the pristine lattice. At a geometric current density of 1000 mA cm^{-2}, Lattice_NC required lower potentials than the pristine lattice for both HER (-0.417 vs. -0.686 V vs. RHE) and OER (1.607 vs. 1.897 V vs. RHE). confirming the beneficial role of nanocone structures in enhancing catalytic activity. Importantly, when the current densities were normalized by ECSA, Lattice_NC still outperformed the pristine lattice, indicating that the improvement cannot be explained solely by increased surface area. Instead, the rapid detachment of bubbles

facilitated by the nanocone structures plays a central role in sustaining electrolyte contact and achieving superior performance at high current densities.

To further compare the effect of nanocone modification across different substrates, we analyzed the overpotentials required to reach 1000 mA cm^{-2} for Foil_NC, Foam_NC, and Lattice_NC electrodes under both HER and OER conditions (**Figure 2.14e** and **2.14f**). Among the three, Lattice_NC consistently required the lowest overpotentials. This superior performance is closely related to the ordered, low-tortuosity channels inherent to the 3D-printed lattice, which promotes efficient bubble transport and prevents bubble accumulation within the electrode framework. The combination of nanocone-induced superaerophobicity with the favorable architecture of the 3D-printed lattice thus provides a powerful strategy for achieving efficient and stable operation under ultrahigh current densities.

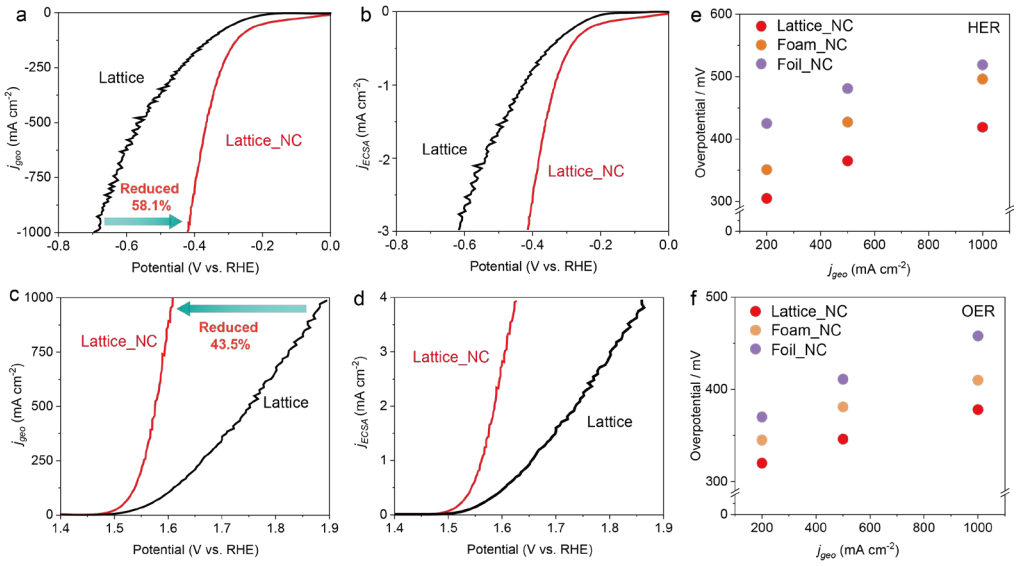

Figure 2.14. LSVs of Lattice and Lattice_NC electrodes collected in 1.0 M KOH at a scan rate of 0.1 mV s^{-1} for (a, b) HER and (c, d) OER. Figures (a and c) are plotted in geometric current density, while Figures (b and d) are plotted in ECSA-

normalized current density. Figures (e and f) compare the HER and OER overpotentials of Foil_NC, Foam_NC, and Lattice_NC at different geometric current densities.

To further understand the origin of the improved electrochemical performance, electrochemical impedance spectroscopy (EIS) was performed for the Ni foil-, Ni foam-, and 3D printed lattice-based electrodes under both HER and OER conditions. As shown in **Figure 2.15**, all nanocone-modified electrodes exhibited smaller semicircles than their corresponding unmodified electrodes, indicating reduced charge-transfer resistance after nanocone modification. This trend was observed consistently for Foil_NC, Foam_NC, and Lattice_NC, confirming that the nanocone structure improves the interfacial reaction environment across different electrode geometries.

Among these electrodes, Lattice_NC showed the smallest impedance response. This result is consistent with its superior polarization performance and suggests that combining a 3D printed open lattice architecture with nanocone surface modification provides the most favorable electrode configuration. The lattice structure offers an open pathway for electrolyte transport and gas release, while the nanocone surface promotes rapid bubble detachment from the electrode surface. Together, these two structural features help maintain efficient electrolyte contact, reduce bubble-induced blockage, and facilitate interfacial charge transfer during high-rate water splitting.

Therefore, the EIS results further support that the enhanced activity of nanocone-modified electrodes is not only associated with increased surface area,

but also with improved gas management and reduced interfacial resistance. This effect becomes particularly important at high current densities, where rapid gas products generation can otherwise block active sites and increase local transport resistance.

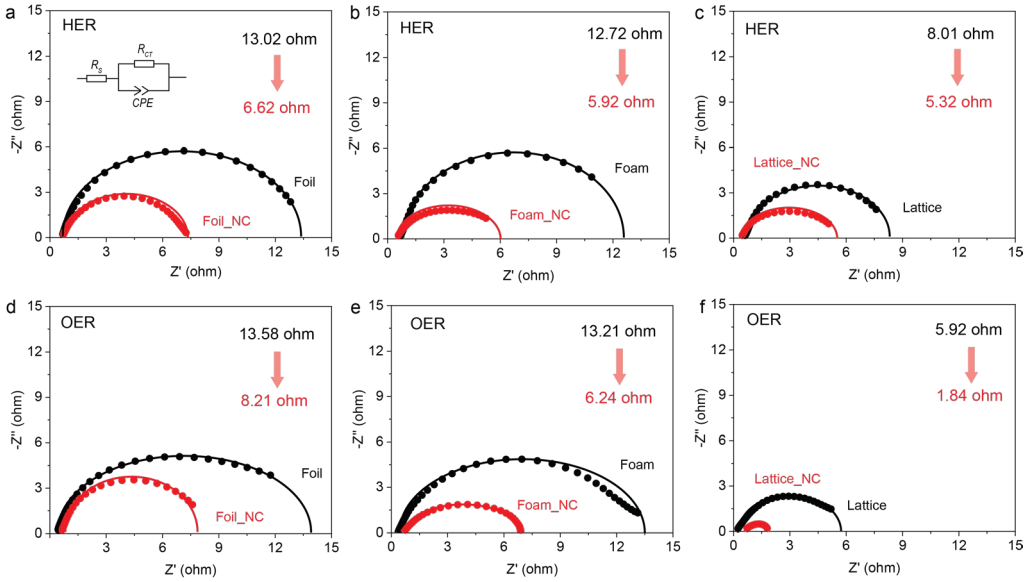

Figure 2.15. EIS spectra of (a, d) Foil and Foil_NC, (b, e) Foam and Foam_NC, and (c, f) Lattice and Lattice_NC were collected in 1.0 M KOH. The top row shows EIS spectra under HER conditions, and the bottom row shows EIS spectra under OER conditions. EIS was performed at -1.08 V versus Hg/HgO for HER and 0.70 V versus Hg/HgO for OER, with a frequency ranging from 100 kHz to 1 Hz and an amplitude of 5 mV. Circles represent experimental data. The solid lines represent fitting curves based on the equivalent circuit model (inset).

2.4.6 Long-term stability and surface integrity

In addition to high activity, practical electrolyzer electrodes must also demonstrate long-term durability under industrially relevant conditions. To evaluate the stability of nanocone-modified electrodes, a two-electrode alkaline water

splitting device was assembled using Lattice_NC electrodes as both the anode and cathode. The cell was operated at a fixed voltage of 2.45 V in 1.0 M KOH at room temperature, corresponding to an initial current density of approximately 910 mA cm^{-2}.

As shown in **Figure 2.16**, the device maintained over 95% of its initial current after 100 h of continuous operation, highlighting the exceptional electrochemical stability of the Lattice-NC architecture. This level of durability at nearly 1 A cm-2 is significant, as bubble-induced mechanical stress and detachment forces are generally expected to compromise electrode coatings under such demanding conditions.

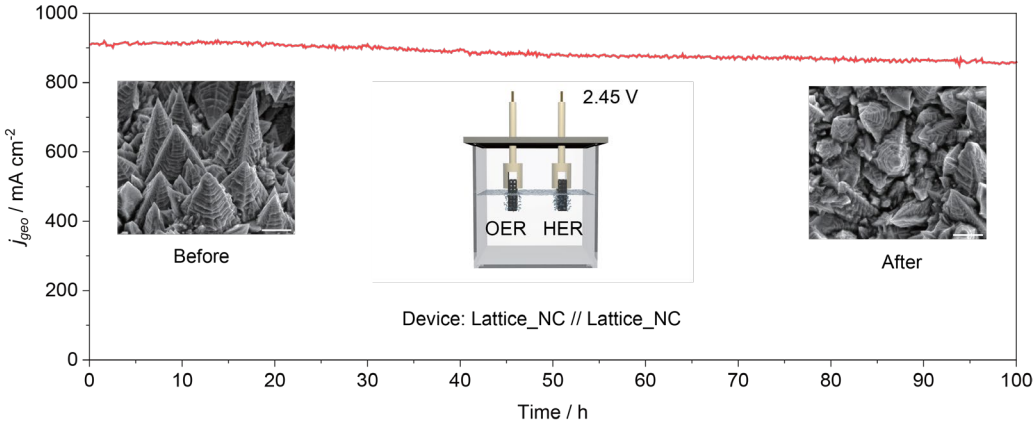

Figure 2.16. The geometric current density of a device assembled with two Lattice_NC electrodes recorded at a fixed voltage of 2.45 V for 100 h. The inset figure shows a schematic illustration of the two-electrode device. The SEM images show the NC morphology before and after the stability test.

Post-stability analysis further confirmed the structural robustness of the nanocone layer. SEM images collected after the stability test revealed that the nanocone morphology was largely preserved, with no significant peeling,

delamination, or structural collapse observed (**Figure 2.17**). This suggests that the nanocone features were mechanically resilient against repeated bubble detachment and fluid shear stresses. XPS analysis provided additional insights into chemical stability. For electrodes tested under HER conditions, the Ni 2p spectra before and after stability tests showed consistent signals from metallic Ni, Ni^{2+}, and Ni^{3+}, indicating minimal surface oxidation. In contrast, electrodes subjected to OER conditions exhibited a diminished metallic Ni signal after long-term operation, with Ni^{2+} and Ni^{3+} species dominating the spectra (**Figure 2.17**). This transformation is attributed to the oxidative environment of OER, where surface Ni tends to form stable hydroxide or oxyhydroxide phases. Despite this chemical shift, the overall catalytic performance remained stable, suggesting that the nanocone-modified architecture provides sufficient tolerance to oxidative restructuring.

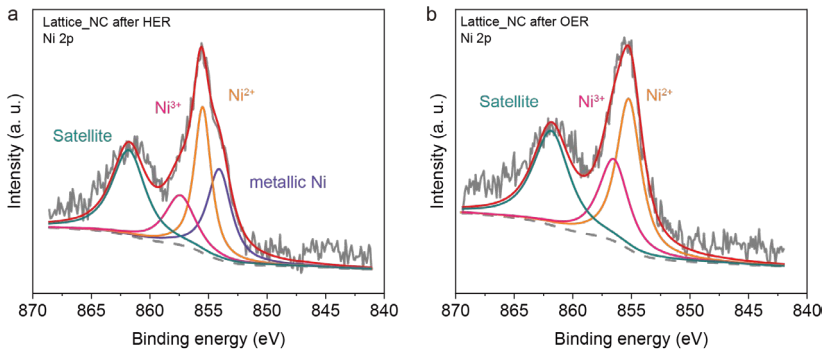

Figure 2.17. Ni 2p XPS spectra of (a) Lattice_NC after HER and (b) Lattice_NC after OER stability tests in water splitting.

Overall, these results confirm that nanocone surface modification not only enhances bubble detachment and catalytic performance but also demonstrates strong mechanical and electrochemical stability under ultrahigh current densities. The preservation of both structural integrity and catalytic activity underscores the

potential of nanocone-modified electrodes for long-term operation in practical water electrolyzer systems.

2.5 Conclusion

In this chapter, nanocone surface modification was demonstrated as an effective strategy to address one of the most critical challenges in high-rate alkaline water splitting: the accumulation and slow detachment of gas bubbles at the electrode-electrolyte interface. Through a combination of simulations, high-speed optical imaging, electrochemical measurements, and long-term stability tests, the mechanistic origins of this improvement were established.

The results show that nanocone-modified nickel surfaces exhibit superaerophobicity, which facilitates rapid bubble detachment and suppresses bubble coalescence. Compared to pristine electrodes, the modified surfaces supported significantly smaller bubble detachment sizes and shorter residence times. Electrochemically, these improvements translated into reduced overpotentials at ultrahigh current densities ($\approx$1000 mA cm^{-2}) and enhanced device stability over extended operation. Importantly, the beneficial effects were not limited to nickel foils but were also observed on nickel foam and 3D-printed nickel lattices, demonstrating the generality and scalability of this surface engineering approach.

Mechanistically, the improved performance arises not from altered catalytic chemistry but from engineered interfacial geometry. The nanocone structures both reduce the effective contact area between bubbles and the substrate and reorient adhesive forces, thereby lowering the barrier for bubble detachment. By mitigating bubble-induced blockage, the electrodes retain more accessible catalytic sites and sustain efficient ion transport under demanding conditions.

This study establishes that surface nanostructuring offers a robust and energy-efficient solution for bubble management in practical alkaline electrolyzers. Nevertheless, while the nanocone strategy effectively addresses gas bubble accumulation, another key limitation in high-current-density operation is ion diffusion through the electrolyte and electrode pores. The next chapter therefore focuses on strategies to alleviate ion transport resistance, further advancing the development of stable and efficient electrodes for large-scale hydrogen production.

References

1. Kou, T.; Wang, S.; Li, Y. *ACS Mater. Lett.* **2021**, 3, 224
2. Wang, W.; Xu, X.; Zhou, W.; Shao, Z., *Adv. Sci. (Weinh)* **2017**, 4, 1600371;
3. Tang, C.; Zheng, Y.; Jaroniec, M.; Qiao, S. Z., *Angew. Chem. Int. Ed. Engl.* **2021**, 60, 19572;
4. Sun, H.; Yan, Z.; Liu, F.; Xu, W.; Cheng, F.; Chen, J., *Adv Mater* **2020**, 32, e1806326;
5. Carmo, M.; Fritz, D. L.; Mergel, J.; Stolten, D., *Int. J. Hydrogen Energy* **2013**, 38, 4901.
6. Yu, Z. Y.; Duan, Y.; Feng, X. Y.; Yu, X.; Gao, M. R.; Yu, S. H., *Adv. Mater.* **2021**, 33, 2007100.
7. Luo, Y.; Zhang, Z.; Chhowalla, M.; Liu, B., *Adv. Mater.* **2022**, 34, 2108133;
8. Zhang, C.; Luo, Y.; Tan, J.; Yu, Q.; Yang, F.; Zhang, Z.; Yang, L.; Cheng, H. M.; Liu, B., *Nat. Commun.* **2020**, 11, 3724.
9. Angulo, A.; van der Linde, P.; Gardeniers, H.; Modestino, M.; Fernández Rivas, D., *Joule* **2020**, 4, 555;

10. Wang, J.; Xu, F.; Jin, H.; Chen, Y.; Wang, Y., *Adv. Mater.* **2017**, 29, 1605838.
11. Buttler, A.; Spliethoff, H., *Renewable Sustainable Energy Rev.* **2018**, 82, 2440.
12. Niether, C.; Faure, S.; Bordet, A.; Deseure, J.; Chatenet, M.; Carrey, J.; Chaudret, B.; Rouet, A., *Nat. Energy* **2018**, 3, 476;
13. Islam, M. H.; Burheim, O. S.; Pollet, B. G., *Ultrason. Sonochem.* **2019**, 51, 533;
14. Fernández, D.; Diao, Z.; Dunne, P.; Coey, J. M. D., *Electrochim. Acta* **2010**, 55, 8664.
15. Xie, L.; Wang, L.; Zhao, W.; Liu, S.; Huang, W.; Zhao, Q., *Nat. Commun.* **2021**, 12, 5070;
16. Lu, Z.; Zhu, W.; Yu, X.; Zhang, H.; Li, Y.; Sun, X.; Wang, X.; Wang, H.; Wang, J.; Luo, J.; Lei, X.; Jiang, L., *Adv. Mater.* **2014**, 26, 2683.
17. Bae, M.; Kang, Y.; Lee, D. W.; Jeon, D.; Ryu, J., *Adv. Energy Mater.* **2022**, 12, 2201452.
18. Hodges, A.; Hoang, A. L.; Tsekouras, G.; Wagner, K.; Lee, C. Y.; Swiegers, G. F.; Wallace, G. G., *Nat. Commun.* **2022**, 13, 1304.
19. Su, Z.; Yang, C.; Xie, B.; Lin, Z.; Zhang, Z.; Liu, J.; Li, B.; Kang, F.; Wong, C. P., *Energy Environ. Sci.* **2014**, 7, 2652.
20. Latt, J.; Malaspinas, O.; Kontaxakis, D.; Parmigiani, A.; Lagrava, D.; Brogi, F.; Belgacem, M. B.; Thorimbert, Y.; Leclaire, S.; Li, S.; Marson, F.; Lemus, J.; Kotsalos, C.; Conradin, R.; Coreixas, C.; Petkantchin, R.; Raynaud, F.; Beny, J.; Chopard, B., *Comput. Math. with Appl.* **2021**, 81, 334.
21. Santos, J. E.; Bihani, A.; Landry, C. J., Git code **2019**, https://doi.org/10.5281/zenodo.5203295.

22. Feng, L. L.; Yu, G.; Wu, Y.; Li, G. D.; Li, H.; Sun, Y.; Asefa, T.; Chen, W.; Zou, X., *J. Am. Chem. Soc.* **2015**, 137, 14023.

23. Kou, T.; Wang, S.; Hauser, J. L.; Chen, M.; Oliver, S. R. J.; Ye, Y.; Guo, J.; Li, Y., *ACS Energy Lett.* **2019**, 4, 622.

24. Lv, J.; Yang, Q.; Liang, T.; Sun, X.; Rong, W.; Dai, Q.; Liu, Y., *J. Am. Chem. Soc.,* **2025**, 147, 27708.

25. George, J. E.; Chidangil, S.; George, S. D., *Adv. Mater. Interfaces* **2017**, 4, 1601088.

26. Kou, T.; Wang, S.; Shi, R.; Zhang, T.; Chiovoloni, S.; Lu, J. Q.; Chen, W.; Worsley, M. A.; Wood, B. C.; Baker, S. E.; Duoss, E. B.; Wu, R.; Zhu, C.; Li, Y., *Adv. Energy Mater.* **2020**, 10, 2002955

Chapter 3

Interpenetrating 3D Electrodes for High-Rate Alkaline Water Splitting

3.1 Abstract

High-rate alkaline water splitting remains limited by ion-transport losses once gas-bubble blockage is mitigated. To address this, we designed and validated a 3D-printed interpenetrating gyroid (3DIG) electrode in which two independent, interwoven lattices minimize interelectrode distance and provide ordered, and open channels for ion diffusion and gas removal. Simulation results show that the 3DIG architecture establishes a more uniform electric-potential gradient and achieves cell-wide concentration equilibration more rapidly than a configuration using separate 3D-printed gyroid electrodes (3DG), indicating accelerated ionic diffusion and improved spatial utilization. Experimentally, 3DIG delivers markedly higher current density at a fixed voltage (e.g., ~1000 mA cm^{-2} at 2.85 V for 3DIG versus ~225 mA cm^{-2} for 3DG), despite comparable ECSA, and exhibits consistently lower solution resistance (R_S) and charge-transfer resistance (R_{CT}) based on the electrochemical impedance spectra analysis. The advantage of the interpenetrating design is amplified at lower temperatures, where sluggish diffusion typically dominates, yet 3DIG still maintains small R_S and R_{CT} values (e.g., ~1.0 Ω and ~3.5 Ω at 275 K). Further surface engineering and catalyst modification (nanocone modification and NiFeOOH coating) reduce the overpotential without sacrificing the ordered transport pathways. These results demonstrate that interpenetrating gyroid electrodes provide a device-level route to alleviate ion-diffusion limitations in alkaline water splitting and complement the bubble-detachment strategy established in Chapter 2.

3.2 Introduction

Alkaline water splitting is one of the most promising technologies for clean hydrogen production.[1-3] To achieve high efficiency, substantial efforts have been devoted to minimizing the activation overpotential by improving the intrinsic catalytic activity and increasing the number of accessible active sites.[4,5] However, because alkaline water splitting involves two gas-evolution reactions occurring at the gas-liquid-solid triple-phase boundary, its performance is also significantly influenced by extrinsic transport limitations, particularly under high-current densities.[6-8]

As current density increases, the accumulation of hydrogen and oxygen gas bubbles can block active sites, thereby increasing the activation overpotential. In addition, these bubbles impede ion transport and electrolyte access, contributing to additional ohmic loss.[9] With advances in additive manufacturing, various three-dimensional (3D) architected electrodes have been developed to increase surface area and facilitate bubble detachment.[10-12] Nevertheless, simply stacking 3D electrodes in parallel does not represent an optimal device-level configuration.

Mass transport, particularly ionic diffusion resistance during alkaline water splitting, remains an important yet often overlooked factor. The efficiency of ion diffusion depends on both the concentration gradient and the inter-electrode distance. Thick electrodes and retained gas bubbles increase effective diffusion pathways, resulting in inhomogeneous concentration gradients and larger mass-transport overpotential. Existing strategies mainly focus on improving electrolyte conductivity through additives.[13, 14] Alternatively, reducing the electrode separation

distance through rational arrangement of 3D electrodes provides a more direct and practical route to enhancing ion diffusion at the device level.

Here, we present an interpenetrating gyroid electrode architecture consisting of two independent lattices interwoven within the same volume for alkaline water splitting. This configuration enables the integration of porous anode and cathode structures while maintaining a constant and minimized separation distance, independent of electrode thickness. The open architecture of each lattice ensures efficient bubble release within this compact configuration.[15] Using double-gyroid interpenetrating nickel lattices as a model system, we demonstrate that the interpenetrating gyroid (3DIG) architecture significantly improves ion transport compared with separate gyroid electrodes (3DG). The 3DIG device exhibits reduced solution resistance (R_S) and charge-transfer resistance (R_{CT}), and achieves substantially higher current densities under the same applied voltage. For example, at 2.85 V, 3DIG delivers a current density of 1000 mA cm^{-2}, which is significantly higher than that of 3DG (225 mA cm^{-2}), highlighting the effectiveness of the interpenetrating design in mitigating ion-diffusion limitations. Finally, we explore surface modification strategies, such as nanocone engineering and NiFeOOH coating, that further improve catalytic activity without compromising ordered transport pathways.

This work establishes interpenetrating gyroid electrodes as a generalizable platform for engineering ion transport in alkaline electrolyzers, providing a complementary strategy to the bubble-management advances discussed in Chapter 2 and offering a pathway toward practical high-rate hydrogen production.

3.3 Experimental section

3.3.1 Fabrication of 3D-printed interpenetrating gyroid electrodes

Interpenetrating and separate double gyroid (3DIG and 3DG) electrodes were fabricated using a commercial photo-curable plant-based resin (Elegoo) using a stereolithography 3D printer (Saturn 8K, Elegoo). The gyroid structures were generated in Rhinoceros 3D, a commercial computer-aided design software package, and exported for printing. All printed parts were rinsed and sonicated in isopropyl alcohol for approximately 5 min to remove residual resin, followed by post-curing for 1 h at 60 °C under 405 nm UV light (Form Cure, Formlabs).

Printing was conducted with a layer thickness of 50 μm. The exposure duration was set to 35 s for the first layer to ensure adhesion and 5 s for each subsequent layer. The platform retraction velocity was maintained at 80 mm min^{-1}. To enhance surface wettability, the printed gyroid lattices were plasma-treated in an air plasma cleaner (Harrick Plasma) for 2 min at a radio-frequency power of 18 W.

The physical dimensions of the interpenetrating gyroid electrodes with different unit cell lengths are summarized in **Table 3.1.**

Table 3.1. Physical dimensions of interpenetrating electrodes with different unit cell lengths.

Unit cell length / mm	Dimension (length × width × thickness) / mm
4	15 × 12 × 3.5
6	18 × 18 × 5.5
8	17 × 17 × 8.0

3.3.2 Metallization of 3DIG and 3DG

Although the 3D-printed gyroid scaffolds provided the desired interpenetrating geometry, the as-printed polymer frameworks exhibited inherently limited electrical conductivity. To convert these structures into continuous conductive electrodes, a two-step metallization procedure was employed, consisting of sensitization/activation followed by electroless nickel plating and subsequent Ni electrodeposition.[16]

Prior to metallization, the printed gyroid substrates were immersed in 3.0 M NaOH at 45 °C for 30 min to clean the surface and generate hydroxyl groups that promote adhesion. The substrates were then sensitized in an aqueous solution containing 6.0 g of $SnCl_2$ and 6.0 mL of concentrated HCl, followed by activation in a solution containing 60 mg of $PdCl_2$ and 1.5 mL of HCl at 45 °C for 60 min. This process introduced catalytic Pd nuclei across the scaffold surface, enabling uniform nucleation during subsequent electroless plating.

Electroless nickel plating was carried out in a 300 mL bath containing 3.9 g $NiSO_4$, 6.3 g citric acid, and 3.18 g NaH_2PO_2 as the reducing agent. The solution was maintained at 70 °C, and the substrates were immersed for 10 min to deposit a conformal nickel layer across the entire 3D structure. The plating reaction proceeded through the autocatalytic reduction of Ni^{2+} onto the Pd-seeded surface, forming a uniform metallic film across the scaffold surface.

To further thicken the conductive backbone and ensure robust electrical conductivity, electrodeposition of nickel was subsequently performed using a standard three-electrode setup with the gyroid scaffold as the working electrode, Ni foam as the counter electrode, and Ag/AgCl as the reference electrode. The

electrolyte contained 0.84 M $NiCl_2$, 1.0 M H_3BO_3, and 1.40 M NH_4Cl (pH = 4.0). Electrodeposition was performed at a constant current density of 20 mA cm^{-2} for 8 min at 60 °C. This procedure yielded an additional nickel layer that reinforced the scaffold mechanically and electrically while preserving the interpenetrating architecture.

The resulting metallized 3DIG and 3DG electrodes displayed continuous electrical pathways throughout the scaffold, high structural integrity, and uniform surface coverage. These characteristics enabled reliable electrochemical testing under ultrahigh current densities without collapse or localized ohmic losses.

3.3.3 Synthesis of NiFeOOH@3DIG

NiFeOOH catalyst was deposited onto 3DIG using a previously reported method.[17] Nanocone-modified 3DIG was immersed in a solution containing 0.814 mmol iron chloride hexahydrate in 60 mL of ethanol. The samples were then immersed in a solution containing 0.814 mmol iron chloride hexahydrate and 4.49 mmol ammonium bicarbonate in 60 ml of ethanol while stirring for 6 h at room temperature to obtain NiFeOOH@3DIG. The sample was removed, washed with DI water, and dried under ambient conditions.

3.3.4 Electrode fabrication

Conductive silver colloidal paint was used to attach a piece of Ni foil strip onto each of the two strands of 3DIG or 3DG, so the two electrodes could be individually addressed. Then, epoxy was used to cover the stands and the rest of the electrode, ensuring that only the central gyroid structure was exposed for the water splitting reaction.

3.3.5 Structural and surface characterization

The morphology of the printed and metallized 3DIG scaffolds was characterized by scanning electron microscopy (SEM, Hitachi S-4800 II). Crystal structures were analyzed by X-ray diffraction (XRD, Rigaku SmartLab) using Cu Kα radiation, with standard nickel diffraction peaks provided for reference. Elemental analysis was collected by an SEM equipped with Thermo Fisher Apreo, Oxford Ultimax EDS, Aztec 5.1.

3.3.6 Electrochemical measurements

Electrochemical measurements of 3DIG and 3DG were performed using a CHI 660D electrochemical workstation in a two-electrode configuration in a 1.0 M KOH solution. For each sample, cyclic voltammetry (CV) was first performed within a cell-voltage window of 0.6 to 3.0 V for 40 cycles at a scan rate of 10 mV s^{-1}, and then LSVs were collected at 1.0 mV s^{-1}. EIS measurements were performed at cell voltages corresponding to different current densities (10, 50, 100, and 200 mA cm^{-2}), derived from the LSVs, utilizing a frequency range from 100 kHz to 1 Hz, and an amplitude of 5 mV. The R_S and the R_{CT} were obtained from the Nyquist plots. The water splitting stability test was performed at room temperature in a two-electrode configuration at various voltages. ECSA was determined by measuring the capacitive current associated with double-layer charging from the scan-rate dependence of CVs. LSV and EIS data were collected at various temperatures by placing the electrocatalytic cell in a thermally controlled water bath.

The ECSA values of 3DIG and 3DG were determined using a previously reported method.[18] Specifically, a series of CV curves were collected within a potential window ranging from 0.1 to 0.2 V where no faradaic reaction occurred.

The scan rate varied between 2 and 10 mV s^{-1} at an interval of 2.0 mV s^{-1}. A linear plot was generated from the difference between j_{anodic} and $j_{cathodic}$ (at 0.15 V) versus scan rate, and the slope of this plot represents the electrode's areal capacitance and is proportional to its ECSA. The ECSA of each sample was calculated based on the following equation (**Equation 3.1**):

$$ECSA = \frac{C_{area} \times A}{C_{ref}} \qquad \textbf{(Equation 3.1)}$$

Where, C_{area} is the areal capacitance, which is half the slope of the generated plot, A is the geometric area of the electrode, and C_{ref} is the nominal areal capacitance for Ni (40 μF cm^{-2}).[19]

3.3.7 Simulation

The diffusion equation (**Equation 3.2**), accounting for both concentration and potential gradients, was employed to investigate the diffusion kinetics of the 3DIG and 3DG cells,

$$\frac{\partial c}{\partial t} = \nabla \cdot \left(D \left[\nabla c + \frac{cZ}{kT} \nabla \phi \right] \right), \qquad \textbf{(Equation 3.2)}$$

where c is concentration, D is ionic diffusivity in the electrolyte, Z is the charge of the ionic species, ϕ is the electric potential field, T is absolute temperature and k is the Boltzmann constant. The electric potential field ϕ follows Poisson's equation (**Equation 3.3**),

$$\nabla^2 \phi = \frac{\rho}{\epsilon} \qquad \textbf{(Equation 3.3)}$$

where ρ and ϵ are volumetric charge and permittivity. Unit cells of the 3DIG and 3DG structures were used in simulations. In the 3DG structure, the x and z directions are treated as periodic, while the y direction is fixed to simulate two

parallel, separate electrodes. The same boundary conditions were applied to the 3DIG for a fair comparison. We considered a dilute limit for solving the electric field distribution, which was then used as input for the diffusion equation. All simulation parameters (**Table 3.2**) were non-dimensionalized to enhance the efficiency of numerical solutions.

Table 3.2. Simulation parameters for 3DIG and 3DG.

L_x	L_y	L_z	D^*	Δc^*	$\Delta \phi^*$
100 (220)	100	100	10	1	4

All simulation parameters are non-dimensionalized. $L_i, i = x, y, z$ is the simulation cell size. The L_x is 100 and 200 for 3DIG and 3DG simulation cell, respectively. D^* is the normalized diffusivity. Δc^* and $\Delta \phi^*$ is the applied concentration and potential difference between two electrodes.

3.4 Results and discussion

3.4.1 Surface morphology and structural characterization

The structural features of the 3DIG electrode were first examined. **Figure 3.1a** schematically illustrates the interpenetrating architecture, in which two independent gyroid networks (Gyroid 1 and Gyroid 2) are interwoven within the same volume. The fabrication process is outlined in **Figure 3.1b**: a polymer scaffold was printed, followed by surface activation, electroless plating, and nickel electrodeposition to yield the final metallized 3DIG electrode. Digital images (**Figures 3.1c, d**) confirmed that the interpenetrating framework was successfully reproduced, with two distinct gyroid networks extending continuously throughout the electrode volume. SEM imaging provided detailed insight into morphology. Low-

magnification SEM (**Figure 3.1e**) showed that the gyroid framework was preserved after metallization, with strut thicknesses of ~650-680 μm and channel openings of ~2.7 mm, consistent with the designed geometry. High-magnification SEM of the strut surface (**Figure 3.1f**) revealed a continuous nickel coating with granular texture, indicating that the electroless plating and electrodeposition processes produced conformal coverage without blocking the ordered transport channels. Elemental mapping of a representative strut (**Figure 3.1g**) confirmed a homogeneous distribution of nickel, demonstrating that metallization achieved uniform coverage across the entire scaffold, including the internal regions.

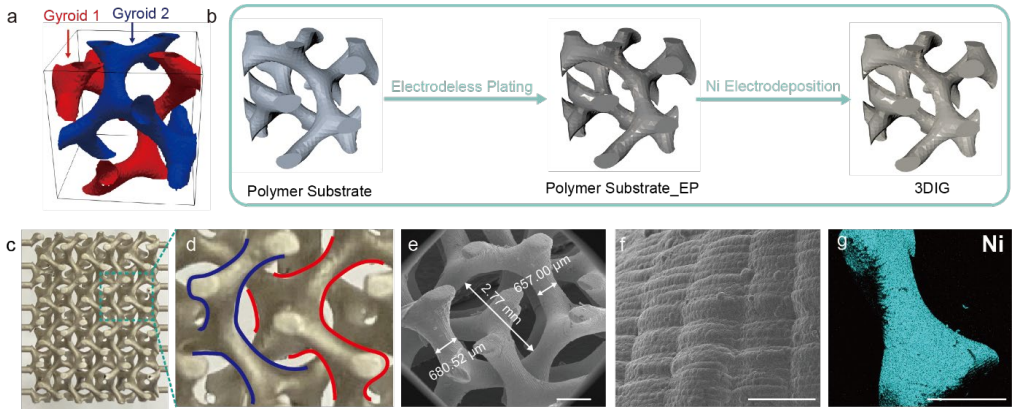

Figure 3.1. (a) Schematic illustration of an interpenetrating gyroid structure. Gyroid 1 and Gyroid 2 are highlighted with red and blue curves, respectively. (b) Schematic diagram showing the fabrication process of 3DIG. (c) Digital image of 3DIG. (d) Magnified image of the boxed region in (c). (e) SEM image of 3DIG showing the strut thickness and pore size. (f) SEM image of the surface of a 3DIG strut after metallization. (g) EDS elemental mapping of a single 3DIG strut showing the uniform distribution of Ni.

For comparison, the separate double 3D-printed gyroid (3DG, **Figure 3.2a**) electrodes were also characterized. A digital image of the 3DG device is shown in **Figure 3.2b**, where gyroid 1 and gyroid 2 were printed as independent scaffolds and arranged face-to-face with a finite interelectrode gap. SEM images (**Figures 3.2c-e**) confirmed the periodic arrangement of channels within the gyroid lattice. The struts displayed smooth curvature and well-defined pores, while the metallized surfaces appeared continuous and free of pore blockage, indicating that the coating procedures preserved the designed structure. Unlike the 3DIG configuration, however, the two gyroid networks in 3DG remain separate, resulting in longer ionic diffusion pathways across the electrode gap.

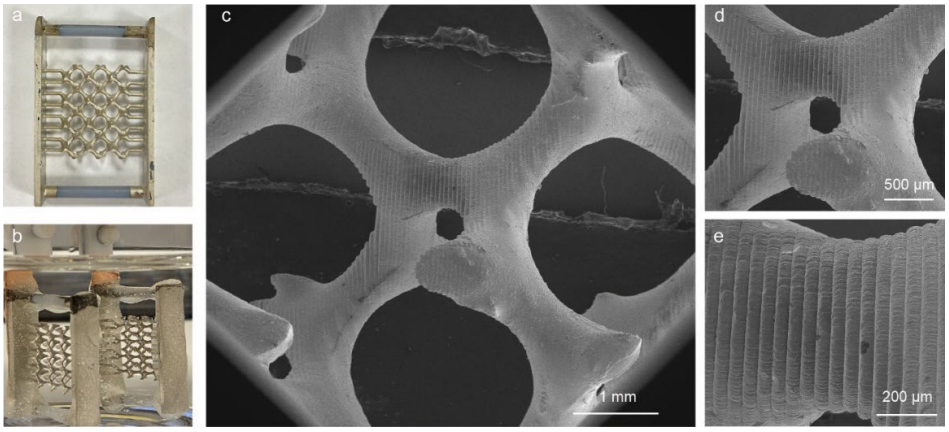

Figure 3.2. (a, b) Digital image of 3DG, where Gyroid 1 and Gyroid 2 electrodes are arranged in a separate configuration. (c-e) SEM images of a gyroid lattice under different magnifications.

The crystalline structure of the metallized electrodes was probed by X-ray diffraction (**Figure 3.3**). Both 3DIG and 3DG exhibited three major reflections at 44.5°, 51.8°, and 76.4°, which correspond to the (111), (200), and (220) planes of face-centered cubic Ni. These peaks match well with the reference Ni pattern

(PDF#04-0850), and no secondary phases were detected. The strong (111) reflection is consistent with the preferential orientation commonly observed in electrodeposited nickel. The similarity of diffraction profiles between 3DIG and 3DG indicates that both electrodes consist of crystalline nickel, and that performance differences are primarily attributable to architectural configuration rather than compositional factors.

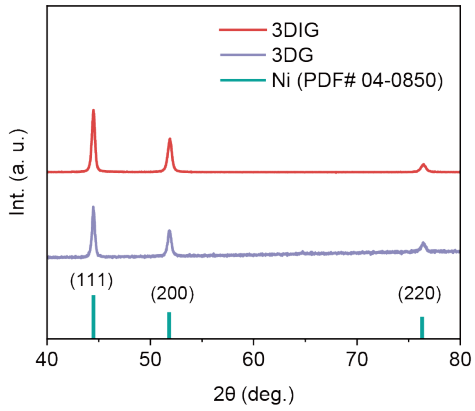

Figure 3.3. XRD patterns of 3DIG and 3DG. Standard Ni diffraction (PDF# 04-0850) is added for reference.

3.4.2 Ionic transport characteristics from simulation

Simulations were performed to compare ionic transport behavior in the 3DIG and 3DG architectures under constant concentration and potential gradients. **Figure 3.4a** plots the average normalized ion concentration in the electrolyte as a function of normalized time. The 3DIG electrode rapidly reached equilibrium, with the average concentration approaching unity almost instantaneously. In contrast, the 3DG electrode exhibited much slower equilibration, requiring significantly longer times to reach steady state. This result highlights the advantage of the interpenetrating configuration in accelerating ion replenishment across the

electrode volume. The spatial distribution of ion concentration at equilibrium further emphasizes these differences. In the 3DIG electrode (**Figure 3.4b**), the electrolyte concentration remained uniformly high throughout the channel network, indicating that the ordered interpenetrating architecture facilitates efficient ion transport and suppresses localized depletion zones. By comparison, the 3DG electrode (**Figure 3.4c**) displayed strong concentration gradients near the electrode surfaces, with pronounced depletion regions in the interelectrode gap. These findings are consistent with the longer effective diffusion distances inherent to the separated configuration.

The effect of electrode architecture on potential distribution was also analyzed. **Figure 3.4d** shows the normalized electric potential gradient magnitude in the 3DIG structure, which was uniformly distributed across the volume with minimal localized intensification. This indicates that the interpenetrating channels promote homogeneous electric field distribution and reduce resistive losses. In contrast, the 3DG electrode (**Figure 3.4e**) exhibited steep potential gradients concentrated near the electrode-electrolyte interface, reflecting inefficient ionic conduction and non-uniform utilization of the electrode. Overall, the simulation results demonstrate that the 3DIG architecture substantially improves ionic transport compared to the separated 3DG.

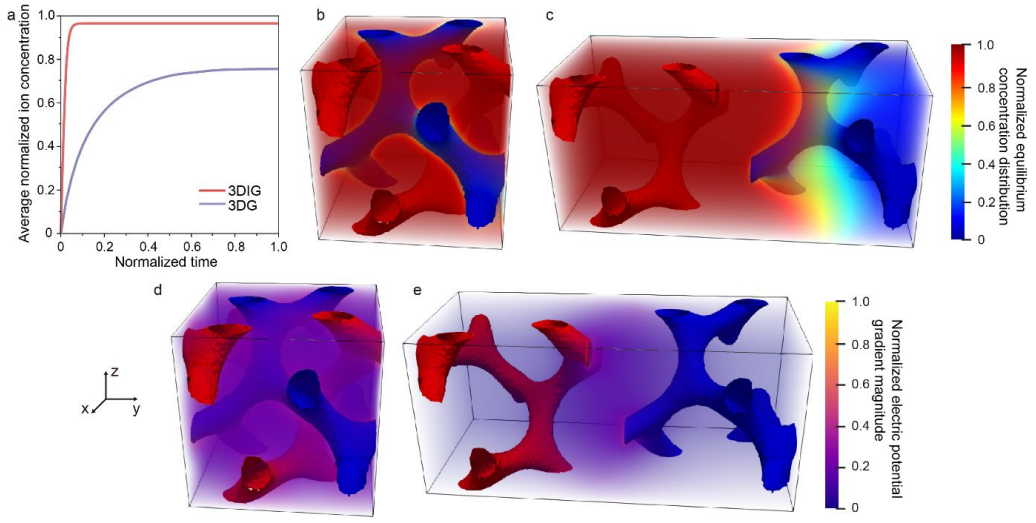

Figure 3.4. Simulation comparing ion diffusion kinetics in 3DIG and 3DG, driven by constant concentration and electric potential gradients. (a) Average normalized ion concentration in the electrolyte as a function of normalized time. Normalized equilibrium concentration distribution in (b) 3DIG and (c) 3DG. Normalized electric potential gradient magnitude in (d) 3DIG and (e) 3DG.

3.4.3 Electrochemical performance

We studied the electrochemical performance of the 3DIG and 3DG. To evaluate the influence of geometric design parameters on electrochemical performance, interpenetrating gyroid electrodes with different unit cell lengths were fabricated (**Figure 3.5a** and **Table 3.1**). Digital images of the printed structures (**Figures 3.5b-d**) show well-defined 3DIG architectures with unit cell lengths of 4, 6, and 8 mm, corresponding to overall electrode thicknesses of 3.5, 5.5, and 8.0 mm, respectively. The ordered channels were preserved across all feature sizes, enabling systematic investigation of the effect of structural dimension on transport behavior.

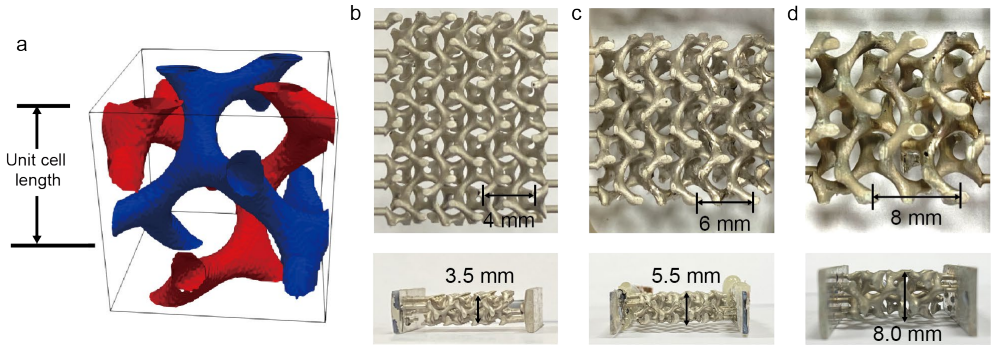

Figure 3.5. (a) Schematic illustration of a repeating unit in the interpenetrating gyroid structure. Digital images show interpenetrating gyroid structures with different unit cell lengths (b) 4 mm, (c) 6 mm, and (d) 8 mm. These electrodes' thicknesses are 3.5 mm, 5.5 mm, and 8 mm, respectively.

LSV curves collected in 1.0 M KOH at a scan rate of 1.0 mV s^{-1} revealed clear feature-size-dependent performance. (**Figure 3.6a**) The 3DIG electrode with a unit cell length of 4 mm exhibited the highest geometric current density, reaching nearly 1000 mA cm^{-2} at ~2.85 V. By comparison, electrodes with 6 and 8 mm unit cells achieved the current densities of only 659 and 449 mA cm^{-2} respectively, at the same cell voltage, reflecting increased transport resistance associated with longer pathways and thicker electrodes. To decouple the contribution of electrochemically active surface area (ECSA), the current densities were normalized by ECSA values (**Table 3.3**). Even after normalization, as shown in **Figure 3.6b**, the 4 mm electrode maintained superior activity compared to the 6 and 8 mm counterparts. This result indicates that the performance improvement cannot be attributed solely to a larger accessible surface area. Instead, the smaller unit cell length and reduced electrode thickness shorten ionic diffusion distances, improve electrolyte penetration, and

facilitate bubble evacuation, thereby mitigating ion transport limitations at high current densities.

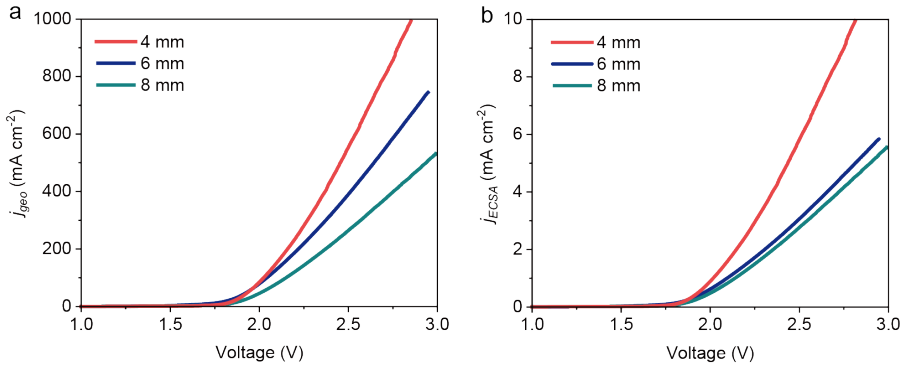

Figure 3.6. LSVs of 3DIG with different feature sizes collected in 1.0 M KOH at a scan rate of 1.0 mV s^{-1} (a) under geometric current density and (b) are plotted in ECSA-normalized current density.

Table 3.3. The ECSA of 3DIG with different feature sizes

Feature size (mm)	ECSA (cm^2)
4	95.25
6	127.5
8	95.75

These findings demonstrate that optimizing the feature size of interpenetrating gyroid electrodes plays a critical role in enhancing their high-rate performance. The 4 mm gyroid configuration provides the most favorable balance between structural integrity and transport efficiency, establishing it as the optimal design for subsequent electrochemical testing.

The electrochemical performance of the 3DG electrodes was also evaluated. Digital images of the fabricated electrodes are shown in **Figure 3.7a**. Two

independent gyroid scaffolds, denoted as gyroid 1 and gyroid 2, were arranged in a face-to-face configuration with a separation distance set to 5 mm, which represents the minimum spacing achievable in our test cell (**Figure 3.7b**). This geometry retains the structural characteristics of individual gyroids but introduces a finite ionic diffusion gap between the two electrodes.

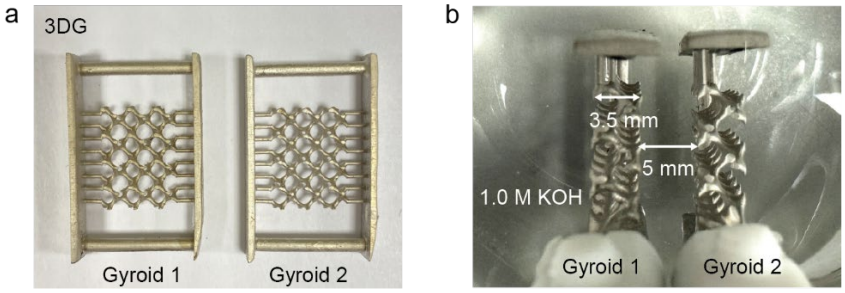

Figure 3.7. (a) Digital images of two 3DG electrodes. (b) The distance between the two 3DG electrodes was set to be 5 mm for the water splitting test.

The polarization behavior of 3DG electrodes with varied separation distances is shown in **Figure 3.8**. When the interelectrode gap was reduced from 20 mm to 10 mm and further to 5 mm, the current density at a given voltage increased correspondingly. The improvement at shorter spacing reflects reduced ionic transport distance across the electrolyte. However, even at the minimum separation of 5 mm, the 3DG electrodes required considerably higher voltages to reach industrially relevant current densities, indicating persistent mass-transport limitations imposed by the electrolyte gap.

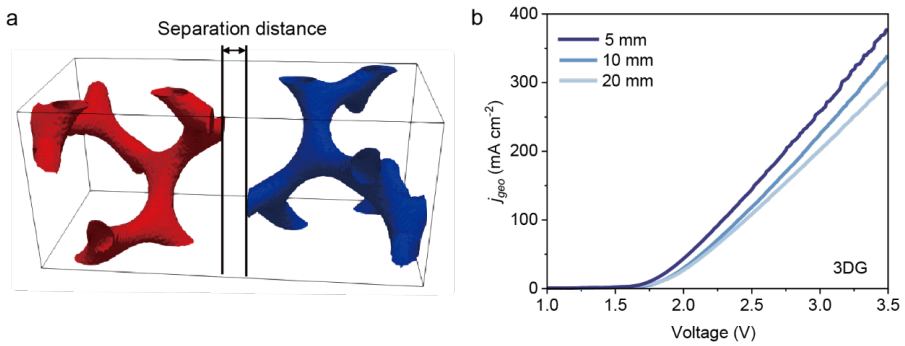

Figure 3.8. (a) The schematic illustration of 3DG and (b) LSVs of 3DG with separation distances collected in 1.0 M KOH at a scan rate of 1.0 mV s^{-1} are plotted in geometric current density.

A direct comparison of the optimized 3DIG electrodes with the 3DG configuration is presented in **Figure 3.9** and **3.10**. The interpenetrating architecture delivered dramatically enhanced performance, achieving 1000 mA cm^{-2} at ~2.85 V, whereas the 3DG electrodes produced less than quarter of that current density under the same potential (~225 mA cm^{-2}). After normalization by ECSA (**Figure 3.9**), the 3DIG electrodes still exhibited significantly superior activity (**Figure 3.10**), confirming that the advantage arises from architectural differences rather than variations in accessible surface area. Specifically, the interpenetrating design eliminates the bulk electrolyte gap between opposing electrodes and provides continuous, reduced ion pathways, thereby enabling more efficient transport and higher utilization of the electrode volume.

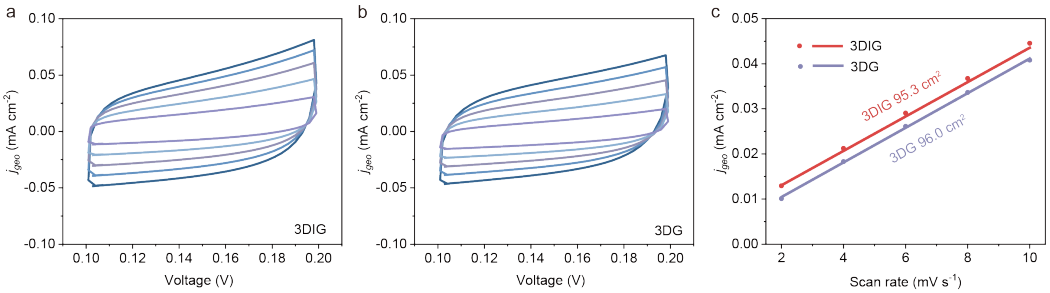

Figure 3.9. CV curves of (a) 3DIG and (b) 3DG collected in 1.0 M KOH at different scan rates from 2 to 10 mV s^{-1} at an interval of 2.0 mV s^{-1}. The data obtained in the potential range from 0.1 to 0.2 V are used to determine the electrode's ECSA. (c) The geometric current density of 3DIG and 3DG are plotted as a function of scan rate.

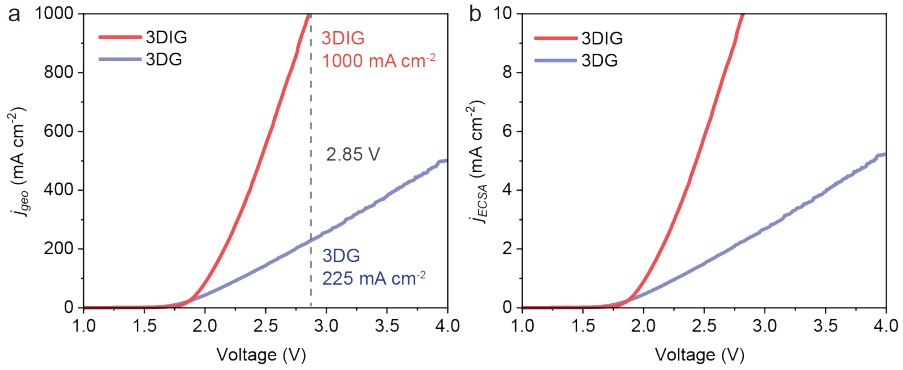

Figure 3.10. LSVs of 3DIG and 3DG collected in 1.0 M KOH at a scan rate of 1.0 mV s^{-1} are plotted in (a) geometric current density and (b) ECSA-normalized current density.

3.4.4 Electrochemical impedance analysis

Electrochemical impedance spectroscopy (EIS) was carried out to further probe the transport and interfacial properties of the interpenetrating 3DIG and the separate 3DG electrodes under different operating conditions. At room temperature,

the Nyquist plots of both electrodes displayed a characteristic high-frequency intercept and a semicircle (**Figure 3.11a**), which could be fitted using an equivalent circuit containing a solution resistance (R_S) and a charge-transfer resistance (R_{CT}). The 3DIG electrode exhibited a noticeably smaller high-frequency intercept and a significantly reduced semicircle diameter compared to 3DG, directly corresponding to lower R_S and R_{CT} values (**Figures 3.11b** and **c**). Quantitative analysis revealed that the solution resistance of 3DIG was reduced by more than a factor of two relative to 3DG, while its R_{CT} was nearly halved. The lower R_S reflects more efficient ionic conduction within the electrode, enabled by shorter transport distances and the elimination of the bulk electrolyte gap in the interpenetrating design. Meanwhile, the reduced R_{CT} highlights improved interfacial kinetics, which can be attributed to more homogeneous ion access across the interconnected gyroid channels. These differences at room temperature already establish that the architectural features of 3DIG play a decisive role in mitigating both ionic transport resistance and kinetic barriers.

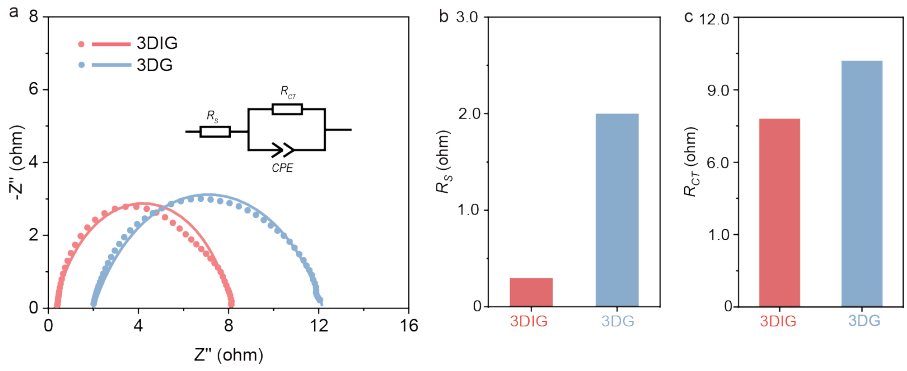

Figure 3.11. (a) Nyquist plots of 3DIG and 3DG are obtained in a frequency range from 100 kHz to 1.0 Hz under an amplitude of 5 mV. Circles represent experimental data. The solid lines represent fitting curves based on the equivalent circuit model (inset). Histograms show the (b) R_S and (c) R_{CT} values of 3DIG and 3DG.

To further examine how temperature influences these resistive components, impedance measurements were conducted at 275, 298, and 318 K. As shown in **Figure 3.12a**, the LSV curves of both 3DIG and 3DG electrodes showed the expected decline in current density at lower temperatures due to reduced ionic diffusivity in alkaline electrolyte. However, the impact of temperature was far less pronounced for the 3DIG electrode. Even at 275 K, the 3DIG electrode was able to sustain substantially higher current densities at given voltages compared with the 3DG electrode. The voltage ratio analysis at fixed current densities (200 and 400 mA cm^{-2}, **Figure 3.12b**) quantitatively illustrates this effect: although the performance gap narrowed slightly as temperature increased, the 3DIG electrodes consistently required lower voltages than 3DG across the full range. The advantage was most prominent at 275 K, where ionic mobility is most restricted at lower temperature, demonstrating that the interpenetrating channels of 3DIG substantially alleviate diffusion limitations under demanding conditions.

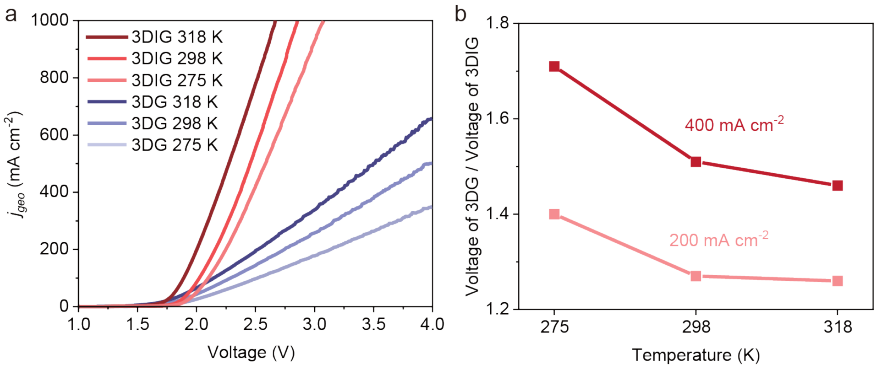

Figure 3.12. (a) LSVs of 3DIG and 3DG collected in 1.0 M KOH at a scan rate of 1.0 mV s^{-1} at different temperatures. (b) The 3DG/3DIG voltage ratios obtained at 200 and 400 mA cm^{-2} are plotted as a function of temperature.

The Nyquist plots obtained at different temperatures further clarify these observations. For the 3DIG electrodes (**Figure 3.13a**), both the semicircle diameter and the high-frequency intercept remained small across the entire temperature range, reflecting stable and low values of both R_S and R_{CT}. In contrast, the 3DG electrodes (**Figure 3.13b**) showed a pronounced enlargement of the semicircle at lower temperatures, especially at 275 K, indicative of severe interfacial polarization and elevated solution resistance. The extracted resistance values (**Figures 3.13c** and **d**) confirmed that the R_S of 3DG increased to several ohms at 275 K, whereas 3DIG maintained values close to 1.0 Ω. Similarly, the R_{CT} of 3DG reached values above 10.0 Ω at 275 K, while 3DIG stabilized around 3.5 Ω. This sharp contrast highlights that the ordered, reduced ion channels in the interpenetrating design provide a level of robustness against reduced diffusivity that cannot be achieved by the separated configuration.

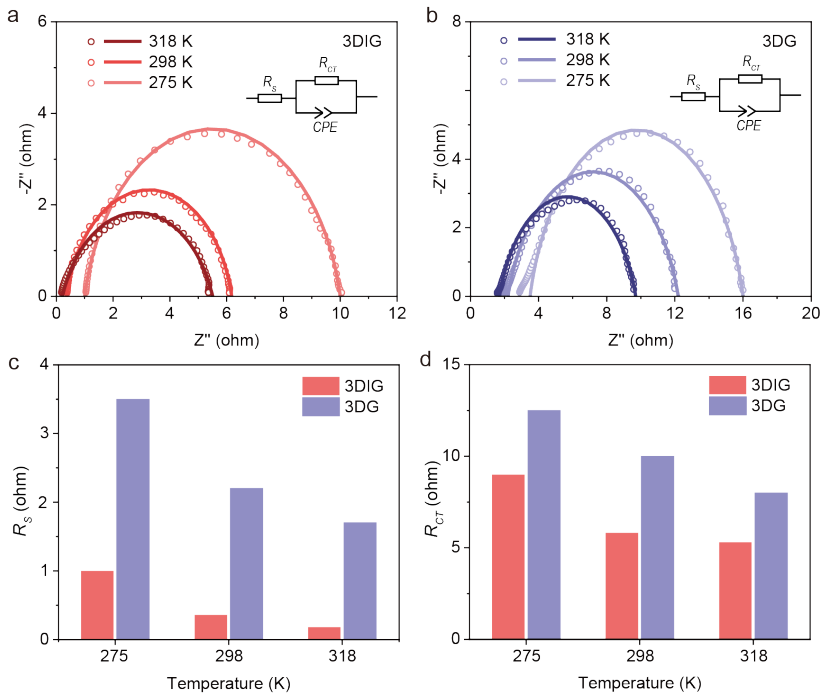

Figure 3.13. Nyquist plots of (a) 3DIG and (b) 3DG collected in a frequency range from 100 kHz to 1.0 Hz at an amplitude of 5 mV at different temperatures. Circles are experimental data. Solid lines are fitting curves based on the equivalent circuit model. Histograms show the (c) R_S, and (d) R_{CT} of 3DIG and 3DG at different temperatures.

The impedance behavior was also evaluated as a function of operating current density, spanning from 10 to 200 mA cm^{-2} (**Figure 3.14**). Nyquist plots of the 3DIG electrodes (**Figure 3.14a**) demonstrated a systematic reduction in semicircle size as current density increased, consistent with accelerated kinetics under stronger driving forces. The fitting results showed that R_{CT} decreased from ~3.5 Ω at 10 mA cm^{-2} to below 1.0 Ω at 200 mA cm^{-2}, while R_S remained essentially constant at ~0.5-0.7 Ω across the range (**Figures 3.14c** and **d**). By comparison, 3DG electrodes (**Figure 3.14b**) exhibited consistently larger semicircles and higher intercepts, with R_S exceeding 2.0 Ω across the entire range and R_{CT} starting as high as ~9.0-10.0 Ω at 10 mA cm^{-2} before dropping to ~2.0 Ω at 200 mA cm^{-2}. The fact that 3DIG maintains both low R_S and low R_{CT} across current densities underscores that the interpenetrating architecture not only improves ionic transport but also sustains more uniform charge-transfer kinetics as the reaction rate increases.

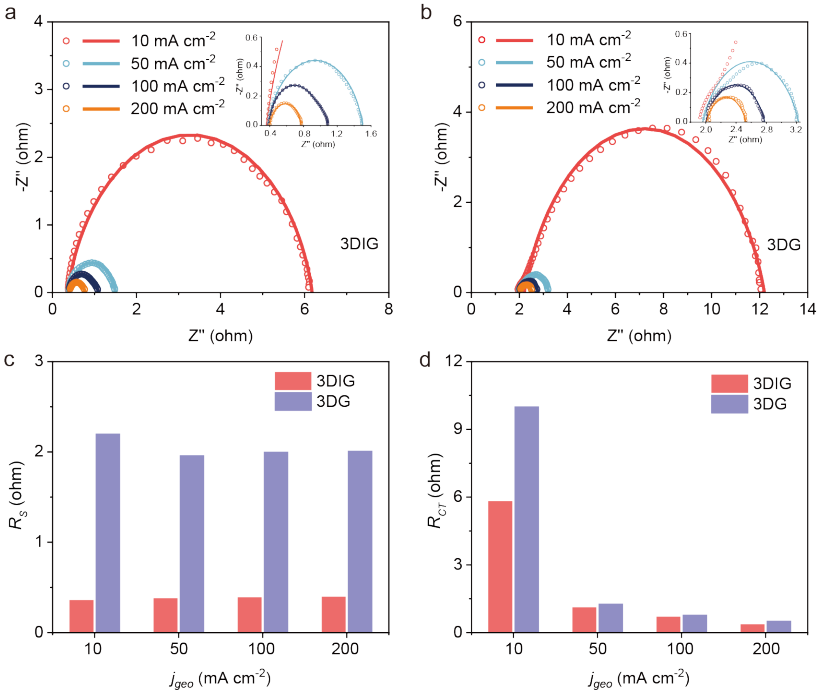

Figure 3.14. Nyquist plot of (a) 3DIG and (b) 3DG, in a frequency range from 100 kHz to 1.0 Hz at an amplitude of 5 mV at different current densities. Circles are experimental data. Solid lines are fitting curves based on the equivalent circuit model. Insets: Magnified Nyquist plots in the high-frequency region. Histograms show the (c) solution resistance and (d) charge transfer resistance of 3DIG and 3DG obtained at different current densities.

In conclusion, these impedance studies provide a comprehensive picture of the transport advantages afforded by the 3DIG design. At room temperature, the interpenetrating electrode already exhibits significantly lower resistances than the separated 3DG. Under reduced temperatures, these advantages become even more pronounced, highlighting the robustness of the architecture in conditions where ionic diffusivity is typically the limiting factor. Furthermore, across a wide range of current densities, 3DIG maintains stable and low R_S together with sharply reduced

R_{CT}, enabling efficient operation at industrially relevant current densities. Overall, the EIS results confirm that the interpenetrating architecture fundamentally alters the transport environment by shortening diffusion lengths, and homogenizing ionic flux distribution, thereby providing a decisive advantage for high-rate alkaline water splitting.

3.4.5 Long-Term Stability

The durability of the 3DIG electrodes under high-rate operation was examined using chronoamperometric measurements in a beaker cell (**Figure 3.15a**). As shown in **Figure 3.15b**, the interpenetrating electrodes were operated at a fixed cell voltage of 2.4 V for 100 h. the initial current density is 366 mA cm^{-2}, and it retains 97 % of its initial value after 100 h, demonstrating excellent long-term electrochemical stability under demanding conditions.

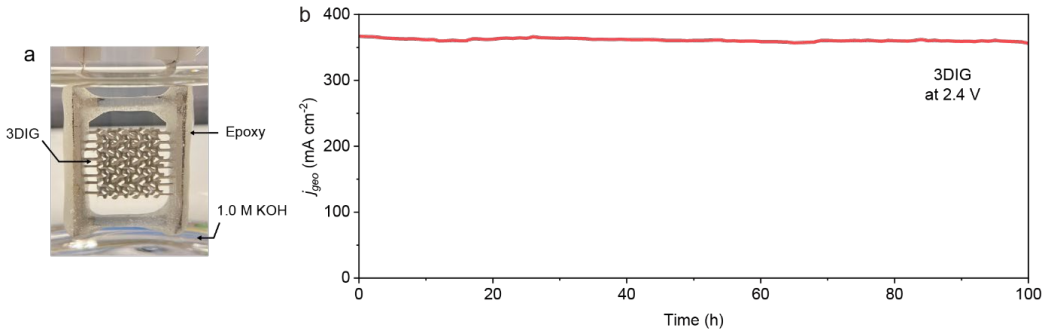

Figure 3.15. (a) Digital image of 3DIG device. (b) The current density of 3DIG obtained at 2.4 V in 1.0 M KOH is plotted as a function of time.

3.4.6 Catalyst modification of 3DIG electrodes

To further enhance the electrochemical performance of the 3DIG electrode, surface modification was carried out following previously established strategies. Metallic Ni nanocones were first electrodeposited onto the gyroid electrode surface

to facilitate bubble release from the substrate. Our previous study demonstrated that nanocone-modified electrodes can promote gas bubble detachment by transforming the surface into an underwater superaerophobic state. This surface modification strategy was therefore applied to the 3DIG framework to improve gas-release dynamics while preserving the ordered architecture.

After nanocone growth, the surface was further decorated with a layer of NiFeOOH catalyst using a previously reported electrodeposition method.[17] **Figure 3.16a** presents a digital image of the modified electrode (denoted as NiFeOOH@3DIG), where the originally shiny metallic surface of 3DIG became dark grey after the catalyst deposition. SEM images revealed that the additional coating on the interpenetrating electrodes was uniform and did not cause structural blockage or distortion of the gyroid channels (**Figure 3.16b**). Magnified SEM images confirmed the retention of the nanocone-modified surface morphology after NiFeOOH deposition (**Figure 3.16c**).

Although the thin NiFeOOH catalyst layer was not directly distinguishable in SEM images, elemental mapping analysis showed a uniformly distributed Fe signal along the struts of the gyroid lattice (**Figure 3.16d**), confirming the successful and homogeneous deposition of NiFeOOH. Importantly, the interpenetrating gyroid architecture remained intact after both nanocone growth and catalyst coating, ensuring that the ordered porous network was preserved.

Electrochemical measurements demonstrated that NiFeOOH@3DIG exhibited improved electrochemical performance compared to unmodified 3DIG, as evidenced by a reduction in overpotential (**Figure 3.16e**). These results indicate that combining nanocone-induced bubble detachment enhancement with NiFeOOH

catalytic activity provides a synergistic improvement in overall device performance while maintaining the structural advantages of the interpenetrating gyroid framework.

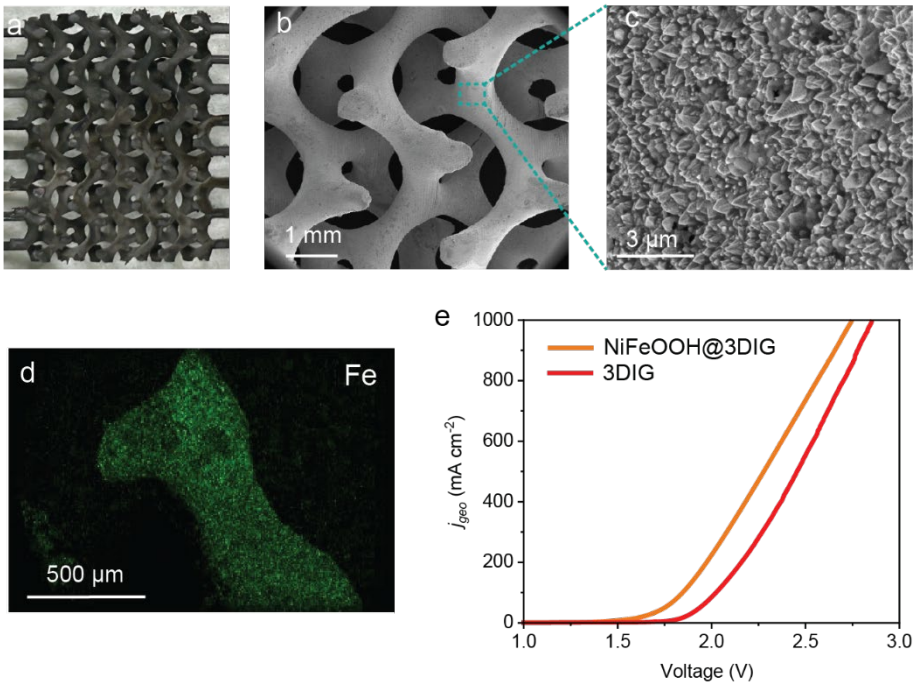

Figure 3.16. (a) Digital image and (b) SEM image of NiFeOOH@3DIG. (c) Magnified SEM image showing the region highlighted by the box in (b). (d) EDS elemental mapping obtained from a strut of NiFeOOH@3DIG shows the distribution of Fe signal. (e) LSVs of 3DIG and NiFeOOH@3DIG collected in 1.0 M KOH at a scan rate of 1.0 mV s^{-1}.

3.5 Conclusion

In this chapter, we addressed the ion-diffusion limitations that emerge as a critical bottleneck in high-rate alkaline water splitting once bubble accumulation is mitigated. A 3D-printed interpenetrating gyroid electrode was developed to provide

ordered, and reduced interelectrode distance, thereby enhancing electrolyte accessibility and ionic transport.

Structural analyses confirmed that the interpenetrating framework preserved high porosity and uniform metallization while maintaining the fidelity of the designed architecture. Finite element simulations demonstrated that 3DIG establishes smoother potential gradients and more uniform ionic concentration profiles compared to separated gyroid electrodes, consistent with lower tortuosity and improved transport behavior. Electrochemical impedance measurements further verified that the interpenetrating geometry reduces both solution resistance and charge-transfer resistance. Importantly, these transport advantages persisted even under reduced-temperature conditions, highlighting the robustness of the design. Finally, long-term chronoamperometric tests established that the 3DIG electrodes maintain their structural integrity and catalytic activity over extended operation.

In conclusion, these findings demonstrate that interpenetrating gyroid architecture offers a general strategy to overcome ion-diffusion barriers in alkaline electrolyzers. By rationally engineering tortuosity, porosity, and electrode spacing, the 3DIG design complements the bubble-detachment strategy established in Chapter 2, providing a unified framework for addressing both gas and ion transport challenges in high-rate water splitting.

References

1. Ehlers, J. C.; Feidenhans'l, A. A.; Therkildsen, K. T.; Larrazábal, G. O., *ACS Energy Lett.* **2023,** *8*, 1502-1509.

2. Yu, Z.-Y.; Duan, Y.; Feng, X.-Y.; Yu, X.; Gao, M.-R.; Yu, S.-H., *Adv. Mater.* **2021,** *33*, 2007100.

3. Wan, L.; Xu, Z.; Xu, Q.; Pang, M.; Lin, D.; Liu, J.; Wang, B., *Energy Environ. Sci.* **2023,** *16*, 1384-1430.

4. Clament Sagaya Selvam, N.; Kwak, S. J.; Choi, G. H.; Oh, M. J.; Kim, H.; Yoon, W.-S.; Lee, W. B.; Yoo, P. J., *ACS Energy Lett.* **2021,** *6*, 4345-4354.

5. Zheng, Y.; Serban, A.; Zhang, H.; Chen, N.; Song, F.; Hu, X., *ACS Energy Lett.* **2023,** *8*, 5018-5024.

6. Li, Y.; Wei, B.; Yu, Z.; Bondarchuk, O.; Araujo, A.; Amorim, I.; Zhang, N.; Xu, J.; Neves, I. C.; Liu, L., *ACS Sustainable Chem. Eng.* **2020,** *8*, 10193-10200.

7. Yang, H.; Driess, M.; Menezes, P. W., *Adv. Energy Mater.* **2021,** *11*, 2102074.

8. Kou, T.; Wang, S.; Li, Y., *ACS Mater. Lett.* **2021,** *3*, 224-234.

9. Luo, Y.; Zhang, Z.; Chhowalla, M.; Liu, B., *Adv. Mater.* **2022,** *34*, e2108133.

10. Ren, Q.; Feng, L.; Ye, C.; Xue, X.; Lin, D.; Eisenberg, S.; Kou, T.; Duoss, E. B.; Zhu, C.; Li, Y., *Adv. Energy Mater.* **2023,** *13*, 2302073.

11. Kou, T.; Wang, S.; Shi, R.; Zhang, T.; Chiovoloni, S.; Lu, J. Q.; Chen, W.; Worsley, M. A.; Wood, B. C.; Baker, S. E.; Duoss, E. B.; Wu, R.; Zhu, C.; Li, Y., *Adv. Energy Mater.* **2020,** *10*, 2002955.

12. Márquez, R. A.; Kawashima, K.; Son, Y. J.; Rose, R.; Smith, L. A.; Miller, N.; Carrasco Jaim, O. A.; Celio, H.; Mullins, C. B.,. *ACS Appl. Mater. Interfaces* **2022,** *14*, 42153-42170.

13. Ma, T.; Xu, W.; Li, B.; Chen, X.; Zhao, J.; Wan, S.; Jiang, K.; Zhang, S.; Wang, Z.; Tian, Z.; Lu, Z.; Chen, L., *Angew. Chem., Int. Ed.* **2021,** *60*, 22740-22744.

14. Beall, C. E.; Fabbri, E.; Schmidt, T. J., *ACS Catal.* **2021,** *11*, 3094-3114.

15. Rocha, F.; Delmelle, R.; Georgiadis, C.; Proost, J., *Adv. Energy Mater.* **2022,** *13*, 2203087.

16. Liu, S.; Feng, J.; Bian, X.; Liu, J.; Xu, H.; An, Y., *Energy Environ. Sci.* **2017,** *10*, 1222-1233.

17. Zhou, H.; Yu, F.; Zhu, Q.; Sun, J.; Qin, F.; Yu, L.; Bao, J.; Yu, Y.; Chen, S.; Ren, Z., *Energy Environ. Sci.* **2018**, *11*, 2858-2864.

18. Feng L. L., Yu G., Wu Y., Li G. D., Li H., Sun Y., Asefa T., Chen W., Zou X., *J. Am. Chem. Soc.* **2015**, 137, 14023.

19. Kou T. , Wang S., Hauser J. L., Chen M., Oliver S. R. J., Ye Y., Guo J., Li Y., *ACS Energy Lett.* **2019**, 4, 622.

Chapter 4

Ni^{3+}-Enriched Nickel Sulfide Catalysts for Urea Oxidation

4.1 Abstract

The high thermodynamic potential of the oxygen evolution reaction (OER, 1.23 V vs. RHE) fundamentally limits the energy efficiency of alkaline water splitting, even when electrode architecture and bubble management are optimized. To address this intrinsic constraint, this chapter investigates the urea oxidation reaction (UOR) as an alternative anodic process with a substantially lower theoretical potential (0.37 V vs. RHE), enabling energy-efficient hydrogen generation while simultaneously treating urea-rich wastewater. Unlike conventional Ni-based catalysts that rely on in-situ electrochemical oxidation of Ni^{2+} to Ni^{3+} at elevated anodic potentials, this work develops a valence-state engineering strategy to intrinsically enrich Ni^{3+} species within a nickel sulfide framework by controlling sulfur precursor concentration during hydrothermal synthesis. Systematic structural and spectroscopic analyses confirmed that modulation of sulfur stoichiometry enables precise tuning of the Ni^{3+}/Ni^{2+} ratio, establishing a direct correlation between intrinsic Ni^{3+} enrichment and enhanced UOR kinetics. The optimized Ni_3S_2 catalyst delivers a current density of 100 mA cm^{-2} at 1.361 V vs. RHE and maintains stable operation for over 100 h under alkaline UOR conditions. Electrochemical impedance spectroscopy revealed accelerated interfacial charge-transfer kinetics associated with increased Ni^{3+} content. Density functional theory calculations further demonstrate that sulfur incorporation modifies the electronic environment of Ni sites, providing a more energetically favorable pathway for C-N bond cleavage and lowering the energy barrier of the rate-determining step

compared to sulfur-free $Ni(OH)_2$. To assess system-level performance, the optimized catalyst is integrated into a three-dimensional interpenetrating electrode architecture and operated in a flow-cell configuration. The architecture-driven enhancement of mass transport and gas removal enables sustained high-rate operation under continuous UOR conditions. This chapter establishes intrinsic Ni valence modulation through sulfur engineering as an effective strategy to advance UOR kinetics, and demonstrates how coupling catalyst-level electronic control with device-level transport optimization provides a scalable pathway toward energy-efficient hydrogen production integrated with wastewater remediation.

4.2 Introduction

Alkaline water splitting represents a promising technology for sustainable hydrogen production; however, its overall energy efficiency is fundamentally constrained by the anodic oxygen evolution reaction (OER).[1-5] Despite extensive efforts devoted to improving OER electrocatalysts, the OER remains a major energy-limiting step in water splitting because of its high equilibrium potential of 1.23 V vs. RHE and sluggish reaction kinetics.[6-8] As demonstrated in Chapters 2 and 3, interfacial bubble management and electrode architecture engineering can substantially alleviate mass-transport limitations and enable stable operation at industrially relevant current densities. Nevertheless, even when transport-related constraints are mitigated, the high anodic potential associated with OER remains a dominant bottleneck that limits further reductions in cell voltage and overall energy consumption.

A promising strategy to address this limitation is to replace the OER with a more thermodynamically favorable anodic oxidation reaction. Among various

candidates, the urea oxidation reaction (UOR) is particularly attractive due to its much lower theoretical potential of 0.37 V vs. RHE.[9-11] When coupled with the HER, UOR-enabled electrolysis substantially reduces the required energy input compared to conventional water splitting. Moreover, since urea originates largely from human and animal urine as well as fertilizer runoff, it is abundant in various wastewater streams.[12-14] Therefore, integrating UOR with water splitting not only enhances energy efficiency but also enables simultaneous wastewater remediation.

Despite these advantages, UOR is kinetically sluggish. The reaction involves a complex six-electron transfer process ($CO(NH_2)_2 + 6OH^- \rightarrow N_2 + CO_2 + 5H_2O + 6e^-$), accompanied by multiple bond-breaking and bond-forming steps.[15, 16] Among these, urea adsorption, dehydrogenation, and C-N bond cleavage constitute the primary kinetic barriers. Consequently, the development of high-performance and stable electrocatalysts is essential. Nickel-based catalysts have emerged as promising candidates owing to their earth abundance, favorable electronic structure, and electrochemical properties.[17-21] Their catalytic mechanism is strongly influenced by electrolyte composition and pH.[11, 22-24] In alkaline media, most Ni-based (pre)catalysts such as $Ni(OH)_2$ undergo in-situ oxidation from Ni^{2+} to NiOOH, generating catalytically active Ni^{3+} species. These Ni^{3+} sites promote the adsorption and dehydrogenation of urea molecules into CO* and NH* intermediates, eventually producing N_2 and CO_2.[25, 26] However, this $Ni^{2+} \rightarrow Ni^{3+}$ valence transition typically occurs at relatively high potentials (~1.36 V vs. RHE), leading to additional energy input and higher overpotential.[27] Furthermore, NiOOH often suffers from poor electrical conductivity. Therefore, strategies that promote Ni^{3+}

formation at lower potentials[28, 29] or intrinsically enrich Ni^{3+} within the catalyst framework[30] represent promising approaches for improving UOR efficiency.

In this chapter, a controllable hydrothermal synthesis strategy is developed to tune the sulfur stoichiometry of nickel sulfide (Ni_3S_2), enabling intrinsic enrichment of Ni^{3+} species within the catalyst. X-ray photoelectron spectroscopy (XPS) analysis confirms that adjusting the sulfur precursor concentration allows systematic tuning of the Ni^{3+}/Ni^{2+} ratio. The optimized Ni_3S_2 electrode achieves a current density of 100 mA cm^{-2} at only 1.361 V vs. RHE and maintains over 90% of its initial activity after 100 h of continuous operation. Density functional theory (DFT) calculations further reveal that Ni_3S_2 significantly lowers the free energy barrier for the dissociation of adsorbed $CO(NH_2)_2$* into CO* and NH* intermediates compared to sulfur-free $Ni(OH)_2$, and that increasing the Ni^{3+} fraction within the sulfide framework further reduces the activation barrier of the rate-determining step. Beyond catalyst-level optimization, Ni_3S_2 is integrated with the three-dimensional interpenetrating electrode architecture developed and evaluated in a flow-cell configuration. This architecture-driven approach enhances mass transport, facilitates gas bubble transport, and enables stable high-rate operation. Through the combined strategies of reaction-level substitution, valence-state engineering, and architecture-enabled transport optimization, this chapter establishes an effective pathway toward energy-efficient hydrogen production coupled with urea-rich wastewater remediation.

4.3 Experimental section

4.3.1 Structural characterization

Sample morphologies and elemental mapping of samples were characterized by SEM (Thermo Scientific Scios 2 DualBeam, equipped with an Oxford Instruments AZtecLive Ultim Max 100 EDS detector). Crystal phases were investigated by XRD (Rigaku SmartLab). XPS spectra were collected by using Kratos Analytical AXIS Ultra Delay-Line Detector (DLD) instrument. Prior to XPS measurements, samples underwent electrochemical conditioning: specifically, 40 cyclic voltammetry (CV) cycles were performed in 1.0 M KOH within a potential window of 0 to 0.8 V vs. Hg/HgO at 10 mV s^{-1}, LSVs were collected before and after the CV scans, and the conditioning was considered complete once the pre- and post-CV LSV curves overlapped, indicating that the electrode had reached a stable state. Transmission electron microscopy (TEM) images were acquired using a FEI Talos F200X microscope.

4.3.2. 3D printing of interpenetrated polymer substrates and flow cell device

Interpenetrated lattice polymer structures were printed using a commercial masked stereolithography apparatus (Mars 5 Ultra, Elegoo). The KC-body centered cell interpenetrated electrodes used in this work were generated using 3D computer graphics and computer aided design software (nTopology). Both BCC and KC use a 3 × 3 × 3 mm unit cell. The unit cells were repeated in a 5 × 4 grid resulting in a 15 × 12 × 3 mm interpenetrated electrode. The outer support is made up of a simple cubic lattice with a unit cell of 1 × 1 × 1 mm with overall dimensions of 30 × 22 × 5 mm. Flow cell components were fabricated on a commercial stereolithography 3D printer (Form 3, Formlabs) using Autodesk Inventor for CAD design. All 3D-

printed parts were rinsed and sonicated in isopropyl alcohol for 10 min to remove uncured resin, and then post-cured under 405 nm light (Form Cure, Formlabs) at 60 °C for 1 h.

4.3.3 Ni deposition of 3D-printed interpenetrating electrodes

Metallization of the 3D-printed polymer substrate followed a previously reported method with minor modifications.[31] First, the printed structures were immersed in 300 mL of 1.0 M NaOH solution at 45 °C for 30 min to activate the surface. They were then sequentially treated in two separate solutions: one containing 6.0 g of $SnCl_2$ and 6.0 mL of HCl, and another containing 60 mg of $PdCl_2$ and 1.5 mL of HCl, both maintained at 45 °C for 1 h. These sensitization and activation steps enabled the deposition of Pd catalytic sites via redox interactions. Next, the substrates underwent electroless nickel plating by immersion in 300 mL of a solution composed of 3.9 g $NiSO_4$, 6.3 g citric acid, and 3.18 g sodium hypophosphite at 70 °C for 10 minutes, yielding a conductive Ni-P coating. In this process, Pd particles functioned as nucleation sites for Ni-P deposition, facilitating the formation of a uniform metal layer across the polymer surface. To further improve electrical conductivity, electrochemical nickel deposition was performed in a two-electrode setup, where the nickel-coated polymer substrate served as the working electrode and a piece of Ni foam was used as the counter electrode. The deposition bath consisted of 100 mL of aqueous solution containing 4.0 g $NiSO_4$ and 0.64 g NH_4Cl. A potential of 2.0 V was applied for 1 h. After deposition, the samples were rinsed thoroughly with deionized water and ethanol and air-dried to obtain metallized 3D-printed interpenetrating electrode (3DIE).

4.3.4. Synthesis of nickel sulfide on Ni substrates

A piece of Ni foam (1.5 × 3 cm) or 3DIE (1.2 × 1.5 cm) was immersed in a solution containing thioacetamide (0, 10, 20, 30 and 40 mM), sodium sulfate (0.65 mM), and sodium hydroxide (11.25 mM) in 15 mL of deionized water. Prior to use, the Ni foam substrate was cleaned by sonication in acetone, 3.0 M HCl, and ethanol for 15 minutes each. The solution and Ni foam were then transferred into a 30 mL Teflon-lined stainless-steel autoclave. The sealed autoclave was heated at 150 °C in an electric oven for 6 h and then allowed to cool down to room temperature. The Ni substrate was taken out, thoroughly washed with deionized water and ethanol, and dried under ambient conditions. The Ni foam-based samples with different concentrations of thioacetamide were labelled as $Ni(OH)_2$, Ni_3S_2_1.0, Ni_3S_2_2.0, Ni_3S_2_3.0, Ni_3S_2_4.0, respectively.

4.3.5. Preparation of Ni_3S_2-modified 3DIE for electrochemical tests

In order to make both sides of the electrodes independently addressable a small portion of the supporting scaffold was cut out using a razor blade. The hole in the supporting arm was then filled with epoxy and allowed to dry. This was done one side at a time, and the epoxy was allowed to fully dry in between to ensure the two sides of the electrode did not touch. For samples coated in the Ni_3S_2 catalyst, an additional Ni layer of nickel was electrodeposited onto the BCC lattice to serve as both the counter and reference electrode. Then stainless-steel foils were attached using conductive silver colloidal paint to act as contact points for the electrochemical testing. Finally, epoxy was used to seal the supporting scaffold, leaving only the interpenetrated part of the electrode exposed as the active area.

4.3.6. Electrochemical measurements

Electrochemical measurements were performed for as-prepared catalysts on the CHI 660D electrochemical workstation in a three-electrode configuration in a solution containing 1.0 M KOH and 0.33 M urea. The as-prepared catalysts served as the working electrode; carbon rod was selected as the counter electrode and Hg/HgO was used as the reference electrode. For each sample, CV was first performed in a potential window of 0 to 0.8 V versus Hg/HgO for 40 cycles at a scan rate of 10 mV s^{-1}, and then LSVs were collected at 1.0 mV s^{-1}. EIS measurements were performed at the different voltages, utilizing a frequency range from 100 kHz to 1 Hz, and an amplitude of 5 mV. The R_S and the R_{CT} were obtained from the Nyquist plots. All LSV data were 85% iR corrected based on EIS data. The overall water splitting test was performed at room temperature in a two-electrode configuration at various voltages. ECSA was determined by measuring the capacitive current associated with double-layer charging from the scan-rate dependence of CVs. Interpenetrated electrodes were tested in a two-electrode configuration on the CHI 660D electrochemical workstation. The kelvin lattice served as the working electrode and the BCC lattice as the working and counter electrode. CVs were conducted to stabilize the electrode with a potential window of 0.8 to 2.5 V for 40 cycles. LSVs were collected at 1.0 mV s^{-1} in a solution containing 1.0 M KOH and 0.33 M urea.

4.3.7. *In-situ* Raman spectroscopy

In-situ Raman spectra were collected using a Renishaw inVia Plus Raman microscope equipped with a 532 nm laser source. The spectral range was 100-2000 cm^{-1} with an exposure time of 120 s and one accumulation per spectrum. The laser

power was set to 10%, and a 50× long-working-distance objective was used. Electrochemical Raman measurements were conducted in a standard three-electrode configuration with a Pt wire as the counter electrode and a Hg/HgO electrode as the reference electrode. The electrolyte consisted of 1.0 M KOH with 0.33 M urea. Before data acquisition, the working electrode was stabilized at open circuit potential (OCP) for 3 min. Raman spectra were then sequentially collected at applied potentials ranging from 1.20 to 1.40 V vs. RHE in 0.05 V increments. At each potential, the system was held for 3 min prior to spectral acquisition to ensure stabilization.

4.3.8. Simulation

All periodic DFT calculations were carried out using the GPAW code, which implements the projector augmented wave (PAW) method on a real-space plane-wave grid.[32] The exchange-correlation energy was treated using the Perdew-Burke-Ernzerhof (PBE) functional within the generalized gradient approximation (GGA).[33] A plane-wave basis set with a kinetic energy cutoff of 600 eV was employed to represent the valence electrons. Spin-polarized calculations were performed using the Methfessel-Paxton smearing method with a width of 0.2 eV to improve convergence.

The Ni_3S_2 surface with an adsorbate was modeled using a slab generated from the heazlewoodite bulk phase (space group $R\bar{3}2$, COD ID: 9007640), as originally reported by Parise et al.[34] The (110) surface was constructed using the ASE surface builder with two atomic layers and approximately 30 Å of vacuum along the surface normal, followed by expansion to a 3 × 3 in-plane supercell. The resulting slab geometry was placed in a triclinic simulation cell defined by the lattice vectors a =

(18.09, 0.00, 0.00) Å, b = (-3.56, 10.78, 0.00) Å, and c = (0.00, 0.00, 66.08) Å, providing more than 30 Å of vacuum separation between periodically repeated slabs. The $Ni(OH)_2$ slab was built from the bulk structure provided in the CIF file[35] (space group P1, lattice parameters a = b = 3.341 Å, c = 4.396 Å, γ = 120°), corresponding to the layered brucite-type Ni(OH)2 phase. The (110) surface was constructed using the ASE surface builder. The slab was then expanded to a 3 × 3 × 1 supercell to reduce lateral interaction between periodically repeated images. GPAW calculations were performed in plane-wave mode, which employs three-dimensional periodic boundary conditions. Periodic boundary conditions were applied in the x and y directions, while the z direction was kept non-periodic. The Brillouin zone was sampled at the Γ point only. Geometry optimization was performed using the BFGS algorithm as implemented in the Atomic Simulation Environment (ASE)[36] until all residual forces were below 0.05 eV/Å. The final optimized structures were visualized by using the VESTA program.[37]

4.4 Results and discussion

4.4.1. Surface morphology and structural characterization

Ni_3S_2 catalysts were directly grown on nickel foam substrates via a one-step hydrothermal sulfurization process, with the sulfur precursor concentration varied to tune the extent of sulfur incorporation (**Figure 4.1a**). XRD patterns of the as-prepared samples are shown in **Figure 4.1b**. The control sample synthesized in the absence of sulfur precursor exhibits diffraction peaks characteristic of nickel hydroxide ($Ni(OH)_2$), consistent with the formation of a hydroxide phase under alkaline hydrothermal conditions. In contrast, all sulfurized samples display

diffraction peaks that can be indexed to the Ni_3S_2 phase, indicating successful conversion of the nickel substrate into crystalline nickel sulfide. Importantly, no additional impurity phases are detected across the entire sulfur precursor concentration range investigated, suggesting that the hydrothermal sulfurization process yields phase-pure Ni_3S_2 regardless of sulfur loading. The similarity in diffraction peak positions and relative intensities among the Ni_3S_2 samples further indicates that variation of sulfur precursor concentration does not induce significant changes in the bulk crystal structure.

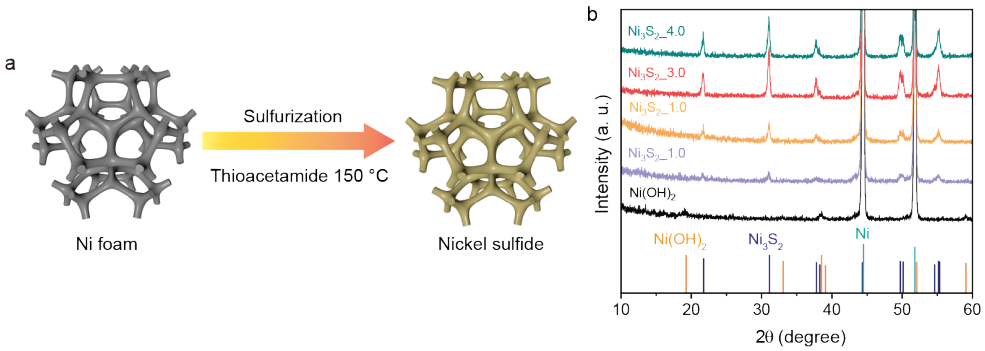

Figure 4.1. (a) Schematic illustration of the hydrothermal synthesis of Ni_3S_2. (b) X-ray diffraction patterns of $Ni(OH)_2$, Ni_3S_2_1.0, Ni_3S_2_2.0, Ni_3S_2_3.0 and Ni_3S_2_4.0. Standard diffraction patterns of $Ni(OH)_2$ (PDF# 14-0117), Ni_3S_2 (PDF# 44-0805) and metallic Ni (PDF# 04-0850) are added for reference.

The surface morphology of the catalysts was examined using SEM. As shown in **Figure 4.2 a-e**, both the control and sulfurized samples exhibit a uniformly roughened surface composed of interconnected nanoscale features covering the nickel foam substrate. The overall morphology remains largely consistent across the Ni_3S_2 series, despite variations in sulfur precursor concentration (**Table 4.1**), indicating that the sulfurization process primarily modifies the chemical

composition and electronic structure rather than inducing drastic morphological reconstruction. Energy-dispersive X-ray spectroscopy (EDS) elemental mapping was further employed to probe the spatial distribution of the elements. Representative EDS maps confirm the homogeneous distribution of nickel and sulfur across the catalyst surface for all sulfurized samples, with no evidence of localized sulfur-rich or sulfur-deficient regions. Quantitative EDS analysis (**Table 4.1**) reveals a progressive increase in sulfur content with increasing sulfur precursor concentration, approaching the stoichiometric composition of Ni_3S_2. The uniform elemental distribution observed across large surface areas suggests that the hydrothermal sulfurization process produces compositionally homogeneous Ni_3S_2 coatings, thereby minimizing structural or compositional heterogeneity that could otherwise complicate interpretation of electrochemical behavior.

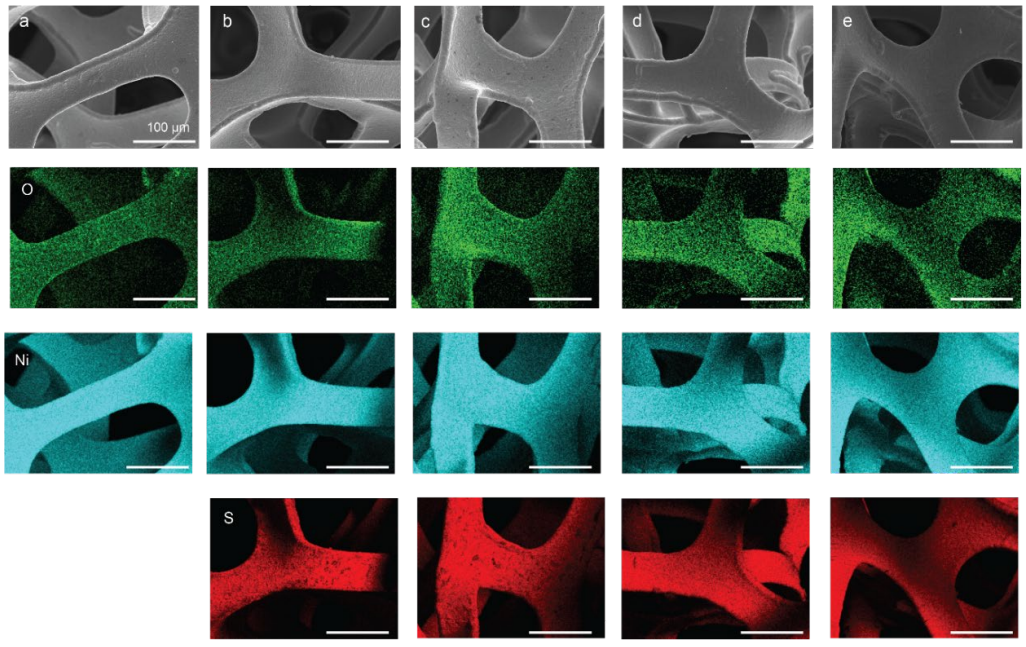

Figure 4.2. (a-e) SEM images of $Ni(OH)_2$, Ni_3S_2_1.0, Ni_3S_2_2.0, Ni_3S_2_3.0 and Ni_3S_2_4.0, along with corresponding elemental mappings for O, Ni, and S. Scale bars are 100 µm.

Table 4.1. Summary of the measured weight percentages and calculated atomic percentages of Ni, O, and S for the control and sulfurized samples.

Catalyst	Ni (wt %)	O (wt %)	S (wt %)	Ni (at %)	O (at %)	S (at %)
$Ni(OH)_2$	96.8	3.2	-	89.2	10.8	-
Ni_3S_2_1.0	78.7	1.1	20.2	65.7	3.4	30.9
Ni_3S_2_2.0	75.3	0.5	24.2	62.0	1.5	36.5
Ni_3S_2_3.0	73.2	1.4	25.4	58.6	4.1	37.2
Ni_3S_2_4.0	71.9	2.7	25.4	56.0	7.7	36.2

4.4.2 Electronic Structure and Valence-State Analysis

To elucidate the impact of sulfurization on the electronic structure of nickel centers and to quantitatively evaluate the extent of valence-state modulation, XPS was systematically employed to analyze the chemical states of Ni and S in the synthesized catalysts. Because Ni^{3+} species are widely recognized as the catalytically active sites for urea oxidation in alkaline media, particular emphasis was placed on accurately determining the Ni^{3+}/Ni^{2+} ratio using a rigorously constrained and internally consistent fitting protocol. In order to ensure the reliability of the extracted chemical-state information and to avoid artificial enhancement of fit quality through excessive peak splitting, all Ni 2p spectra were analyzed by simultaneously considering both the Ni $2p_{3/2}$ and Ni $2p_{1/2}$ regions under identical fitting constraints. **Figure 4.3** presents the high-resolution Ni 2p spectra of representative Ni_3S_2 samples together with the $Ni(OH)_2$ control. All spectra exhibit clearly resolved spin-orbit doublets corresponding to the Ni $2p_{3/2}$ and Ni $2p_{1/2}$ core levels, accompanied by characteristic shake-up satellite features typical

of nickel-based compounds. The spin-orbit doublets were fitted using a fixed energy separation and a fixed area ratio of 2:1 ($2p_{3/2}$:$2p_{1/2}$), consistent with theoretical degeneracy. The corresponding doublets were constrained to possess identical linewidths, and satellite peaks were incorporated following commonly accepted fitting practices. A consistent Shirley background subtraction method and identical fitting energy window were applied to all samples to ensure strict comparability across the dataset. Importantly, the number of fitting components was limited to the minimum chemically justified set required to reproduce the experimental spectra, and no additional peaks were introduced unless supported by distinct spectral features.

The deconvoluted Ni $2p_{3/2}$ region can be consistently resolved into two primary components centered at approximately 855.4 eV and 856.5 eV, which are assigned to Ni^{2+} and Ni^{3+} species, respectively, in accordance with previous studies on nickel-based hydroxides and sulfides.[38] Quantitative analysis of the electrochemically operated (spent) catalysts reveals that the Ni^{3+}/Ni^{2+} ratios derived from the Ni $2p_{3/2}$ region are 1.63, 1.92, 1.95, 3.69, and 3.20 for $Ni(OH)_2$, Ni_3S_2_1.0, Ni_3S_2_2.0, Ni_3S_2_3.0, and Ni_3S_2_4.0, respectively. Independent extraction of the Ni^{3+}/Ni^{2+} ratios from the Ni $2p_{1/2}$ region yields corresponding values of 0.64, 1.12, 1.21, 2.24, and 2.05 for the same sequence. Although the absolute values obtained from the $2p_{1/2}$ region are systematically lower, likely due to stronger satellite and background contributions in this region, the monotonic trend across the Ni_3S_2 series remains fully consistent with that observed from the $2p_{3/2}$ region, thereby confirming the robustness of the valence-state evolution. In the quantitative discussion throughout this chapter, the Ni^{3+}/Ni^{2+} ratios derived from the Ni $2p_{3/2}$

region are used because this peak exhibits stronger signal intensity and more clearly defined peak envelopes compared to the Ni $2p_{1/2}$ region, enabling more reliable numerical extraction.

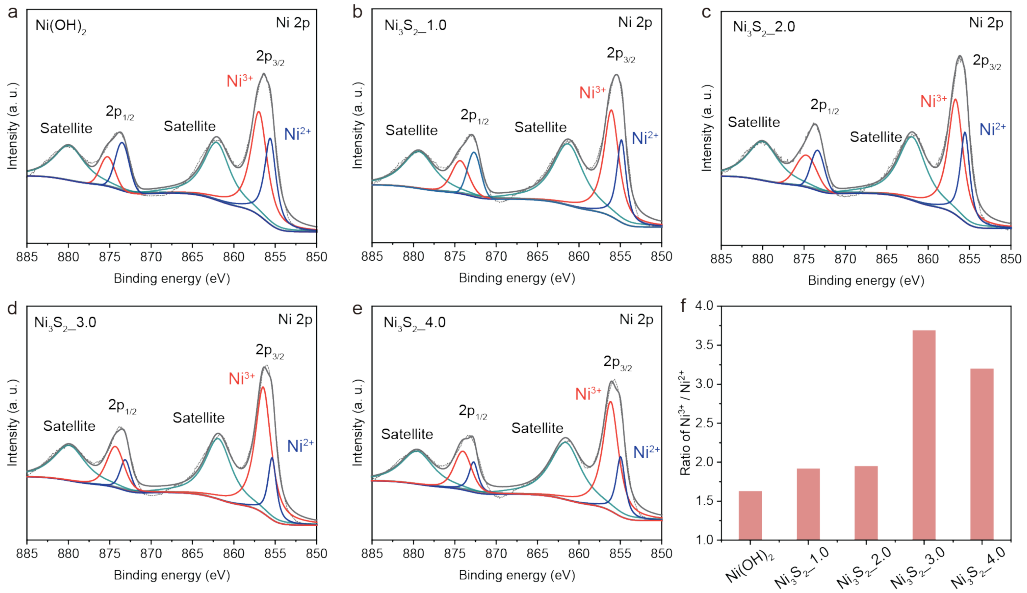

Figure 4.3. Ni 2p XPS spectra of spent catalysts: (a) $Ni(OH)_2$, (b) Ni_3S_2_1.0, (c) Ni_3S_2_2.0, (d) Ni_3S_2_3.0 and (e) Ni_3S_2_4.0. (f) Histogram showing the Ni^{3+}/Ni^{2+} ratio in the spent Ni_3S_2 samples and $Ni(OH)_2$. Quantitative analysis of the Ni^{3+}/Ni^{2+} ratios was performed using the Ni $2p_{3/2}$ peak due to its superior signal intensity and more clearly defined peak envelopes compared to the Ni $2p_{1/2}$ region.

To further strengthen the reliability of the XPS analysis and to evaluate the influence of electrochemical activation on the nickel valence states, additional Ni 2p measurements were performed on fresh (non-electrochemically activated) samples using exactly the same fitting parameters, background subtraction method, and constraints as those applied to the spent electrodes (**Figure 4.4**). For the fresh catalysts, the Ni^{3+}/Ni^{2+} ratios extracted from the Ni $2p_{3/2}$ region are 1.59, 1.81, 1.87,

3.41, and 3.06 for $Ni(OH)_2$, Ni_3S_2_1.0, Ni_3S_2_2.0, Ni_3S_2_3.0, and Ni_3S_2_4.0, respectively, while those derived from the Ni 2p1/2 region are 0.60, 0.91, 0.92, 1.88, and 1.70. Comparative analysis shows that the spent catalysts exhibit higher Ni^{3+} fractions relative to their fresh counterparts, which can be attributed to partial surface oxidation and reconstruction under alkaline UOR conditions. Importantly, despite this moderate increase in overall Ni^{3+} content after operation, the relative ordering of Ni^{3+} enrichment among the Ni_3S_2 series remains unchanged, indicating that the intrinsic differences in valence state established during synthesis persist under electrochemical conditions.

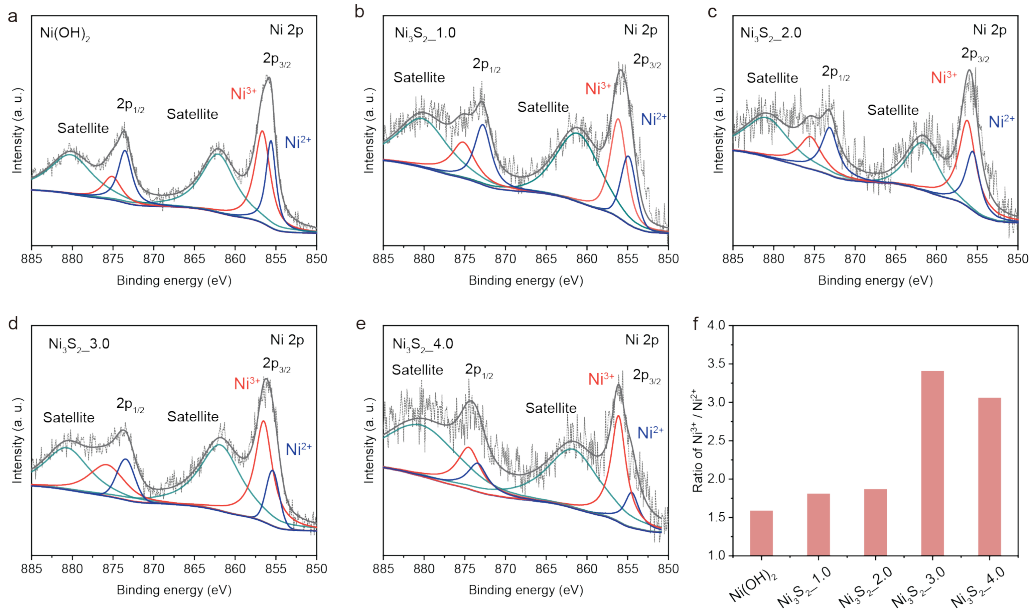

Figure 4.4. Ni 2p XPS spectra of fresh catalysts: (a) $Ni(OH)_2$, (b) Ni_3S_2_1.0, (c) Ni_3S_2_2.0, (d) Ni_3S_2_3.0 and (e) Ni_3S_2_4.0. (f) Histogram showing the Ni^{3+}/Ni^{2+} ratio in the spent Ni_3S_2 samples and $Ni(OH)_2$. Quantitative analysis of the Ni^{3+}/Ni^{2+} ratios was performed using the Ni $2p_{3/2}$ peak due to its superior signal intensity and more clearly defined peak envelopes compared to the Ni $2p_{1/2}$ region.

The electronic interaction between nickel and sulfur was further examined through high-resolution S 2p XPS analysis (**Figure 4.5**). In response to concerns regarding fitting reliability, the S 2p spectra were reprocessed using a rigorously constrained fitting protocol in which the S $2p_{3/2}$ and S $2p_{1/2}$ spin-orbit doublets were explicitly considered with a fixed area ratio of 2:1 and a consistent Shirley background applied across all samples. The dominant S 2p3/2 peaks for Ni_3S_2_1.0, Ni_3S_2_2.0, Ni_3S_2_3.0, and Ni_3S_2_4.0 are located at 161.81, 162.08, 162.46, and 162.32 eV, respectively. With increasing sulfur precursor concentration, the S 2p3/2 peak exhibits an overall positive shift toward higher binding energy, reaching a plateau at Ni_3S_2_3.0. This shift indicates a decrease in electron density around sulfur atoms and is consistent with the enrichment of Ni^{3+} species and the corresponding modulation of the local electronic structure. Surface elemental analysis further reveals that Ni_3S_2_3.0 possesses the highest sulfur content (37.2 at%), whereas further increasing the sulfur precursor to 4 mmol does not increase sulfur incorporation (36.2 at%) but instead leads to increased oxygen content. Because the Ni^{3+} population is sensitive to the local S/O coordination environment, this compositional change likely accounts for the decrease in the Ni^{3+}/Ni^{2+} ratio observed for Ni_3S_2_4.0 relative to Ni_3S_2_3.0.

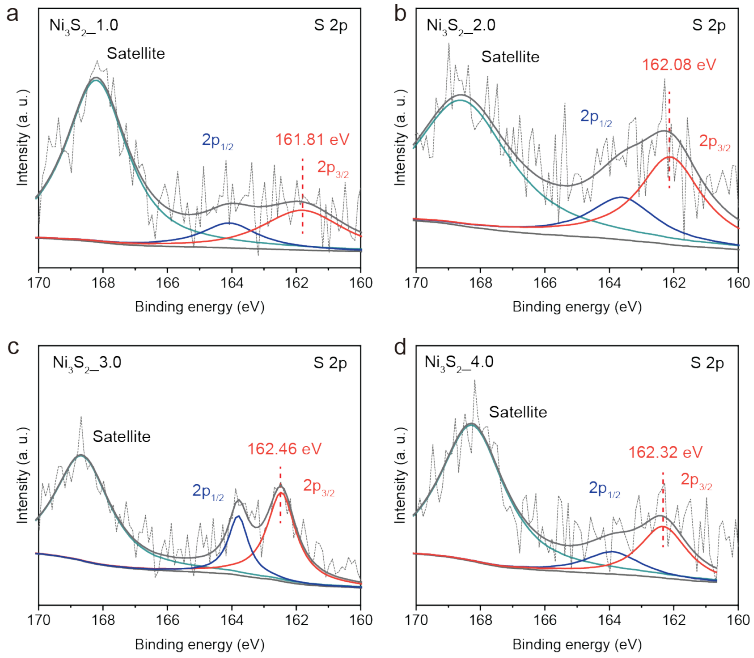

Figure 4.5. S 2p XPS spectra of (a) Ni_3S_2_1.0, (b) Ni_3S_2_2.0, (c) Ni_3S_2_3.0 and (d) Ni_3S_2_4.0.

4.4.3 Electrochemical performance

Building upon the established valence-state modulation discussed above, the electrocatalytic performance of the synthesized catalysts toward the UOR was systematically evaluated in alkaline electrolyte containing urea. All electrochemical measurements were conducted under identical conditions to ensure meaningful comparison and to isolate the effect of sulfur-enabled electronic structure modulation on catalytic activity. In addition to evaluating UOR activity, OER performance was also measured in 1.0 M KOH to provide a reference for assessing the reaction selectivity and catalytic behavior of the Ni-based catalysts.

Figure 4.6a and **b** present the linear sweep voltammetry curves of the Ni_3S_2 catalysts with varying sulfur precursor concentrations, together with the $Ni(OH)_2$ control, recorded in 1.0 M KOH and in 1.0 M KOH containing 0.33 M urea,

respectively. As shown in **Figure 4.6a**, the OER activity varies only slightly among the $Ni(OH)_2$ and Ni_3S_2 samples, with $Ni(OH)_2$ exhibiting the best performance under the tested conditions. In contrast, a pronounced difference is observed for the UOR activity (**Figure 4.6b**). The catalytic activity follows a clear trend as a function of sulfur precursor concentration, with the order of activity observed to be Ni_3S_2_3.0 > Ni_3S_2_4.0 > Ni_3S_2_2.0 ≈ Ni_3S_2_1.0 > $Ni(OH)_2$, indicating that sulfur incorporation significantly influences the UOR catalytic kinetics within the Ni_3S_2 framework. Compared with the $Ni(OH)_2$ sample, all Ni_3S_2 catalysts exhibit markedly enhanced UOR activity, as evidenced by lower onset potentials and higher current densities over the entire potential range. Among these samples, the Ni_3S_2_3.0 catalyst delivers the best catalytic performance. This optimized catalyst requires a potential of 1.361 V vs. RHE to reach a current density of 100 mA cm^{-2}, which is substantially lower than that required for the $Ni(OH)_2$ control. This result highlights the effectiveness of sulfur incorporation in tuning the electronic structure of nickel centers and demonstrates that sulfur-enabled valence-state engineering can significantly promote UOR activity in nickel sulfide catalysts.

To further compare the catalytic performance quantitatively, the potentials required to achieve representative current densities were extracted and summarized in **Figure 4.6c**. The observed performance trend closely mirrors the evolution of the Ni^{3+}/Ni^{2+} ratio determined from XPS analysis (**Section 4.4.2**), indicating that UOR activity is strongly correlated with the population of high-valence Ni^{3+} species rather than with bulk composition or surface morphology alone. This correlation suggests that sulfur incorporation plays a critical role in modulating the local electronic structure of nickel centers within the Ni_3S_2 framework, thereby

facilitating the formation of catalytically active Ni^{3+} species during electrochemical oxidation and enhancing the overall catalytic performance. In addition, a direct comparison between OER and UOR activities was performed using the optimized Ni_3S_2_3.0 catalyst, as shown in **Figure 4.6d**. When urea is introduced into the alkaline electrolyte, the anodic current increases sharply at significantly lower potentials compared to the OER process in pure 1.0 M KOH solution. The Ni_3S_2_3.0 catalyst achieves a current density of 100 mA cm^{-2} at only 1.361 V vs. RHE during UOR, whereas a substantially higher potential is required to reach the same current density for OER. This corresponds to an approximately 170 mV reduction in overpotential, demonstrating that the urea oxidation reaction is thermodynamically and kinetically more favorable than oxygen evolution on the Ni_3S_2 catalyst surface. The pronounced difference further highlights the effectiveness of coupling UOR with hydrogen production to reduce the overall energy consumption of electrolysis systems.

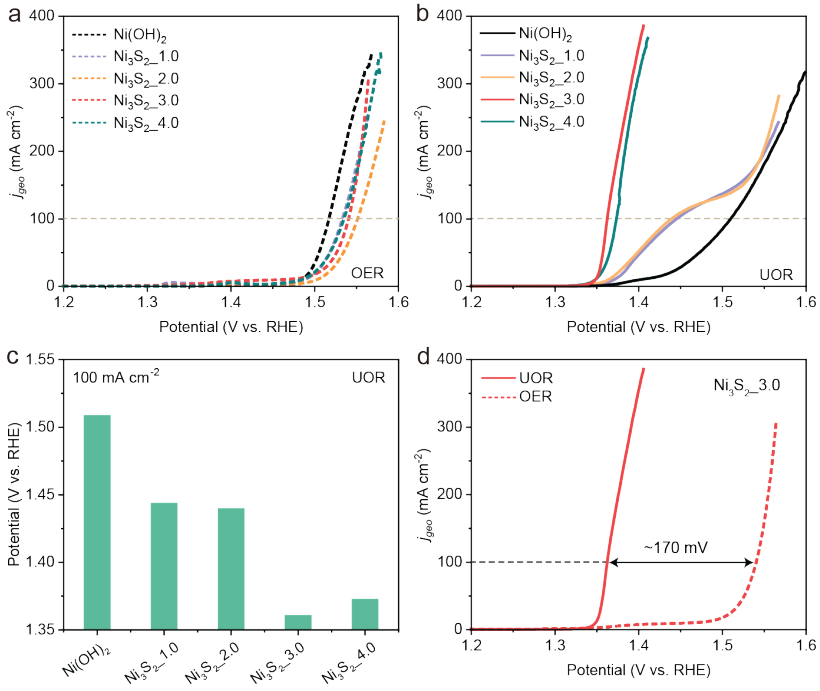

Figure 4.6. LSVs of $Ni(OH)_2$, Ni_3S_2_1.0, Ni_3S_2_2.0, Ni_3S_2_3.0 and Ni_3S_2_4.0 collected in (a) 1.0 M KOH and (b) 1.0 M KOH with 0.33 M urea, at a scan rate of 1.0 mV s^{-1}. (c) Potentials required for each sample to reach a current density of 100 mA cm^{-2}. (d) Comparison of LSVs for Ni_3S_2_3.0 collected in 1.0 M KOH (dash line) and in 1.0 M KOH with 0.33 M urea (solid line) at a scan rate of 1.0 mV s^{-1}.

To evaluate whether variations in electrochemically accessible surface area contribute to the observed catalytic performance differences, the electrochemically active surface area (ECSA) of the catalysts was studied from cyclic voltammetry conducted within a non-faradaic potential window. As shown in **Figure 4.7**, cyclic voltammograms were collected at scan rates ranging from 20 to 100 mV s^{-1} for each catalyst under both OER and UOR conditions. The capacitive current densities extracted from the positive potential region were plotted as a function of scan rate to determine the corresponding areal capacitances of the electrodes.

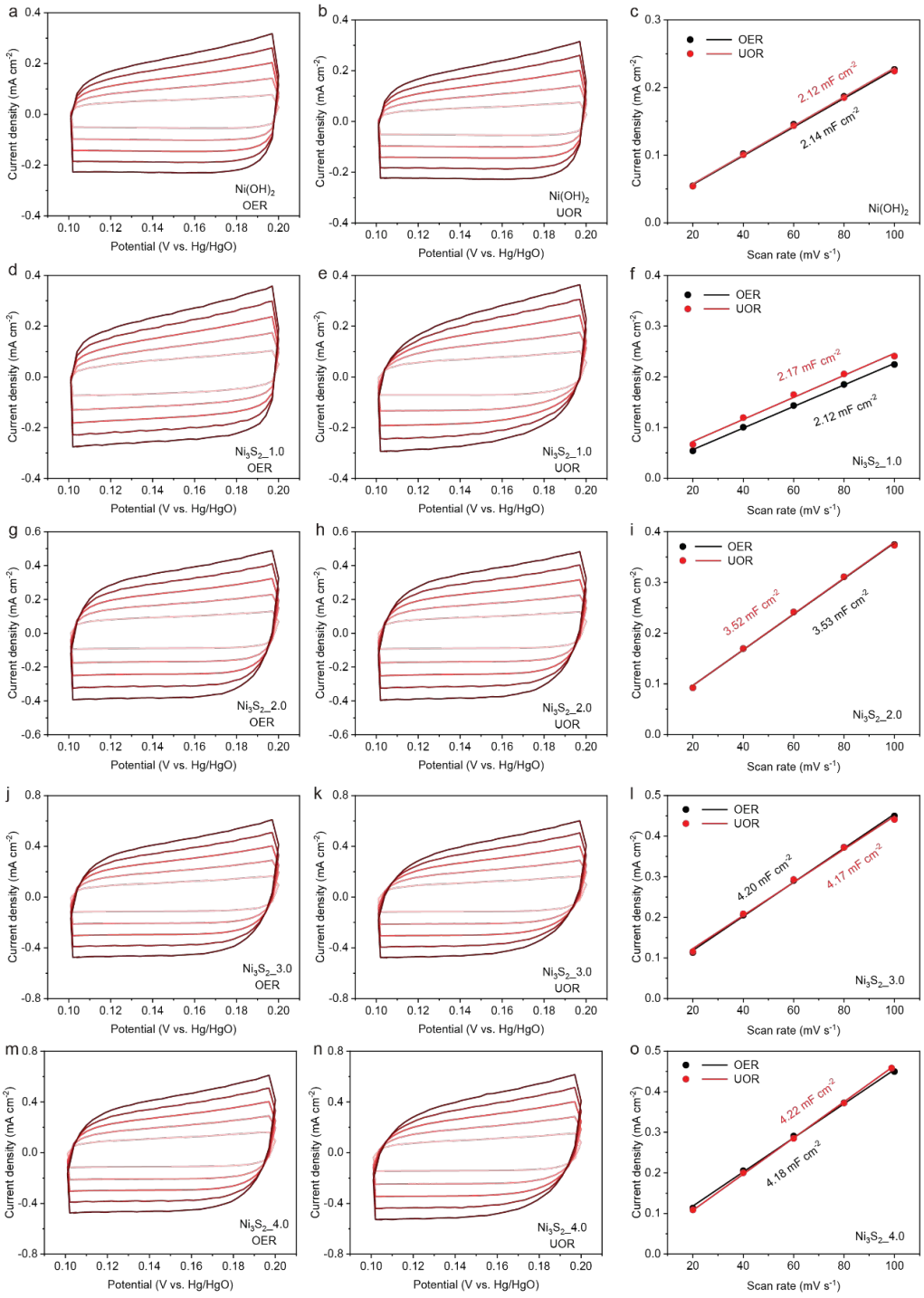

Figure 4.7. CV curves of each sample (a, b) $Ni(OH)_2$, (d, e) Ni_3S_2_1.0, (g, h) Ni_3S_2_2.0, (j, k) Ni_3S_2_3.0 and (m, n) Ni_3S_2_4.0 collected in 1.0 M KOH and 1.0 M KOH with 0.33 M urea at different scan rates from 20 to 100 mV s^{-1} at an interval of 20 mV s^{-1}, respectively. The data obtained in the positive potential are used to

determine the electrode's ECSA for OER and UOR, respectively. The geometric current density j_{geo} of each sample (c) $Ni(OH)_2$, (f) Ni_3S_2_1.0, (i) Ni_3S_2_2.0, (l) Ni_3S_2_3.0 and (o) Ni_3S_2_4.0 is plotted as a function of scan rate. The values in the figures are the areal capacitances of samples.

The calculated ECSA values are summarized in **Figure 4.8a**. The results indicate that the ECSA of the Ni_3S_2 catalysts increases progressively with increasing sulfur precursor concentration and eventually reaches a plateau for Ni_3S_2_3.0. In addition, the ECSA values obtained under OER and UOR conditions are nearly identical for each catalyst, indicating that the introduction of urea does not significantly alter the electrochemically accessible surface area of the electrodes.

To further determine whether the enhanced catalytic performance originates from surface area effects, the UOR polarization curves were normalized by the corresponding ECSA values, as shown in **Figure 4.8b**. Even after ECSA normalization, the Ni_3S_2_3.0 catalyst still exhibits the highest catalytic activity among the series. This result indicates that the superior UOR performance of Ni_3S_2_3.0 cannot be attributed solely to an increased electrochemically accessible surface area or a higher density of exposed active sites. Instead, the catalytic activity trend correlates more closely with the evolution of the Ni^{3+}/Ni^{2+} ratio determined from XPS analysis (**Section 4.4.2**), suggesting that sulfur incorporation plays a critical role in modulating the electronic structure of nickel centers and enhancing the intrinsic catalytic activity for the urea oxidation reaction.

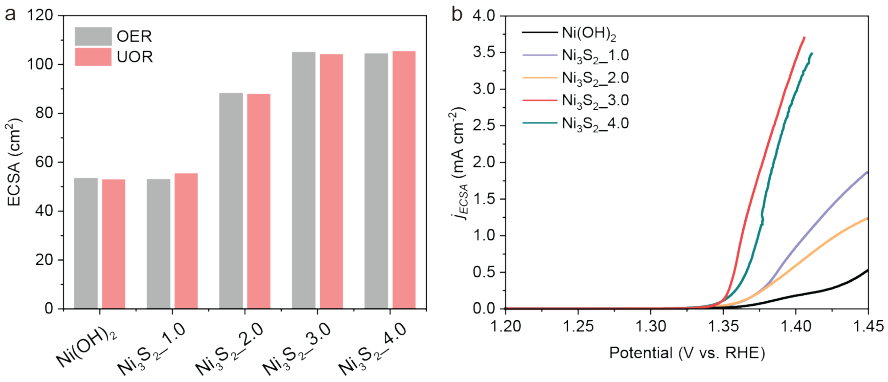

Figure 4.8. (a) The ECSA for OER and UOR of $Ni(OH)_2$, Ni_3S_2_1.0, Ni_3S_2_2.0, Ni_3S_2_3.0 and Ni_3S_2_4.0. (b) ECSA normalized LSV curves for UOR.

To further understand the origin of the ECSA variation, the surface morphologies of the catalysts were examined by SEM under higher magnification, as shown in **Figure 4.9**. The $Ni(OH)_2$ sample exhibits a relatively smooth surface morphology, whereas the sulfurized Ni_3S_2 catalysts display progressively rougher and more textured surfaces as the sulfur precursor concentration increases. This gradual evolution of surface roughness provides a larger electrochemically accessible interface between the catalyst and electrolyte, which is consistent with the increasing ECSA values extracted from the cyclic voltammetry measurements.

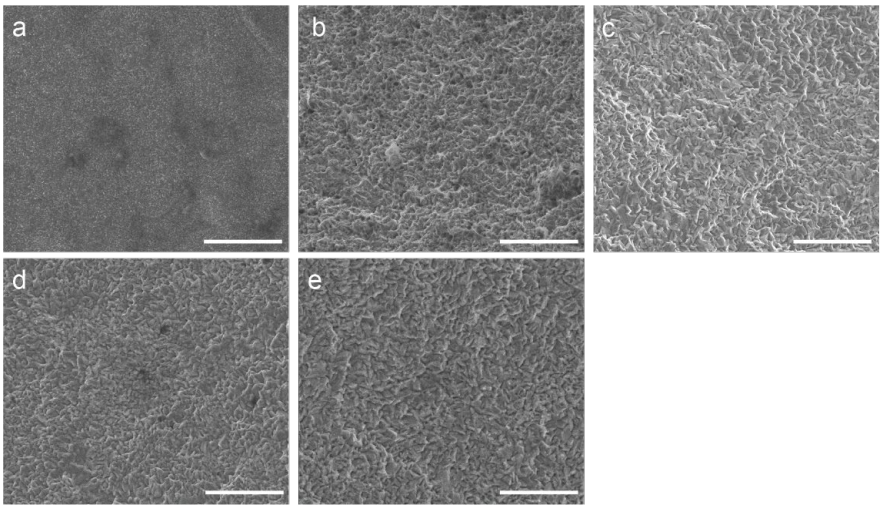

Figure 4.9. SEM images illustrating the surface morphology of (a) $Ni(OH)_2$, (b) Ni_3S_2_1.0, (c) Ni_3S_2_2.0, (d) Ni_3S_2_3.0, and (e) Ni_3S_2_4.0 under higher magnification. Scale bars are 4 μm.

Electrochemical impedance spectroscopy (EIS) was subsequently employed to probe the charge-transfer kinetics associated with the urea oxidation reaction on the different catalysts. Nyquist plots recorded at a representative UOR operating potential of 1.417 V vs. RHE are presented in **Figure 4.10a**. All Ni_3S_2 samples exhibit substantially smaller semicircle diameters than the $Ni(OH)_2$ control, indicating significantly reduced charge-transfer resistance and more favorable interfacial electron-transfer kinetics. To more clearly resolve the impedance features, an enlarged view of the high-frequency region is provided in **Figure 4.10b**. The Nyquist plots were fitted using an equivalent circuit model to extract the solution resistance (R_S) and charge-transfer resistance (R_{CT}) for each catalyst. The extracted resistance values are summarized in the histogram shown in **Figure 4.10c**. The results show that all catalysts possess comparable R_S, indicating similar electrode conductivity and electrolyte accessibility among the samples. In contrast,

pronounced differences are observed in the charge-transfer resistance. The Ni_3S_2_3.0 catalyst exhibits the lowest R_{CT} value among the series, demonstrating the most efficient charge-transfer kinetics during the urea oxidation process. In comparison, the $Ni(OH)_2$ control displays a significantly larger R_{CT} value, indicating sluggish interfacial electron transfer. The significantly reduced charge-transfer resistance observed for the Ni_3S_2 catalysts can be attributed to the conductive sulfide framework and the sulfur-enabled modulation of the nickel electronic structure. In particular, the Ni_3S_2_3.0 sample possesses the highest Ni^{3+}/Ni^{2+} ratio as revealed by XPS analysis, which promotes the formation of catalytically active Ni^{3+} species and facilitates electron transfer during the multi-electron urea oxidation reaction. Overall, the EIS results further support the conclusion that sulfur incorporation not only modifies the electronic structure of nickel centers but also significantly accelerates the interfacial charge-transfer kinetics, thereby contributing to the superior UOR catalytic performance observed for the Ni_3S_2_3.0 catalyst.

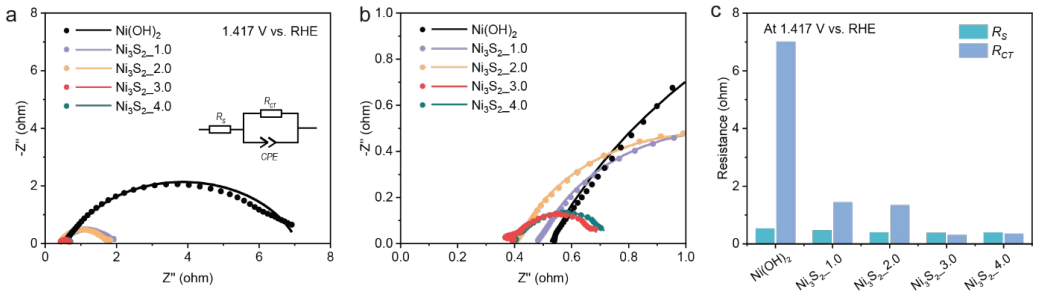

Figure 4.10. (a) Nyquist plots of the samples obtained in a frequency region ranging from 100 kHz to 1.0 Hz under an amplitude of 5 mV at 1.417 V vs. RHE. Circles represent experimental data. The solid lines represent fitted curves based on the

equivalent circuit model. (b): Enlarged view of the high frequency region. (c) Histograms illustrate the R_S and R_{CT} values across different samples.

The operational stability of the optimized Ni_3S_2 catalyst was further evaluated under prolonged electrolysis to assess its suitability for sustained UOR operation. Chronoamperometric measurements were conducted in 1.0 M KOH containing 0.33 M urea using a three-electrode configuration. As shown in **Figure 4.11a**, the Ni_3S_2_3.0 electrode exhibits excellent durability during continuous electrolysis at two representative anodic potentials. When operated at 1.35 V vs. RHE, corresponding to a geometric current density of approximately 15 mA cm^{-2}, the catalyst maintains a nearly constant current density throughout the 100 h testing period. At a higher operating potential of 1.37 V vs. RHE, corresponding to a current density of approximately 123 mA cm^{-2}, the Ni_3S_2_3.0 catalyst retains over 90% of its initial current density after prolonged electrolysis, indicating robust catalytic stability under both moderate and high reaction rates. To further examine possible structural changes after long-term electrolysis, XRD measurements were performed before and after the stability test, as shown in **Figure 4.11b**. The diffraction patterns remain essentially unchanged after 100 h of operation, indicating that the crystalline structure of Ni_3S_2 is well preserved during the electrochemical reaction. These results demonstrate that the Ni_3S_2 catalyst maintains both catalytic activity and structural integrity during prolonged UOR operation, highlighting the stability of the sulfur-stabilized Ni_3S_2 framework under sustained anodic conditions.

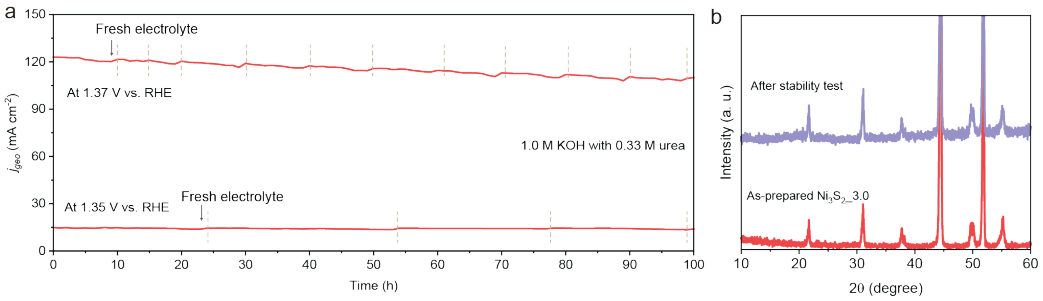

Figure 4.11. (a) Chronoamperometric stability test conducted at 1.35 and 1.37 V vs. RHE in 1.0 M KOH with 0.33 M urea using a three-electrode configuration. (b) XRD of Ni_3S_2_3.0 before and after stability test.

These electrochemical results establish a clear structure-property relationship between sulfur-regulated nickel valence-state modulation and UOR activity. The systematic enrichment of Ni^{3+} species through controlled sulfurization lowers the operating potential required for urea oxidation, accelerates charge-transfer kinetics, and enables long-term stable operation. These findings demonstrate that sulfur-enabled valence-state engineering constitutes an effective strategy for enhancing UOR performance and provides a direct link between electronic structure control and practical electrocatalytic functionality.

4.4.4 Mechanistic study

First, *in-situ* Raman spectroscopy was performed to investigate the potential-dependent surface evolution of Ni_3S_2 during the urea oxidation reaction. Raman spectra were collected for Ni_3S_2_1.0 and Ni_3S_2_3.0 in an electrolyte containing 1.0 M KOH and 0.33 M urea as the applied potential increased from open-circuit potential (OCP) to 1.40 V vs. RHE with a potential interval of 0.05 V. These two

catalysts were selected because they exhibit significantly different Ni^{3+}/Ni^{2+} ratios and UOR activities while maintaining the same Ni_3S_2 framework.

At OCP, both samples display characteristic Ni_3S_2 lattice vibrations at approximately 325 and 350 cm^{-1},[39] together with an intense Raman peak at 1005 cm^{-1} corresponding to adsorbed urea species,[40] confirming effective adsorption of urea molecules on the catalyst surface. Notably, the Ni_3S_2 lattice peaks remain visible throughout the entire potential range up to 1.40 V vs. RHE, indicating that the bulk Ni_3S_2 framework remains structurally stable under anodic polarization during UOR operation. Broad Raman features between 450 and 550 cm^{-1}, attributed to Ni^{2+}-O vibrations, are observed for both catalysts.[41] The relative intensity of these peaks indicates that Ni_3S_2_1.0 contains a higher proportion of Ni^{2+} species compared with Ni_3S_2_3.0, consistent with the XPS results discussed in **Section 4.4.2**. As the applied potential increases to approximately 1.35 V vs. RHE and above, two characteristic peaks at around 477 and 556 cm^{-1} emerge, corresponding to the bending and stretching modes of Ni^{3+}-O species in NiOOH.[42] The Ni^{3+}-O signal is considerably stronger for Ni_3S_2_1.0 than for Ni_3S_2_3.0, indicating that the initially present Ni^{2+} species undergo conversion to NiOOH under anodic conditions.

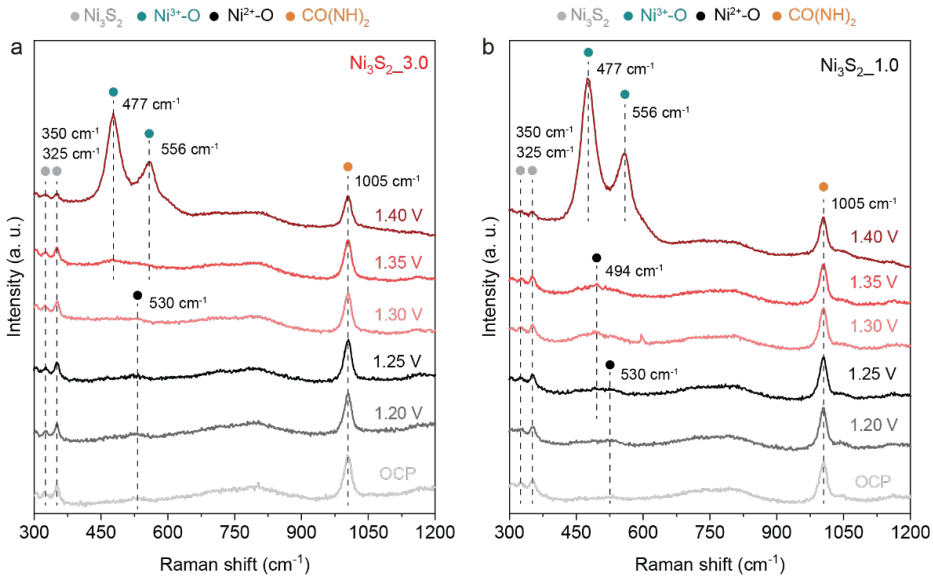

Figure 4.12. *In-situ* Raman spectra of (a) Ni_3S_2_3.0 and (b) Ni_3S_2_1.0 in the electrolyte containing 1.0 M KOH with 0.33 M urea.

Transmission electron microscopy (TEM) further confirms the structural stability of the catalyst after electrochemical operation. TEM images of the spent Ni_3S_2_3.0 catalyst reveal clear lattice fringes with an interplanar spacing of approximately 0.28 nm, corresponding to the (110) plane of crystalline Ni_3S_2. The preservation of these lattice features after UOR testing indicates that the crystalline Ni_3S_2 framework remains intact during electrochemical operation, consistent with the *in-situ* Raman observation that the sulfide lattice is maintained under anodic conditions.

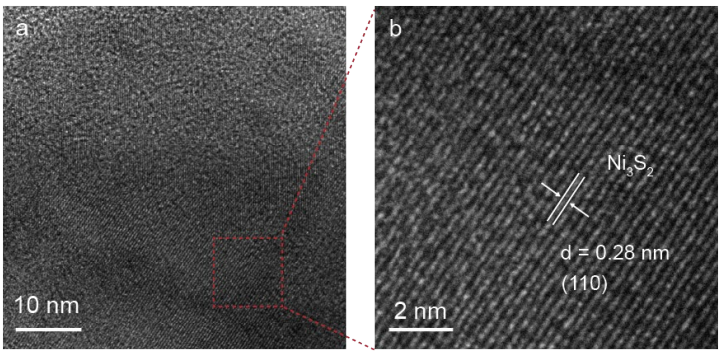

Figure 4.13. Lattice-resolved TEM image of the post-UOR Ni_3S_2_3.0 sample under different magnifications.

To provide quantitative mechanistic insight into the role of Ni^{3+} enrichment in enhancing urea oxidation activity, density functional theory (DFT) calculations were performed to explicitly examine how variations in the local electronic environment of Ni sites influence the activation barrier of the rate-determining step. In particular, the theoretical analysis was designed to complement experimental observations by directly evaluating the effect of increased Ni^{3+} content within the Ni_3S_2 framework. Following established mechanistic models for urea oxidation on nickel-based catalysts in alkaline media, the reaction pathway was considered to proceed through urea adsorption, subsequent C-N bond cleavage, and further oxidation steps leading to the formation of CO_2 and N_2.[43] (**Figure 4.14**) Among these elementary steps, cleavage of the urea C-N bond has been widely identified as the rate-determining step (RDS) and therefore constitutes the primary focus of the present calculations.

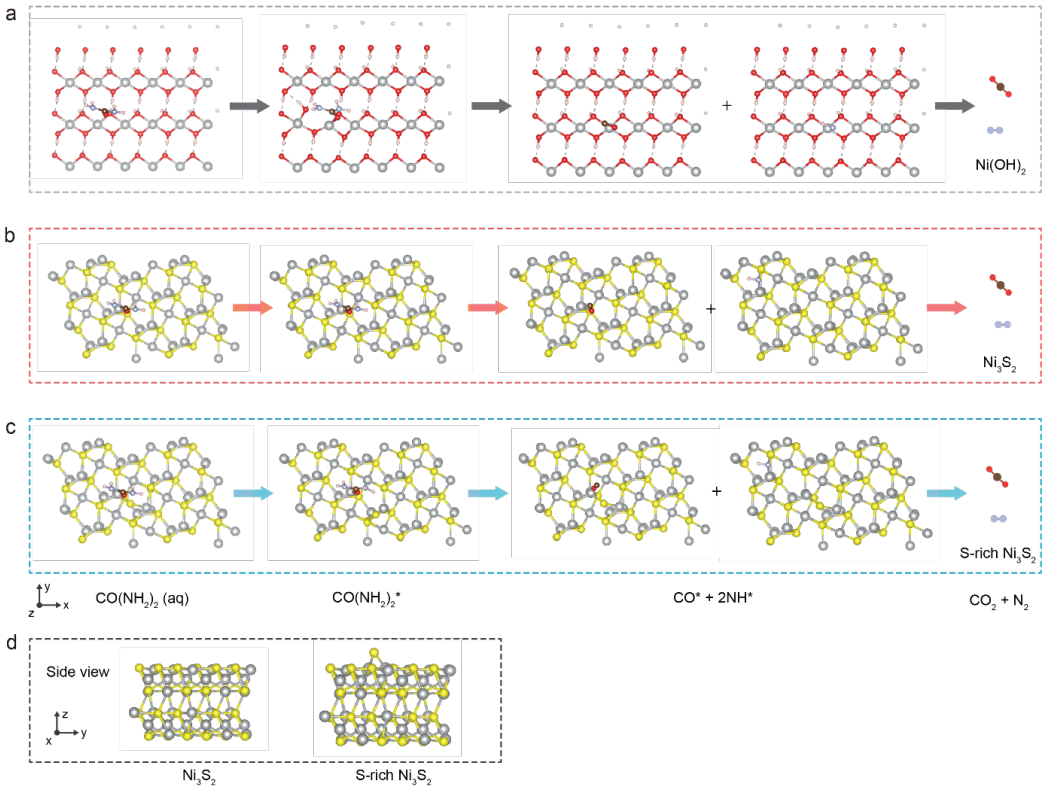

$$CO(NH_2)_2\,(aq) \rightarrow CO(NH_2)_2^* \qquad \textbf{Eqn. 4.1}$$

$$CO(NH_2)_2^* + 2OH^- \rightarrow CO^* + 2NH^* + 2H_2O\,(l) + 2e^- \qquad \textbf{Eqn. 4.2}$$

$$CO^* + 2NH^* + 4OH^- \qquad \textbf{Eqn. 4.3}$$

$$\rightarrow CO_2\,(g) + N_2\,(g) + 3H_2O\,(l) + 4e^-$$

Figure 4.14. Simulated reaction pathways for (a) $Ni(OH)_2$, (b) Ni_3S_2, (c) S-rich Ni_3S_2, (d) side view of Ni_3S_2 and S-rich Ni_3S_2 and the corresponding reactions.[43]

DFT calculations were first conducted on pristine Ni_3S_2 and $Ni(OH)_2$ surfaces to compare the intrinsic reaction energetics of sulfide- and hydroxide-based catalysts. As summarized in **Figure 4.15**, Ni_3S_2 exhibits a substantially lower activation barrier for the C-N bond cleavage step (ΔG = 3.06 eV) compared to $Ni(OH)_2$ (ΔG = 7.40 eV), highlighting the inherent advantage of nickel sulfide in facilitating urea oxidation. While this comparison establishes the superior intrinsic

activity of Ni_3S_2 relative to $Ni(OH)_2$, it does not explicitly capture the effect of incremental changes in Ni^{3+} content within the Ni_3S_2 framework. To more directly probe the influence of Ni^{3+} enrichment, an S-rich Ni_3S_2 surface model was constructed by introducing an additional sulfur atom at the catalyst surface to mimic a locally nonstoichiometric environment. This model reflects experimental conditions under which increased sulfur incorporation is associated with a higher fraction of Ni^{3+} species, as evidenced by XPS analysis. The introduction of excess surface sulfur modifies the local coordination environment of surface Ni atoms, leading to an elevated nickel oxidation state and altered electronic structure. The calculated reaction energy profiles reveal that the S-rich Ni_3S_2 surface exhibits a further reduction in the activation barrier for the C-N bond cleavage step, with a ΔG value of 2.58 eV. This barrier is notably lower than that of pristine Ni_3S_2 (3.06 eV) and dramatically reduced relative to $Ni(OH)_2$ (7.40 eV). The progressive decrease in activation barrier from $Ni(OH)_2$ to Ni_3S_2 and further to S-rich Ni_3S_2 establishes a clear theoretical trend that directly correlates increased Ni^{3+} content with facilitated urea activation.

Figure 4.15b summarizes the Gibbs free energy barriers associated with the rate-determining step for the three catalyst models. The substantial reduction in the C-N bond cleavage barrier on the S-rich Ni_3S_2 surface provides quantitative theoretical support for the experimentally observed enhancement in UOR activity with increasing Ni^{3+} fraction. This result demonstrates that Ni^{3+} enrichment does not merely alter adsorption energetics but directly lowers the kinetic bottleneck governing the overall reaction rate.

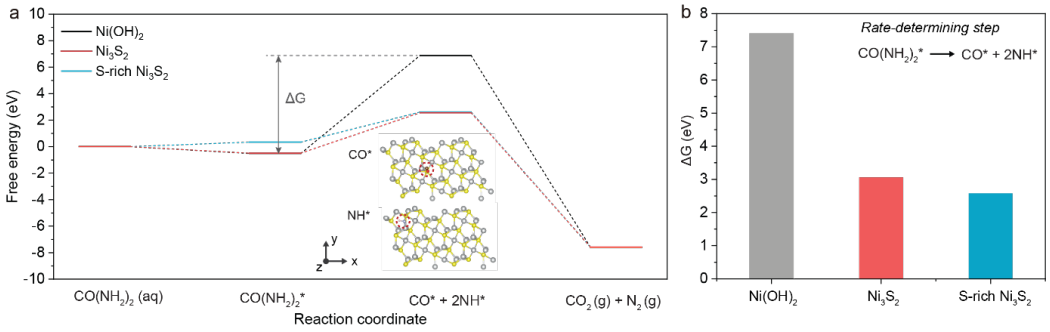

Figure 4.15. (a) The calculated reaction energy diagram of $Ni(OH)_2$, Ni_3S_2, and S-rich Ni_3S_2 for UOR. Inset image: the simulated profile for the rate-determining step: the formation of CO* and NH* intermediates on Ni_3S_2 catalyst. (b) The Gibbs free energy barrier for the rate-determining step of $Ni(OH)_2$, Ni_3S_2, and S-rich Ni_3S_2. The gray, yellow, red, brown, light blue and pink spheres represent Ni, S, O, C, N and H, respectively.

In conclusion, the DFT results provide strong theoretical support for the experimental findings presented in **Sections 4.4.2 and 4.4.3**. By intrinsically enriching Ni^{3+} species within the Ni_3S_2 framework, the energetic barrier for the rate-determining C-N bond cleavage step is effectively reduced, leading to accelerated UOR kinetics and improved catalytic performance. These mechanistic insights confirm that valence-state engineering operates at the fundamental reaction level, establishing a direct link between electronic structure modulation and enhanced urea oxidation activity.

4.5 Device-level performance of the interpenetrating electrode architecture

To further evaluate the practical applicability of the valence-state-engineered Ni_3S_2 catalyst under system-relevant conditions, the catalyst was integrated into a three-dimensional (3D) printed interpenetrating electrode device coupled with a

flow-cell configuration. This device-level design aims to enhance mass transport, shorten ion diffusion pathways, and enable continuous electrochemical operation, thereby bridging catalyst-level performance with realistic device operation. Each interpenetrating device consists of two independently addressable electrodes constructed from distinct but intertwined lattice architectures. Specifically, the device is composed of repeating units of a body-centered cubic (BCC) lattice interpenetrated with repeating units of a Kelvin cell (KC) lattice, as schematically illustrated in **Figures 4.16a** and **4.16b**. The interpenetrating structures were first fabricated via 3D printing using a commercially available plant-based resin (Elegoo), followed by electroless nickel plating to render the frameworks electrically conductive. Subsequently, the Ni_3S_2 catalyst was grown directly on the nickel-plated framework using the same hydrothermal sulfurization method described in the Experimental Section. After catalyst synthesis, the mechanical supports were selectively removed to yield two individually addressable electrodes.

In the final device configuration, nickel was electrodeposited onto the BCC lattice to serve as the cathode, while the KC lattice remained coated with the Ni_3S_2 catalyst to function as the anode. Stainless steel leads were attached to each electrode, and the entire device was sealed in epoxy, leaving only the lattice surfaces exposed as the ion-accessible region, as shown in **Figure 4.16c**. This interpenetrating configuration significantly reduces the distance between the anode and cathode, thereby shortening ion diffusion paths. As demonstrated in previous studies, such an architecture effectively enhances ion diffusion kinetics and mitigates concentration inhomogeneity within electrochemical devices. To assess the impact of the interpenetrating architecture on electrochemical performance,

devices constructed in the interpenetrated configuration were compared with control devices fabricated using separated electrodes, in which the KC and BCC lattices were printed individually and assembled without interpenetration. LSV measurements were first conducted in a beaker cell containing 1.0 M KOH with 0.33 M urea. As shown in Figure 4d, the interpenetrated device exhibits markedly enhanced activity relative to the separated-electrode configuration. At a cell voltage of 1.86 V, the interpenetrated device delivers a current density of 100 mA cm^{-2}, whereas the separated electrodes reach only 27.5 mA cm^{-2} under identical conditions. This performance disparity becomes increasingly pronounced at higher potentials, underscoring the critical role of improved mass transfer enabled by the reduced inter-electrode spacing in the interpenetrating architecture.

The device performance was further evaluated in a home-built flow cell, where continuous electrolyte flow provides additional enhancement of mass transport. Compared to operation in the beaker cell, the current–voltage response of the interpenetrating device shifts markedly toward lower potentials in the flow-cell configuration, as shown in **Figure 4.16e**. In the presence of urea, the interpenetrated Ni_3S_2_3.0//Ni device achieves a current density of 400 mA cm^{-2} at a cell voltage of 2.0 V. In contrast, under identical conditions but in the absence of urea, the OER current reaches only 162 mA cm^{-2} at the same voltage. This substantial difference in current density indicates that the measured current in the urea-containing electrolyte predominantly arises from urea oxidation, highlighting the advantage of UOR in reducing the effective anodic overpotential.

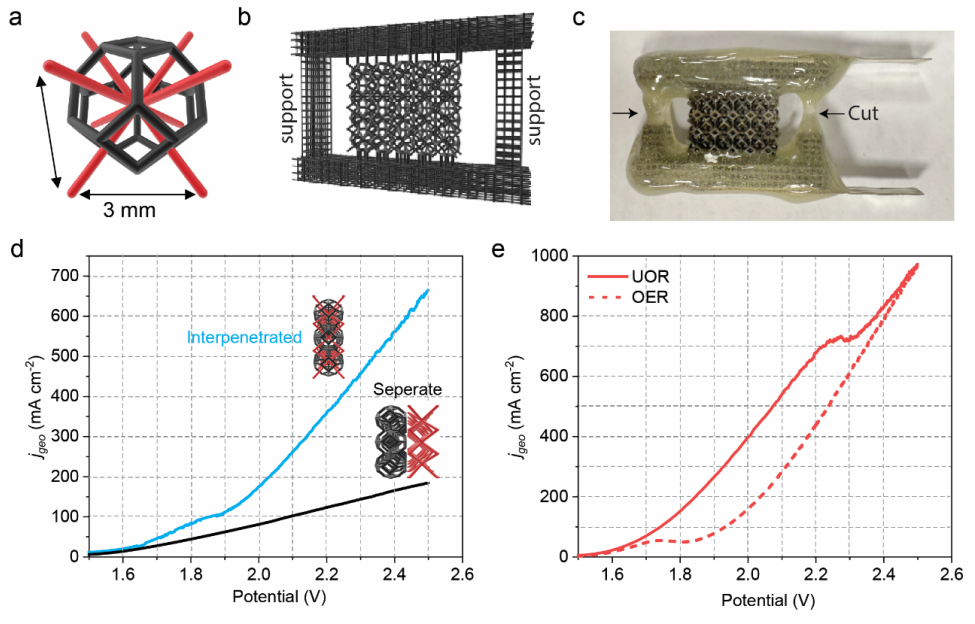

Figure 4.16. (a) Schematic illustration of a repeating unit in the interpenetrated structure. (b) Schematic illustration of an interpenetrated device. (c) Optical image of Ni_3S_2_3.0//Ni interpenetrated device. (d) LSVs of devices made of separated electrodes vs. interpenetrated electrodes collected in a beaker cell. (e) LSVs of the Ni_3S_2_3.0//Ni interpenetrated device collected in a home-built flow cell in 1.0 M KOH (dash line) and in 1.0 M KOH with 0.33 M urea (solid line) at a scan rate of 1.0 mV s^{-1}.

4.6 Conclusion

In this chapter, the UOR was systematically investigated as an alternative anodic process to replace the OER for energy-efficient hydrogen production. Motivated by the intrinsically high thermodynamic potential required for OER, this work demonstrates that reaction-level substitution provides an effective strategy to reduce anodic energy consumption while simultaneously enabling the treatment of urea-rich wastewater. Through controlled hydrothermal sulfurization, a valence-

state engineering strategy was developed to intrinsically enrich Ni^{3+} species within a conductive Ni_3S_2 framework. Comprehensive structural and spectroscopic characterizations confirmed that tuning the sulfur precursor concentration enables reproducible modulation of the Ni^{3+}/Ni^{2+} ratio without inducing significant changes in morphology or crystal structure. Electrochemical measurements revealed a clear correlation between Ni^{3+} enrichment and enhanced UOR activity, manifested by reduced operating potentials, accelerated charge-transfer kinetics, and improved long-term stability. DFT calculations further provided quantitative mechanistic insight, demonstrating that increased Ni^{3+} content lowers the activation barrier of the rate-determining C-N bond cleavage step, thereby establishing a direct structure-energetics-activity relationship.

Beyond catalyst-level performance, the Ni_3S_2 catalyst was successfully integrated into a 3D printed interpenetrating electrode architecture and evaluated under flow-cell operation. Device-level measurements demonstrated that the intrinsic catalytic advantages of UOR and Ni^{3+}-enriched Ni_3S_2 are preserved under continuous operation and enhanced mass-transport conditions. The interpenetrating architecture significantly improves ion transport and enables high current densities at reduced cell voltages, validating the practical relevance of combining reaction-level substitution with architecture-driven transport optimization.

This chapter completes critical progression in this thesis, advancing from interfacial bubble management (Chapter 2) and electrode architecture engineering (Chapter 3) to reaction-level energy optimization. By integrating valence-state-controlled catalyst design with device-level engineering, this work demonstrates a viable pathway toward energy-efficient hydrogen production coupled with

wastewater remediation, providing important insights for the development of next-generation electrochemical energy systems.

References

1. Zhu, J.; Hu, L.; Zhao, P.; Lee, L. Y. S.; Wong, K.-Y., *Chem. Rev.* **2020,** *120* (2), 851-918.

2. Kou, T.; Wang, S.; Li, Y., *ACS Mater. Lett.* **2021,** *3* (2), 224-234.

3. Ren, Q.; Feng, L.; Ye, C.; Xue, X.; Lin, D.; Eisenberg, S.; Kou, T.; Duoss, E. B.; Zhu, C.; Li, Y., *Adv. Energy Mater.* **2023,** *13* (39), 2302073.

4. Ren, Q.; Feng, L.; Tran, C.; Eisenberg, S.; Xue, X.; Pinongcos, A.; Duoss, E. B.; Zhu, C.; Li, Y., *ACS Mater. Lett.* **2024,** *6* (8), 3705-3712.

5. Ren, Q.; Tran, C.; Zhang, K.; Zhu, C.; Li, Y., *Nanoscale* **2025,** *17* (7), 3600-3615.

6. Wang, X.; Zhong, H.; Xi, S.; Lee, W. S. V.; Xue, J., *Adv. Mater.* **2022,** *34* (50), 2107956.

7. Gao, L.; Cui, X.; Sewell, C. D.; Li, J.; Lin, Z., *Chem. Soc. Rev.* **2021,** *50* (15), 8428-8469.

8. Chen, F.-Y.; Wu, Z.-Y.; Adler, Z.; Wang, H., *Joule* **2021,** *5* (7), 1704-1731.

9. Xu, S.; Ruan, X.; Ganesan, M.; Wu, J.; Ravi, S. K.; Cui, X., *Adv. Funct. Mater.* **2024,** *34* (18), 2313309.

10. Gao, X.; Zhang, S.; Wang, P.; Jaroniec, M.; Zheng, Y.; Qiao, S.-Z., *Chem. Soc. Rev.* **2024,** *53* (3), 1552-1591.

11. Fei, L.; Sun, H.; Xu, X.; Li, Y.; Ran, R.; Zhou, W.; Shao, Z., *Chem. Eng. J.* **2023,** *471*, 144660.

12. Li, J.; Zhang, J.; Yang, J.-H., *Int. J. Hydrogen Energy* **2022,** *47* (12), 7693-7712.

13. Paygozar, S.; Sabour Rouh Aghdam, A.; Hassanizadeh, E.; Andaveh, R.; Barati Darband, G., *Int. J. Hydrogen Energy* **2023,** *48* (20), 7219-7259.

14. Yang, K.; Hao, L.; Hou, Y.; Zhang, J.; Yang, J.-H., *Int. J. Hydrogen Energy* **2024,** *51*, 966-981.

15. Gao, X.; Bai, X.; Wang, P.; Jiao, Y.; Davey, K.; Zheng, Y.; Qiao, S.-Z., *Nat. Commun.* **2023,** *14* (1), 5842.

16. Huang, C.-J.; Xu, H.-M.; Shuai, T.-Y.; Zhan, Q.-N.; Zhang, Z.-J.; Li, G.-R., *Small* **2023,** *19* (45), 2301130.

17. Sun, H.; Song, S., *Small* **2024,** *20* (33), 2401343.

18. Ghosh, S.; Bagchi, D.; Mondal, I.; Sontheimer, T.; Jagadeesh, R. V.; Menezes, P. W., *Adv. Energy Mater.* **2024,** *14* (22), 2400696.

19. Kou, T.; Smart, T.; Yao, B.; Chen, I.; Thota, D.; Ping, Y.; Li, Y., *Adv. Energy Mater.* **2018,** *8* (19), 1703538.

20. Liu, M.; Jiao, Y.; Zhan, S.; Wang, H., *Catal. Today* **2020,** *355*, 596-601.

21. Zhang, Y.; Guo, H.; Song, M.; Sun, L.; Song, R., *J. Mater. Chem. A* **2023,** *11* (7), 3584-3593.

22. Ge, W.; Lin, L.; Wang, S.-Q.; Wang, Y.; Ma, X.; An, Q.; Zhao, L., *J. Mater. Chem. A* **2023,** *11* (28), 15100-15121.

23. Wang, H.; Zheng, X.; Fang, L.; Lu, S., *ChemElectroChem* **2023,** *10* (13), e202300138.

24. Xiao, Z.; Qian, Y.; Tan, T.; Lu, H.; Liu, C.; Wang, B.; Zhang, Q.; Sarwar, M. T.; Gao, R.; Tang, A.; Yang, H., *J. Mater. Chem. A* **2023,** *11* (1), 259-267.

25. Zhu, Y.; Liu, C.; Cui, S.; Lu, Z.; Ye, J.; Wen, Y.; Shi, W.; Huang, X.; Xue, L.; Bian, J.; Li, Y.; Xu, Y.; Zhang, B., *Adv. Mater.* **2023,** *35* (24), 2301549.

26. Guo, P.; Cao, S.; Huang, W.; Lu, X.; Chen, W.; Zhang, Y.; Wang, Y.; Xin, X.; Zou, R.; Liu, S.; Li, X., *Adv. Mater.* **2024,** *36* (18), 2311766.

27. Zhan, G.; Hu, L.; Li, H.; Dai, J.; Zhao, L.; Zheng, Q.; Zou, X.; Shi, Y.; Wang, J.; Hou, W.; Yao, Y.; Zhang, L., *Nat. Commun.* **2024,** *15* (1), 5918.

28. Zhou, S.; Lv, S.; Shi, J.; Zhang, L.; Li, J.; Cai, W., *Chem. Eng. J.* **2024,** *484*, 149706.

29. Zhu, D.; Zhang, H.; Miao, J.; Hu, F.; Wang, L.; Tang, Y.; Qiao, M.; Guo, C., *J. Mater. Chem. A* **2022,** *10* (7), 3296-3313.

30. Wang, L.; Zhu, Y.; Wen, Y.; Li, S.; Cui, C.; Ni, F.; Liu, Y.; Lin, H.; Li, Y.; Peng, H.; Zhang, B., *Angew. Chem., Int. Ed.* **2021,** *60* (19), 10577-10582.

31. Liu, S.; Feng, J.; Bian, X.; Liu, J.; Xu, H.; An, Y., *Energy Environ. Sci.* **2017**, 10 (5), 1222-1233.

32. Mortensen, J. J. r.; Larsen, A. H.; Kuisma, M.; Ivanov, A. V.; Taghizadeh, A.; Peterson, A.; Haldar, A.; Dohn, A. O.; SchÃ¤fer, C.; JÃ¸rnsson, E. Ã. r.; Hermes, E. D.; Nilsson, F. A.; Kastlunger, G.; Levi, G.; JÃ¸rnsson, H.; HÃ¤kkinen, H.; Fojt, J.; Kangsabanik, J.; SÃ¸dequist, J.; LehtomÃ¤ki, J.; Heske, J.; Enkovaara, J.; Winther, K. T. s.; Dulak, M.; Melander, M. M.; Ovesen, M.; Louhivuori, M.; Walter, M.; Gjerding, M.; Lopez-Acevedo, O.; Erhart, P.; Warmbier, R.; WÃ¤rdemann, R.; Kaappa, S.; Latini, S.; Boland, T. M.; Bligaard, T.; Skovhus, T. r.; Susi, T.; Maxson, T.; Rossi, T.; Chen, X.; Schmerwitz, Y. L. A.; SchiÃ¸tz, J.; Olsen, T.; Jacobsen, K. W.; Thygesen, K. S., *J. Chem. Phys.* **2024,** *160* (9), 092503.

33. Perdew, J. P.; Burke, K.; Ernzerhof, M., *Phys. Rev. Lett.* **1996,** *77* (18), 3865-3868.

34. Structure of hazelwoodite (Ni_3S_2). *Structural Science* **1980**, *36* (5) 1179-1180

35. LBNL Materials Project (2020). Materials Data on $Ni(OH)_2$ by Materials Project.

36. Hjorth Larsen, A.; JÃ¸rgen Mortensen, J.; Blomqvist, J.; Castelli, I. E.; Christensen, R.; DuÅak, M.; Friis, J.; Groves, M. N.; Hammer, B. r.; Hargus, C.; Hermes, E. D.; Jennings, P. C.; Bjerre Jensen, P.; Kermode, J.; Kitchin, J. R.; Leonhard Kolsbjerg, E.; Kubal, J.; Kaasbjerg, K.; Lysgaard, S.; Bergmann Maronsson, J.; Maxson, T.; Olsen, T.; Pastewka, L.; Peterson, A.; Rostgaard, C.; SchiÃ¸tz, J.; SchÃtt, O.; Strange, M.; Thygesen, K. S.; Vegge, T.; Vilhelmsen, L.; Walter, M.; Zeng, Z.; Jacobsen, K. W., *Journal of Physics: Condens. Matter* **2017,** *29* (27), 273002.

37. Momma, K.; Izumi, F., *J. Appl. Crystallogr.* **2011,** *44* (6), 1272-1276.

38. Kou, T.; Chen, M.; Wu, F.; Smart, T. J.; Wang, S.; Wu, Y.; Zhang, Y.; Li, S.; Lall, S.; Zhang, Z.; Liu, Y.-S.; Guo, J.; Wang, G.; Ping, Y.; Li, Y., *Nat. Commun.* **2020,** *11* (1), 590.

39. Cheng, Z.; Abernathy, H.; Liu, M., *J. Phys. Chem. C*, **2007**, 111, 17997-18000.

40. Kwon, Y. H.; Yang, X.; Wu, Z.; Fan, Z.; Xu, W.,; Jon, C. M., *J. Phys. Chem. C*, 2022, 126, 12492-12499.

41. Louie, M. W.,; Bell, A. T., *J. Am. Chem. Soc.*, 2013, 135, 12329-12337.

42. Bai, L.; Lee, S.,; Hu, X., *Angew. Chem., Int. Ed.*, 2021, 60, 3095-3103.

43. Cai, M.; Zhu, Q.; Wang, X.; Shao, Z.; Yao, L.; Zeng, H.; Wu, X.; Chen, J.; Huang, K.; Feng, S., *Adv. Mater.* **2023,** *35* (7), 2209338.

Chapter 5

Conclusion and outlook

This dissertation focused on several challenges that limit high-rate alkaline water splitting, including gas bubble accumulation, inefficient ion transport, and the slow kinetics of the anodic reaction. The work presented here shows that improving electrolyzer performance requires more than developing catalysts with high intrinsic activity. Electrode surface properties, three-dimensional structures, transport distance, and reaction pathways all play important roles, especially at high current densities.

In Chapter 2, nanocone-modified nickel electrodes were developed to improve gas bubble removal during the reaction. Compared with unmodified nickel surfaces, the nanocone-modified electrodes showed lower bubble adhesion, faster bubble detachment, and smaller bubble departure size. These changes helped reduce bubble coverage on the electrode surface and maintain more available reaction sites during gas evolution. The nanocone structure was applied to nickel foil, nickel foam, and 3D-printed nickel lattices, suggesting that this surface modification can be used on different types of electrode substrates and architectures.

In Chapter 3, an interpenetrating gyroid electrode was designed to reduce the ion-transport distance between the anode and cathode and maintaing open channel for bubble transport. Compared with conventional separated three-dimensional electrodes, the interpenetrating structure decreased solution resistance and provided more uniform concentration and potential distributions. The performance advantage became more significant at high current densities, where transport losses were more severe. These results show that electrode arrangement and geometry can strongly

affect overall electrolyzer performance even when the electrode materials are similar.

In Chapter 4, urea oxidation was used to replace the oxygen evolution reaction as the anodic reaction. A Ni^{3+}-enriched nickel sulfide catalyst was developed to improve urea oxidation activity and stability. Because urea oxidation has a lower theoretical potential than oxygen evolution, coupling it with hydrogen evolution can reduce the required cell voltage. This approach may also provide a way to combine hydrogen production with the treatment of urea-containing wastewater.

Despite these advances, several challenges remain. First, gas bubble management should be further investigated under practical electrolyzer operating conditions.[1-3] In Chapter 2, nanocone-modified surfaces were shown to promote rapid bubble detachment at high current densities. However, in practical electrolyzers, bubble behavior is affected by electrolyte flow, pressure, temperature, electrode spacing, and long-term changes in surface chemistry, morphology, and wettability.[4-6] Future studies combining high-speed imaging, in situ visualization, and multiphase-flow simulation could establish more quantitative design principles for electrodes that maintain efficient gas removal at high current densities during extended operation.

Second, ionic transport in architected electrodes requires further optimization.[7-9] The interpenetrating gyroid electrode developed in Chapter 3 shortens ion-transport pathways and lowers transport resistance compared with separated electrodes. Future work could systematically tune pore size, strut thickness, electrode spacing, porosity, and tortuosity to balance active surface area, mass transport, mechanical robustness, and electrochemical stability. Hierarchical

or gradient electrode architectures may further improve electrolyte distribution and suppress local concentration gradients under high-current-density operation.[10-12]

Third, catalyst integration with three-dimensional electrodes remains important for translating intrinsic catalyst activity into device-level performance. Catalyst loading, coating thickness, electrical contact, adhesion, and pore blockage can all affect overall electrochemical performance.[13, 14] Therefore, future studies should develop conformal, stable, and scalable catalyst-deposition methods that uniformly modify complex electrode architectures without blocking open transport pathways. Another promising direction is to replace the OER with alternative anodic oxidation reactions.[15, 16] As shown in Chapter 4, urea oxidation has a much lower theoretical potential than the OER and can reduce the energy input required for hydrogen production when coupled with the HER. At the same time, it may enable the simultaneous production of hydrogen and treatment of urea-containing wastewater. However, the UOR still suffers from complex reaction pathways and sluggish kinetics. Future work should use in situ and operando characterization to identify active sites, reaction intermediates, and rate-determining steps. More attention should also be given to nitrogen-containing products and their environmental impacts. Beyond urea oxidation, other low-energy anodic reactions, such as alcohol oxidation, glycerol oxidation, and the oxidation of biomass-derived molecules, may also be coupled with hydrogen evolution.[17-19] These reactions could reduce the required cell voltage while generating value-added anodic products. However, achieving high selectivity, long-term stability, and compatibility with practical electrolyzers remains challenging.

Finally, long-term durability and scale-up remain critical for practical applications. Electrodes designed for high-rate operation must maintain their structure, activity, and interfacial properties over extended periods. Possible degradation mechanisms include catalyst reconstruction, surface oxidation, coating detachment, pore blockage, wettability loss, and mechanical damage caused by continuous gas evolution. Longer stability tests, accelerated stress testing, post-mortem characterization, and device-level studies in flow cells or membrane-separated electrolyzers will be necessary to evaluate their practical relevance.[20, 21]

Overall, this dissertation highlights the importance of integrated electrode and system design for high-rate electrochemical hydrogen production. Surface nanostructuring can improve gas bubble release, interpenetrating three-dimensional architectures can enhance ionic transport, and alternative anodic reactions can reduce energy input. Future advances will likely rely on combining these approaches with stable catalysts, scalable fabrication methods, and practical device configurations. Through continued development, these integrated electrochemical systems may provide more efficient, durable, and scalable approaches to sustainable hydrogen production.

References

1. Zhang, J.; Zhang, Q.; Feng, X., *Adv. Mater.* **2019**, 31, 1808167.
2. Park, J.; Kim, M. J.; Kim, Y.; Lee, S.; Park, S.; Yang, W., *ACS Energy Lett.* **2024**, 10, 212-237.
3. Li, M.; Xie, P.; Yu, L.; Luo, L.; Sun, X., *ACS Nano* **2023**, 17, 23299-23316.

4. Yang, S.; Yuan, J.; Xie, P.; Li, B.; Li, M.; Zhou, D.; Luo, L.; Sun, X., *Nat. Commun.* **2025**, 16, 5732.
5. Iwata, R.; Zhang, L.; Wilke, K. L.; Gong, S.; He, M.; Gallant, B. M.; Wang, E. N., *Joule* **2021**, 5, 887-900..
6. Chen, Y.; Chen, J.; Bai, K.; Xiao, Z.; Fan, S., *J. Power Sources* **2023**, 561, 232733.
7. Oener, S. Z.; Ardo, S.; Boettcher, S. W., *ACS Energy Lett.* **2017**, 2, 2625-2634.
8. Lindquist, G. A.; Xu, Q.; Oener, S. Z.; Boettcher, S. W., *Joule* **2020**, 4, 2549-2561.
9. Yan, X.; Biemolt, J.; Zhao, K.; Zhao, Y.; Cao, X.; Yang, Y.; Wu, X.; Rothenberg, G.; Yan, N., *Nat. Commun.* **2021**, 12, 4143.
10. Zhang, Q.; Hao, Y.; Chen, H.; Li, J.; Zeng, Y.; Xiong, J.; Cheng, Y.; Ozden, A.; Tricoli, A.; Li, F., *Adv. Energy Mater.* **2026**, 16, e04039.
11. Pan, S.; Ye, Y.; Zhang, C.; Chen, X.; Wang, X.; Liu, C.; Li, H.; Tian, B.; Wang, F.; Kou, Z., *Adv. Sci.* **2025**, 12, e10546.
12. Zhang, Q.; Guo, Q.; Zhang, Y.; He, Y.; Gong, W.; Liu, W.; Liu, X.; Li, R., *Adv. Funct. Mater.* **2025**, 35, 2414446.
13. Zhou, B.; Gao, R.; Zou, J.-J.; Yang, H., *Small* **2022**, 18, 2202336.
14. Wang, S.; Lu, A.; Zhong, C.-J., *Nano Converg*. **2021**, 8, 4.
15. Huang, C.-J.; Xu, H.-M.; Shuai, T.-Y.; Zhan, Q.-N.; Zhang, Z.-J.; Li, G.-R., *Small* **2023**, 19, 2301130.
16. Xu, S.; Ruan, X.; Ganesan, M.; Wu, J.; Ravi, S. K.; Cui, X., *Adv. Funct. Mater.* **2024**, 34 (18), 2313309.

17. Li, J.; Ma, Y.; Mu, X.; Wang, X.; Li, Y.; Ma, H.; Guo, Z., *Adv. Sci.* **2025**, 12, 2411964.

18. Wang, T.; Cao, X.; Jiao, L., *Angew. Chem.* **2022**, 134, e202213328.

19. Li, J.; Ma, Y.; Mu, X.; Wang, X.; Li, Y.; Ma, H.; Guo, Z., *Adv. Sci.* **2025**, 12, 241196.

20. Meharban, F.; Lin, C.; Wu, X.; Tan, L.; Wang, H.; Hu, W.; Zhou, D.; Li, X.; Luo, W., *Adv. Energy Mater.* **2024**, 14, 2402886.

21. Kong, S.; Li, A.; Long, J.; Adachi, K.; Hashizume, D.; Jiang, Q.; Fushimi, K.; Ooka, H.; Xiao, J.; Nakamura, R., *Nat. Catal.* **2024**, 7, 252-261.